

MATER. TEHNOL.	LETNIK VOLUME	43	ŠTEV. NO.	1	STR. P.	1–59	LJUBLJANA SLOVENIJA	JAN.–FEB. 2009
-------------------	------------------	----	--------------	---	------------	------	------------------------	-------------------

VSEBINA – CONTENTS

IZVIRNI ZNANSTVENI ČLANKI – ORIGINAL SCIENTIFIC ARTICLES

Nanofolds for soldering and brazing in dental joining practice and jewellery manufacturing

Nanofolije za lotanje pri zobozdravniškem delu in izdelavi nakita

K. T. Raić, R. Rudolf, B. Kosec, I. Anžel, V. Lazić, A. Todorović 3

The pseudo-gradient algorithm for residual gas analysis

Psevdogradientna metoda za analizo masnih spektrov

I. Belič 11

Schemes of metal-working processes and the related tribological equations of fluid mechanics

Scheme procesov predelave kovin in tribološke enačbe mehanike fluidov zanje

D. Čurčija, I. Mamuzić 23

The brittle tensile fracture and cleavage strength of a structural steel with a simulated weld-affected-zone microstructure

Trdnost pri krhkem prelomu in cepilna trdnost za konstrukcijsko jeklo s simulirano mikrostrukturo toplotne cone zvara

G. Kosec, B. Arzenšek, J. Vojvodič Tuma, F. Vodopivec 31

The electrochemical study of duplex stainless steel in chloride solutions

Elektrokemijske raziskave dupleksnega nerjavnega jekla v kloridnih raztopinah

A. Kocijan, Č. Donik, M. Jenko 39

A numerical simulation of metal injection moulding

Numerične simulacije brizganja kovinskih prašnatih materialov

B. Berginc, M. Brezočnik, Z. Kampuš, B. Šuštaršič 43

Investigation of the behaviour in chloride solution of aluminium alloys as materials for protector protections

Raziskava vedenja aluminijeve zlitine, materiala za varovalne elektrode, v kloridni raztopini

D. Vuksanović, P. Živković, D. Radonjić, B. Jordović 49

STROKOVNI ČLANKI – PROFESSIONAL ARTICLES

Improving the process capability of a turning operation by the application of statistical techniques

Izboljšanje procesa sposobnosti struženja z uporabo statistične tehnike

A. Sagbas 55

NANOFOILS FOR SOLDERING AND BRAZING IN DENTAL JOINING PRACTICE AND JEWELLERY MANUFACTURING

NANOFOLIJE ZA LOTANJE PRI ZOBOZDRAVNIŠKEM DELU IN IZDELAVI NAKITA

**Karlo T. Raić¹, Rebeka Rudolf², Borut Kosec³, Ivan Anžel², Vojkan Lazić⁴,
Aleksandar Todorović⁴**

¹University of Belgrade, Faculty of Technology and Metallurgy, POB 3503, 11120 Belgrade, Serbia

²University of Maribor, Faculty for Mechanical Engineering, Smetanova 17, 2000 Maribor, Slovenia

³ University of Ljubljana, Faculty of Natural Sciences and Engineering, Aškerčeva 12, 1000 Ljubljana, Slovenia

⁴University of Belgrade, School of Dentistry, Clinic for Prosthodontics, 11120 Belgrade, Serbia
karlo@tmf.bg.ac.rs

Prejem rokopisa – received: 2008-09-18; sprejem za objavo – accepted for publication: 2008-11-26

This paper describes the development of novel, reactive Al-Au nano-multilayered foils, their possible application in different fields and a discussion of the nano-foils' suitability for dental and jewellery applications. Moreover, this study includes the rapid joining of similar and dissimilar materials, by placing multilayer nano-foils and two layers of solder or braze. The foils precisely control the instantaneous release of heat energy for the joining and act as a controllable local heat source. The reactive foils' thickness is in the range 10 nm to less than 100 nm and they contain many nanoscale layers that alternate between materials with high mixing heats, such as Al and Au. The foil between the two solder/braze layers melts the solder/braze with the heat generated by the reaction and bonds the components. The use of reactive foils eliminates the need for a furnace and dramatically increases the soldering/brazing heating rate of the components being bonded. Thus, ceramics and metals can be fused over required areas without the thermal stresses that are encountered in furnace soldering or brazing. In addition, a completely new plasma technology is proposed for the manufacturing of nano-foils and the first results of the preliminary experimental testing are presented.

Key words: ceramic-metal bonding, low-temperature, nano-foils, plasma technology, dentistry, jewellery

Članek opisuje razvoj nanoplastnih reaktivnih Al-Au-folij, njihovo uporabo na različnih področjih in razprava o uporabi v zobni tehniki in pri izdelavi nakita. Študija vključuje hitro spajanje podobnih in različnih materialov s postavitvijo večplastnih nanofolij ter plasti lota med oba dela za spajanje. Folije kontrolirajo hipno sprostitve toplotne energije za spajanje in delujejo kot lokalni vir toplote. Reaktivne folije z debelino od 10 nm do 100 nm so izmenoma iz materialov, ki imajo veliko toploto mešanja, npr. Al in Au. Folija z reakcijsko toploto raztali obe plasti lota in spoji obe lotani komponenti. Pri uporabi reaktivnih folij je peč nepotrebna, zato se zelo poveča hitrost spajanja lotanih komponent. Keramiko in kovine je mogoče spajati na določenih površinah brez toplotnih napetosti, ki nastanejo pri lotanju s segrevanjem v peči. Sugerirana je tudi nova plazemska tehnologija za izdelavo nanofolij in predstavljeni so prvi rezultati praktičnih preizkusov.

Ključne besede: spajanje keramika kovina, nizka temperatura, nanofolije, plazemska tehnologija, zobotehnika, nakit

1 INTRODUCTION

Multilayer structures are thin-film materials that are periodic in one dimension with regard to composition or composition and structure. Composition/structure variations are generated during the structure's synthesis, which is typically accomplished using atom-by-atom, atom-by-molecule, or molecule-by-molecule technologies. Multilayer structures can be synthesized using elemental, alloy, or compound layers to form both microstructures and combinations of elements/materials that cannot be produced using a traditional processing technology. Multilayers are made by the alternate deposition of two or more different materials. After the first few layers, the structure of all the layers of one material is the same. The structure of each material is clearly of importance for the properties of the multilayer, not only in itself, but also for the influence it can have on the structure of the other material. Each material acts as

a substrate for the deposition of the following. The simplest multilayer structures are those that consist of a composition modulation imposed on a single structure. In almost all cases of this type, intermixing can lead to a uniform single phase of the starting crystal structure or atomic geometry¹⁻³.

Nanoscale multilayer foils are usually produced with physical vapour deposition or magnetron sputtering of hundreds to thousands of alternating layers, with layer thicknesses of approximately 1–102 nm⁴. The process of bonding with reactive multilayer foils is very rapid and easily performed in air (there is no need to join the bonds in a clean room or a specially designed furnace). However, it requires a certain preparation of the components. Most typically, layers of solder or braze are pre-applied to the bonding surfaces of the components. It is also possible to use free-standing sheets of solder placed between the reactive foil and the components, provided the surfaces of the components are easily wetted when

using the solder or braze. This implies that most ceramics' surfaces need to be metallised. Following this preparation, the reactive foil is placed between two components that are aligned and a load is applied. In order to ensure good contact between all the surfaces during fusing, the required value will vary depending on the roughness and flatness of the bonding surfaces. The reaction is then initiated by an electrical or optical pulse, heat is released, the solder or braze reflows, and a bond is formed in approximately one second. For large-area bonds it is common to use multiple, simultaneous initiations of the foil to ensure uniform melting of the solder or braze layers across the bonded area. A number of large-area bonds have been created using reactive foils as the local heat source. Localized heating of the reactive foils enables the formation of large-area ceramic-metal bonds by minimizing the residual stresses between those components having appreciable differences in CTE. The transfer of heat from the reactive foil into the adjacent components during a bonding operation has been numerically modelled and the results experimentally validated using infrared measurements. The numerical modelling is performed using a numerical scheme that is based on finite-difference discretization ².

The shear strengths of various ceramic-metal configurations joined with reactive multilayer foils and different solders or brazes are available in the literature ⁵⁻⁷. It is important to know that the measured strengths depend primarily on the strength of the solder used and not on the combination of materials being bonded. Finally, the significant localized heating that occurs during the bonding process enables these types of bonds.

There are an unlimited number of ways that a nano-foil may be applied. Currently, the biggest markets are energetic (propellant ignition) and large-area joining (armour mounting, structural joining, and the joining of sputtering targets), and small-area joining applications such as sealing and component mounting. A nano-foil could be used to join a broad range of components consisting of metals, ceramics, semiconductors, and polymers. Bonding can be performed in many environments and can be completed in a second or less. Because the heat is localized, components can generally be bonded without thermal damage. Nano-foils can be manufactured by the vapour deposition of hundreds of nanoscale layers that alternate between elements, such as aluminium and titanium. By thermally pulsing one end of the resulting foil with energy, the nanoscale layers begin to mix and release heat to the surrounding foil. This leads to more chemical mixing in the joining areas of the foil and a chemical reaction that self-propagates across the full length of the foil ^{1,2}.

The reactive nano-foils can be used for producing new types of protective coatings, for joining materials and for creating free-standing membranes on the base of intermetallic or ceramic compounds. Taking into account that there are at least several hundred systems for which

self-propagating reactions have been realized in powder mixtures, the few reactive multilayer systems studied so far represent a small part of a wider variety of reactive multilayer films that might be considered as potential subjects for scientific and technological study.

Several combinations of reactive elements and alloys have been tested up to now, including Al/Monel ⁴, Nb/Si ⁸, Ti/Al ⁹, CuO/Al ¹⁰. They all exhibited high propagation velocities of the exothermic reaction waves, up to 15–20 m/s, which indicated the high chemical reactivity of the nano-foils.

In this paper, a completely new plasma technology studied experimentally for the first time, is suggested for the manufacturing of Al–Au nano-multilayered foils.

2 POSSIBILITIES AND APPLICATIONS OF Al–Au NANO-MULTILAYERED FOILS

Al–Au nano-multilayered foils could find two completely new applications in the areas of dentistry and jewellery.

(I) The first application would be in dentistry, because of the following problems that occur in dental joining practice:

(a) *Porcelain Fused to Metal Restorations (PFM) – the bond between an alloy (Co–Cr–Mo, Au–Pt) and porcelain veneer*

Although dental alloys have different micro-alloying elements (Ir, In, Rh, Nb, etc.), which are necessary for the ability to bond ceramics to the metal's surface, there are still problems within metal-ceramics bonding. A potential for failure exists through the thick and brittle oxide layer with many alloy systems, because the extent of the oxide formation cannot be readily controlled. A nano-foil placed between the metal and ceramic layers could strengthen the metal-ceramic bond and enable high quality and longer life for the PFM restorations.

This not only represents an overall benefit to the quality of the dental patients' health, but also long-term savings in health-care-related costs.

(b) *Complex Fixed-Removable Restorations – Joining the abutment (an alloy Co–Cr–Mo, Au–Pt) to the precision attachment (female part) and joining a precision attachment (male part) to the denture base acrylic resin (polymethylmetacrylate)*

Retainers (usually precision attachments) for Removable Partial Dentures (RPD) are used for complex fixed-removable restorations. Prefabricated attachments have two components – one incorporated in the abutment and the other part of the RPD. Both extracoronal and intracoronal attachments are available. Resin bonding has been used for the retention of the extracoronal attachments. There is some doubt that the retention obtained is adequate for preventing the dislodgement of the attachments.

Intracoronary attachments typically consist of a precision-milled male-female assembly and they are made of Pt-Pd alloys that can withstand those high temperatures associated with the casting of PFM alloys. The female part of the attachment is incorporated in a wax pattern. After the wax elimination, the restoration is cast directly onto the attachment. The male part of the attachment is either soldered to the frame or attached to the acrylic denture base with auto-polymerizing resin. Most dental technicians prefer to solder the parts of the attachment. However, there are failures of attachment systems, especially when they are used with distal extensions. In order to strengthen the bond between the female attachment and the abutment, and the male attachment and the denture base, a nano-foil could be placed in-between.

(c) Dental Implants – the bond between an alloy (cpTi, Ti-6Al-4V, Ni-Ti) and Hydroxyapatite, Zirconium-oxide coatings

Dental implants made of cpTi or different Ti-alloys (Ti-6Al-4V) have been used in dentistry for many years. The clinical use of various coatings (plasma-sprayed hydroxyapatite-HA coatings, diamond coatings, diamond-like-carbon coatings, yttria-stabilised zirconia, ZrO_2 -3 % Y_2O_3 coatings) on Ti-implants has been widely adopted because the coatings can achieve firm and direct biological fixation with the surrounding bone tissue. They have great potential for use as biomedical implants because of their very high hardness, excellent wear resistance, low friction and biocompatibility characteristics. However, the poor bonding strength between the various coatings and the Ti alloy has been of great concern for long-term clinical applications.

HA/yttria-stabilized zirconia (YSZ)/Ti-6Al-4V composite coatings that possess superior mechanical properties to conventional plasma-sprayed HA coatings have been developed. The bonding strength is better than that between a plasma-sprayed HA coating and Ti-6Al-4V, but this bond strength could further be improved by placing a nano-foil between an implant and a coating.

A nano-foil placed between an implant (Ti-6Al-4V) and an HA and/or ZrO_2 coating could strengthen the bond between the HA/ ZrO_2 coating and the Ti alloy, and could enable high quality and a longer life for the dental implant.

The other possibility is to find a suitable nanostructured metallic-ceramic coating that could provide a nanocrystalline metallic bond at the interface to the hard ceramic bond on the surface.

(II) The second application in jewellery:

(a) Metal-Stone Joining. The joining of many different materials is necessary in jewellery manufacture (the metal frames of rings, earrings, necklaces, etc. with different kinds of stone – precious, semi-precious, synthetic stones, coral, and pearls).

One of the phases in jewellery manufacturing is placing the precious stone into the metal frame. The stones are initially cut into the desired sizes and shapes, and then polished. The metal frame cast is ground and polished and the stones are joined to it by adhesives, soldering, or by mechanical clamping. The attachment between the stone and the metal becomes weaker over time, because of elastic deformation. If the stone is soldered to the metal frame, the joint between the stone and the metal is stronger. Different stones have different mechanical and physical properties and it is necessary to find an appropriate combination of solder components for each stone. For example, sapphire is an Al_2O_3 mineral. Sapphire can be soldered after bonding or brazed without bonding. If the sapphire is brazed to titanium without bonding, an alloy with 72 % Ag could be used. Diamond could be brazed to steel with L-Ag40Cd, L-Ag30Cr and L-Ag20Si.

There are two groups of precious stones according to their price: first-order stones (diamond, ruby, sapphire and emerald) and second-order stones (aquamarine, topaz, zircon, onyx, quartz topaz, etc.). Many of them have similar chemical compositions, but their colours are different. The chemical composition of diamond is 99.95 % carbon. Emerald is a green mineral made of aluminium oxide, and its colour comes from chrome or vanadium. Sapphire and ruby are minerals of Al_2O_3 . Sapphire could have a blue colour from titanium and iron, and violet from vanadium. Ruby could have a red colour from chrome or a chestnut colour from chrome and iron. The chemical compositions of the stones could be very important when joining different kinds of stones. Many stones in the second group are very sensitive to heat. The result of heating the stone above its critical temperature could be a change in the colour. Turquoise has a critical temperature at 250 °C, when its colour then changes from sky blue to green. At the critical temperature interval of tanzanite (from 400 °C to 500 °C), the nuances of yellow gradually disappear and the blue colour is intensified. Other precious stones can also exhibit changes in their colours (quartz, topaz, amethyst, aquamarine, etc.). Therefore, it is very important that during the joining of stones to the metal frame the stones are not heated above their critical temperatures. This can be achieved by local heating of the nano-foil that is placed between the stone and the metal frame. Also, a nano-foil placed in between could strengthen their joint and enable a high-quality jewellery piece.

(b) Metal-Metal Joining. Many different pieces of jewellery have several parts included in their construction. These components are usually joined by gold brazing alloys. The rule, that the brazing alloy must have the same purity (in carats) as the pieces that are joined, has to be respected. The colour of the solder must also be the same. It is necessary for the brazing temperature to be higher than the liquidus temperature of the

brazing alloy, but lower than the solidus temperatures of the materials that have to be joined.

The composition of the brazing alloys used for jewellery applications is Au-Ag-Cu, with the addition of metals such as zinc and cadmium. Cadmium is very toxic, especially its vapour, during the melting process, and must be replaced with non-toxic elements. Cadmium could be substituted by the following metals: tin (Sn), indium (In), gallium (Ga), and zinc (Zn). Also, some solders without cadmium have very high concentrations of Ni (5 to 9 %). According to the EU directive 76/769 EES (January 2000), the concentration of nickel in jewellery cannot exceed a maximum of 0.05 %. This EU directive is a prerequisite for the prevention of allergic reactions caused by nickel. A nano-foil, with properly selected solder or braze components (without Ni) placed between metal parts, could prevent allergic reactions to nickel and could ensure the high quality of metal-metal joins.

3 EXPERIMENTAL PROCEDURE

The Al-Au multilayered foil was obtained by plasma-assisted sputtering in a Plasmait[®] machine¹¹. Atoms of a Au-alloy and Al were sputtered from two separated targets/wires (with diameter $\phi = 3.5$ mm), pure aluminium ($w = 99.99$ %), and 14-carat gold alloy with the chemical composition (mass fractions w : 58.50 % Au, 28.95 % Ag, 12.45 % Cu), **Figure 1**.

The Plasmait[®] machine, with its dynamic sealing system, allows for the continuous processing of materials. The wire or tape guided through the machine is processed with a Special Type Glow discharge working within the pressure range 1–10 mbar. Most applications are processed with N₂, but Argon was added to the discharge as was the case with the multilayer deposition of an Au-alloy and Al for a better sputtering effect.

The wire speed through the processing chamber while processing the thin films was 30 m/min, which equals 0.5 m/s, and the processing power coupled into the plasma was approximately 250 W for the Au-alloy wire and 800 W for the Al wire. All these parameters

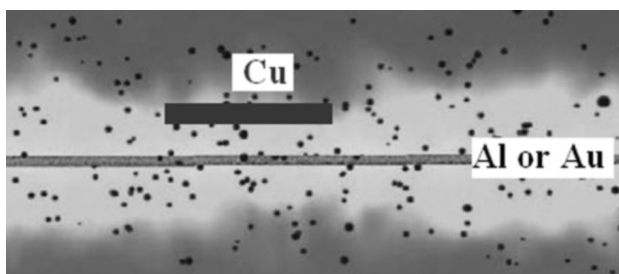


Figure 1: Demonstration of the plasma effect – ion bombardment from the wire (Al or Au) towards the Cu substrate

Slika 1: Prikaz efekta plazemskega ionskega bombardiranja žice (Al ali Au) in nanos na Cu podlagu

(pressure, power in plasma, gas composition, wire speed and wire type) were optimized during the processing.

A substrate of pure copper with dimensions 10 mm × 10mm (thickness about 0.5 mm) was placed on a holder, to be exposed to fluxes of atoms from a Au-alloy or Al atoms, consecutively. The required number of alternating layers was obtained by adjusting the number of turns and thickness for a varying wire speed and magnetron source power.

The Cu/Al-Au-Al-Au/ sample was prepared with Al and Au layers with thicknesses of about 100 nm to 400 nm. The substrate temperature was kept below 323 K in order to prevent any diffusion and reaction during the deposition.

The microstructural characterisation of the produced nano-foils was carried out with scanning electron microscopy (SEM-Sirion 400 NC) and energy-dispersive X-ray (EDX) analyses (Oxford INCA 350). For the electron microscopy the polished specimens were put in the chamber of the SEM microscope, with a vacuum of 10⁻⁶ mbar. The microscopic analysis includes an examination of the polished surface and qualitative and quantitative micro-chemical analyses at characteristic points on the interface between the Au-Al nanofoils and the substrate Cu. We observed surfaces using an electron-beam voltage at 30 kV, and over different working distances (6.5 mm, 7.2 mm, etc.).

Finally, the nano-foils were characterised using a Quanta 200 3D environmental scanning electron microscope equipped with a focussed ion beam (FIB), which enables the cleaning and etching of a sample's surface, transverse cutting directly from the external sample surface, polishing of the cutting surface, and high-resolution observations of the samples' microstructures.

4 RESULTS

The microstructure of the Al-Au multilayered foils is shown in **Figure 2**. From the upper view (**Figure 2a**), a very porous surface could be seen for the last Au nano-foil. This assumption was additionally confirmed by further investigation, namely on the transverse cutting surface (**Figures 2b, 2c**), where regions could be found with small and large voids over the cross-sections of all four foils. Voids within the single foils are surrounded with the agglomerate. It seems that the atoms from the Au-alloy accumulated non-homogeneously on the surface of the Cu-substrate, and caused the formation of a very porous microstructure. Detailed microstructure observations demonstrate that the foils mainly possess a columnar microstructure. This kind of microstructure is typical for foils deposited on a cold substrate. Precise measurements of each foil discovered that the Al-foils have an approximate thickness of about 100 nm, while for the Au-foils the thickness was about 400 nm. Consequently, we could conclude that at similar technical

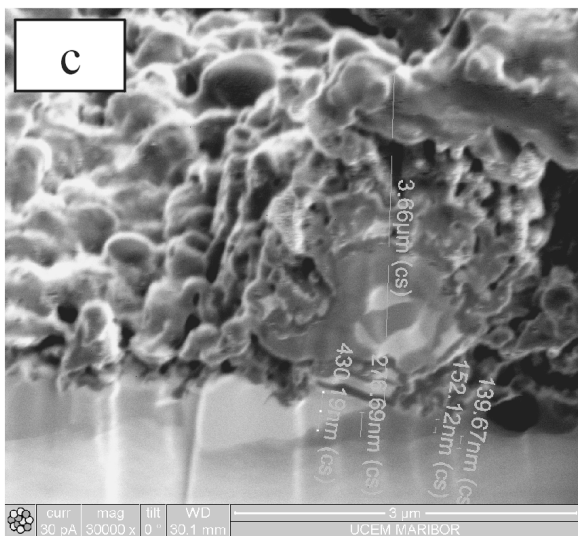
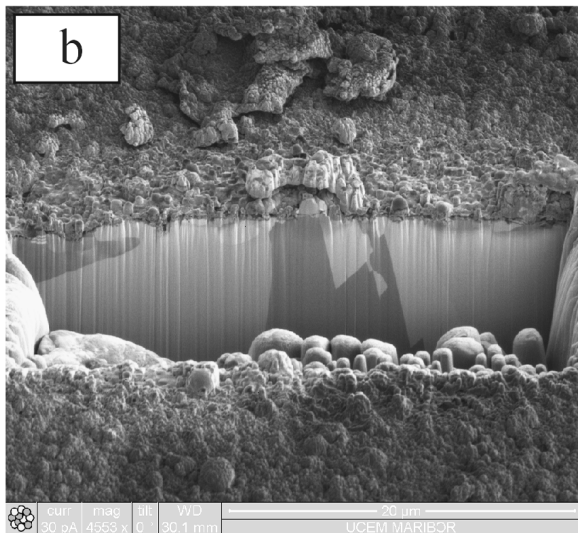
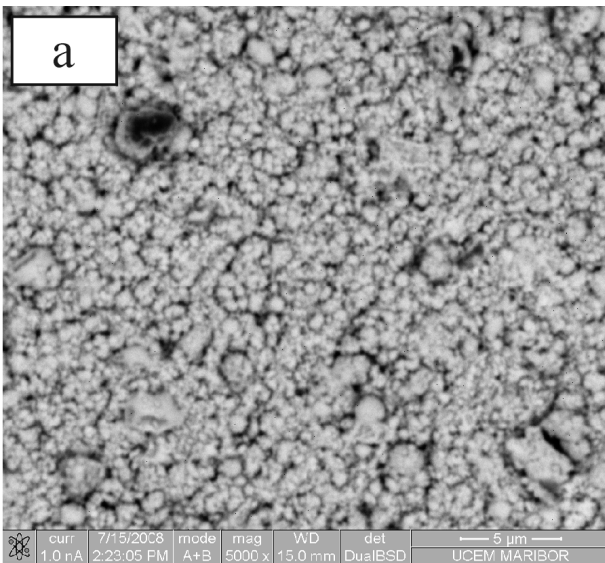


Figure 2: SEM micrographs of : (a) surface, (b) space view and (c) cross-section of Cu /Al-Au-Al-Au/ specimen

Slika 2: SEM-posnetek: (a)–površina, (b) pogled na površino, (c) prerez vzorca Cu/Al-Au-Al-Au

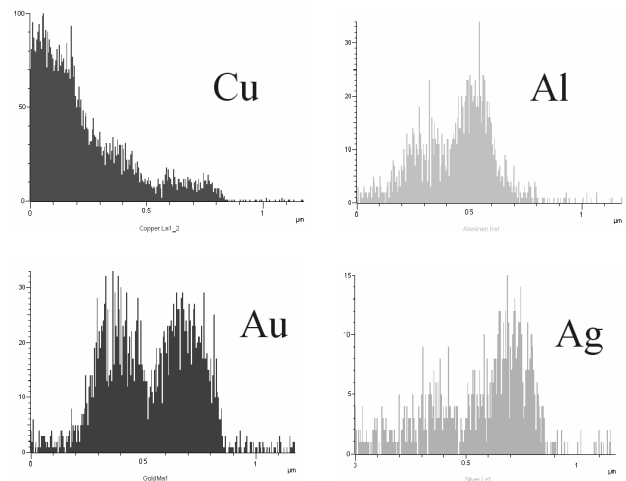
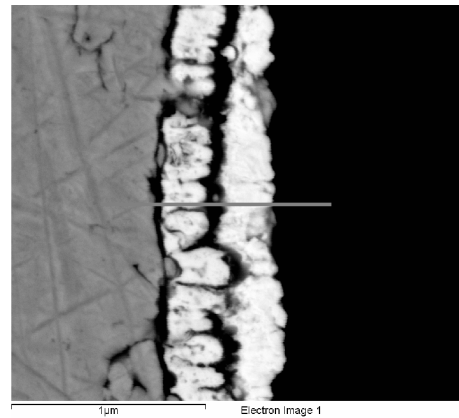


Figure 3: SEM micrograph with EDX line-analyses of Cu /Al-Au-Al-Au/ specimen cross-section, the light layers are Au and the dark layers are Al

Slika 3: SEM-posnetek z linijsko analizo EDX prereza vzorcev Cu/Al-Au-Al-Au. Svetle plasti so Au, temne pa Al

parameters of the plasma process, the thickness of the Au-foil is twice as large as for the Al-foil.

EDX line-analyses (**Figure 3**) over the cross-sections of Al-Au-Al-Au foils also indicate the presence of Ag and Cu atoms in the Au-foils. These elements rise from the alloy, which was used as a wire-positive electrode in the plasma device. The distribution of the elements in Au-foils followed the chemical composition of the wire, which means the higher mass fraction (%) of the element causes a higher peak in the EDX spectrum. On the other hand, only the presence of Al was established for the Al-nano-foil.

The transformations of the pure metals to Al–Au intermetallics at the Al/Au alloy interfaces were not found and interdiffusion between the Cu substrate and the first Al layer was not detected.

5 DISCUSSION

This paper presents nano-foils that were produced using the plasma process. The plasma is an ionised

(exited) gas, where we are used to imagining gas as free atoms and molecules chaotically flying through space ¹².

In a plasma device, the electric field accelerates the ions towards the wire surface (the positive electrode) and electrons towards the edge of the heating chamber (the negative electrode). On their way to the opposite electrode, the particles collide with other atoms and molecules. The less they collide (or the less interrupted their journey), the faster they accelerate and the larger their impact on the wire surface. The plasma device's heating chamber is filled with a low-pressure inert gas to prevent a chemical reaction between the gas and the wire. The wire is fed through the sealing system and the heating chamber continuously, thereby exposing the wire surface to ion bombardment. The effect of such bombardment is threefold: (1) efficient heating, (2) surface smoothing and (3) effective surface cleaning.

(1) Colliding ions release their energy on the surface and heat the wire. In the heating chamber the ions are directed to the wire surface, while the electrons head towards the outer wall of the heating chamber. As the ions are approximately 50,000 times heavier than the electrons, they make a considerably higher energy impact on the wire than that caused by the electrons on the chamber wall. In fact, the energy conducted to the chamber is negligible compared to the energy conducted to the wire. Effectively, all of the power conducted into the plasma is transferred to the wire (and not the walls of the heating chamber). The unique benefit of the plasma treatment is the concentrated impact on the wire surface (directional and focused heating) resulting in a very efficient heating process. As with the microwave oven, the heating chamber remains cool during the process. Less heat transmission to the surroundings also means a friendlier working environment. The fact that the heating process concentrates on the wire alone makes a plasma treatment very effective for high-temperature applications, such as heat treatment. Moreover, the plasma-assisted heating process can be easily and instantly regulated through the electric potential in the heating chamber. The intensity of the wire treatment can be regulated to a desired value within milliseconds by adjusting the voltage in the heating chamber. In practice, this leads to another benefit of plasma technology.

(2) Plasma treatment results in a smoothing effect on the wire surface. Like lightning striking a tree in a field, ions are directed to the tips of the irregularities. The density of ion bombardment is highest on the sharp edges and nibs on the wire surface, concentrating on the tips of the irregularities until they melt away. This leads to a smoothing effect, causing a reduction in the macro-roughness and an increased micro-roughness of the wire surface. In some cases a wire with a damaged or rough surface can be improved in quality, and can even reach the standards of a magnetic wire surface.

(3) The plasma treatment is also an effective cleaning process. The ions bombarding the wire break down dirty

deposits and oxide layers on the wire surface. One can imagine the cleaning process as sand blasting on an atomic scale. A plasma treatment can, therefore, replace the deoxidising, degreasing or other wire-cleaning processes, whilst eliminating the chemicals from the wire-production process. The dirt blasted away burns into ashes and falls off from the surface. The ashes collect at the bottom of the heating chamber and in the vacuum pump's filters. The materials where plasma technology is less competitive are those that require long annealing times, in other words those that need to be exposed to high temperatures for a long time. For such an application, high-speed in-line annealing is likely to be unsuitable, due to the required length of an inline cooling system, necessary for such an application.

For the production of nano-foils in the first step we used the cleaning and smoothing process in order to ensure a high-quality surface for the Cu substrate (reduction in macro-roughness). With this step we wanted to obtain a surface with a low degree of surface defects, which consequently could lead to the formation of a very homogeneous formatted nano-foil. Based on microstructural observations, we could conclude that this step was very successful because the Cu-substrate surface in the cross-section is pretty flat (on the micro-level). In the second step we used the plasma-deposition process for producing nano-foils. On the basis of the obtained nano-foils we could see that the process, in the case of Al-deposition, is completely different to that of Au-deposition. The Al-foils are thin (about 100 nm in thickness), compact and almost without big voids. The Au-foils are thick (about 400 nm), with a quite different non-homogenous microstructure, including many defects (pores and non-uniform grains within the foil). We believe that the reason for the non-homogeneous microstructure is the presence of alloying elements (Ag and Cu), which influence atom segregation during the plasma process.

Al and Au are face-centered cubic (FCC) metals with the highest packing density. In order to understand the change in thickness (volume) during the formation of Al and Au layers, we can compare the density and atomic packing factor (APF) of the pure metals, Table 1. The amounts of volume that the atoms occupy calculated by the APF are equal for Au and Al, but the density of the Au is nine times higher than that of Al. So, for the same processing conditions (wire speed of 0.5 m/s for Al wire and Au-alloy) it is to be expected that the Au-foils will be thicker.

Table 1: The density and APF of Au and Al ¹³

Tabela 1: Gostota in A. P. F. za Au in Al ¹³

	Density, $\sigma/(g/cm^3)$	A. P. F
Au	19.33	0.74
Al	2.7	0.74

Based on the description, the main further research goals would focus on the following areas:

- the determination of the nano-foils' properties, such as the mechanical properties, hardness, chemical inertness (e.g., oxidation, corrosion), biocompatibility, bioresistance, and the wear resistance of metal-ceramic and related joints;
- the optimization of different chemical compositions for obtaining novel nanostructured reactive foils;
- the determination of optimal heat treatment (to estimate the optimal time-temperature diagram) for nanostructured foils. Different heat treatments, training and testing of the materials' functional properties are part of this optimisation;
- the development of suitable methods for fusing a metal with ceramics and/or a metal by inserting nanostructured multilayered foils. The basis would be the already-known methods, but they would have to be modified in order to comply with the specifically requested characteristics for the investigated metal-ceramic/metal and related joints;
- to gain new knowledge about the long-term stability of novel nano-foils;
- to gain a deeper insight into the mutual dependence of the chemical composition, the purity of the nanostructured coatings, the production route and parameters, the microstructure, and the mechanical and functional properties;
- to take a first step towards industrial production;
- to discover new, possible biomedical and other applications for nanostructured films, i.e., wear-resistant orthopaedic implants, etc.

6 CONCLUSIONS

Plasma technology represents a novel approach in the production of nano-foils. Preliminary results of the produced nano-foils with plasma technology show that there are still problems with ensuring the single foil's constant thickness into the sandwich nano-structure. Moreover, the obtained microstructure of the nano-foil depends, mostly, on the initial chemical composition of the surface wire, used as the positive electrode. Also, the other important conclusion is that with nearly the same technological parameters of the plasma technology, the formatted nano-foils of different initial materials are dissimilar. Finally, the shape and the quality of the final nano-foil depends on the preparation of the substrate surface.

ACKNOWLEDGEMENT

This paper is part of the Eureka project E!4213 NANO-FOIL. The authors gratefully acknowledge the Ministry of Higher Education, Science and Technology of the Republic Slovenia and the Ministry of Science and Technological Development of the Republic of Serbia.

7 REFERENCES

- ¹ Nguyen TD, Lairson BM, Clements BM, Shin S-C, Sato K, editors. Structure and properties of multilayered thin films. Materials research society symposium proceedings, vol. 382. Pittsburgh (PA): MRS; 1995. p. 1–493
- ² A. Duckham, J. Levin, and T.P. Weihs, Soldering and Brazing Metals to Ceramics at Room Temperature using a Novel Nanotechnology, *Advances in Science and Technology*, 45 (2006), 1578–1587
- ³ T. P. Weihs, *Handbook of Thin film Process Technology*, ed D.A. Glocker, S.I. Shah, Institute of Physics, Bristol, UK, F7:1-F7:13, 1998
- ⁴ Barbee TW, Weihs T. US Patent No 5538795, July 23; 1996
- ⁵ A. K. Jadoon, B. Ralph, P. R. Hornsby, Metal to ceramic joining via a metallic interlayer bonding technique *Journal of Materials Processing Technology* 152, (2004) 3, 257–265
- ⁶ J. Wang, E. Besnoin, O. M. Knio, T.P. Weihs, Investigating the effect of applied pressure on reactive multilayer foil joining, *Acta Mater.* 52 (2004) 18, 5265–5274
- ⁷ A. J. Swiston Jr., T. C. Hufnagel, T. P. Weihs, Joining bulk metallic glass using reactive multilayer foils, *Scripta Materialia*, 48 (2003) 12, 1575–1580.
- ⁸ M. E. Reiss, C. M. Esber, D. Van Heerden, A. J. Gavens, M. E. Williams, T. P. Weihs, Self-propagating formation reactions in Nb/Si multilayers, *Mater. Sci. Eng. A* 261 (1999) 1–2, 217–222
- ⁹ J.-C. Gachon, A. S. Rogachev, H. E. Grigoryan, E.V. Illarionova, J.-J. Kuntz, D. Yu. Kovalev, A. N. Nosyrev, N. V. Sachkova, P. A. Tsygankov, On the mechanism of heterogeneous reaction and phase formation in Ti/Al multilayer nanofilms, *Acta Mater.* 53 (2005), 1225–1231
- ¹⁰ K. J. Blobaum, M. E. Reiss, J. M. Plitzko Lawrence, T. P. Weihs, Deposition and characterization of a self-propagating CuOx/Al thermite reaction in a multilayer foil geometry, *J. Appl. Phys.* 94 (2003)5, 2915–2922
- ¹¹ www.plasmait.com
- ¹² Peter Ziger, Chief Technology Officer (CTO), Plasmait GmbH, How does plasma work? Publication of Niedermair Group
- ¹³ Zhang X, Yan TT, Thin solid films, proceedings of the international conference on materials for advanced technologies (ICMAT 2005) Symposium H: silicon microelectronics: processing to packaging-ICMAT 2005 Symposium H, 504(1–2):355–361

THE PSEUDO-GRADIENT ALGORITHM FOR RESIDUAL GAS ANALYSIS

PSEVDOGRADIENTNA METODA ZA ANALIZO MASNIH SPEKTROV

Igor Belič

Institute of metals and technology, Lepi pot 11, 1000 Ljubljana, Slovenia
igor.belic@imt.si

Prejem rokopisa – received: 2008-12-19; sprejem za objavo – accepted for publication: 2009-01-12

The article focuses on a special approach to the qualitative and quantitative residual gas analysis of a vacuum-chamber atmosphere. The main outline of mass-spectrometry usage is given together with a brief comparison of two completely different scientific fields. The new approach, where the mass spectra are formalized in a vector annotation, to residual gas analysis is proposed. The main problem with residual gas analysis based on a mass spectrum is its ambiguity, which cannot be easily resolved. One way to deal with the problem is practical knowledge about the interpretation of mass spectra. The pseudo-gradient algorithm for mass-spectra analysis was developed and tested. The general testing platform was developed and the algorithm was tested within it. The presented work is the foundation for a comprehensive study of mass-spectrum analysis techniques. An important concept is the virtual environment that provides the mass-spectrum generator, the standard fragmentation patterns' database, the data space for the various algorithms that can test various approaches to the mass-spectrum analysis, and the database of the achieved results, which is necessary for the comparison of different algorithms and represents the backbone for the dynamic mass-spectra generation and analysis.

Key words: mass spectra, residual gas analysis, gradient descent, optimization

V prispevku je opisan nov način kvalitativne in kvantitativne analize rezidualnih plinov atmosfere v vakuumskem sistemu. Uvodoma je podan pregled različnih vrst uporabe masne spektrometrije, skupaj s pregledom dveh povsem različnih znanstvenih področij. Prikazan je nov način, ki pojmuje masne spektre v formalni vektorski obliki. Osnovni problem pri analizi masnih spektrov, ki ga ni mogoče enostavno rešiti, je njihova večličnost. Ena od možnosti je uvedba praktičnih izkušenj, ki algoritmu pomaga pri razrešitvi nekaterih dvoumij. Razvita in analizirana je psevdo-gradientna metoda za rezidualno analizo plinov iz masnega spektra. Razvito je bilo preizkusno okolje, v katerem je bil analiziran algoritem.

Predstavljeno delo je temelj za široko študijo tehnik za analizo masnih spektrov. Pomemben koncept je virtualno okolje, ki vsebuje generator masnih spektrov, podatkovno bazo standardnih masnih spektrov, podatkovni prostor za hranjenje rezultatov preizkusov algoritmov, ki so nujni za kasnejšo primerjavo delovanja posameznih algoritmov. Virtualno okolje je tudi temelj za kasnejšo dinamično analizo masnih spektrov.

Ključne besede: masna spektrometrija, rezidualna analiza plinov, gradientna metoda, optimizacija

1 INTRODUCTION

The use of mass spectrometry is very widespread and versatile. Many types and various configurations of mass spectrometers are in use. Basically, there are two different ways that mass spectrometry is used: one is for the detection of substances through the fragmentation patterns detected by the mass spectrometers and the other is the use of mass spectrometry in vacuum science. The first is a very wide field that includes chemical, pharmaceutical, biological (from now on bio-chemical) and other purposes, mainly for the study of the structure of substances. The main feature of mass spectrometry that deals with the structures of numerous organic substances (combined with other methods – gas chromatography, etc.) is that one substance (or a small number of them) of a very complex and often unknown structure is introduced to the mass-spectrometer analyzer and the obtained mass spectrum is then analysed.^{1,2} Finding the fragmentation patterns of organic substances is a very complicated process, but necessary in order to implement the automatic mass-spectra identification.³ For this

purpose several software products were developed and are widely used. To illustrate the unbalance in software support that utilizes the mass-spectra analysis in bio-chemical and vacuum fields, several products are listed.

The bio-chemical field is very well supported by numerous commercial software packages. One such software product is the Mascot mass-database search program.⁴ This is a powerful search engine that uses mass spectrometry data to identify proteins from primary-sequence databases.^{5,6} Another one is Analyst software.⁷ A Microsoft Windows-based data system that provides instrument control and data analysis for the entire family of Thermo Scientific mass spectrometers and related instruments is the Xcalibur.^{8,9} Several specialized software modules have been designed to work with Xcalibur to meet the needs of specific applications. MassLynx^{10,11} is a fundamental platform for acquiring, analysing, managing and sharing mass-spectrometry information. The Sample List is a key feature of MassLynx, keeping everything about the samples together in one place. It is also the central place for initiating any activities relating to the sample. It provides

general purpose and specialised application managers dedicated to providing information for specific types of mass-spectrometry analyses and data. Agilent Technologies MassHunter Workstation software¹² is designed to streamline mass-spectrometry analysis, from instrument tuning through to the final report. It enables users to find all the compounds in samples, find differences between samples and find sample sets. The MassHunter workstation uses data-mining techniques to search the mass databases in public and private domains. Geneva Bioinformatics (GeneBio) has launched a software platform known as SmileMS for the identification and analysis of small molecules by mass spectrometry.¹³ SmileMS provides machine-independent software for the analysis of MS spectra from small molecules. It allows each user to add both public and private databases. Mascot Distiller⁵ is used to identify the mass spectra corresponding to proteins from the Information Non-Redundant Protein Sequences Database. The list of commercial software dealing with bio-chemical mass spectrometry is long and versatile¹⁴ (4000 Series Explorer, Analyst QS, BioAnalyst, Cliquid, DiscoveryQuant, GPS Explorer, LightSight, MALDI Imaging, MarkerView, Metabolite ID, MRMPilot, MultiQuant, Pro ICAT, Pro ID, Pro QUANT, ProteinPilot, SimGlycan, TissueView, etc.).

These mass spectra are obtained by various types of instrumentation layouts, such as tandem mass spectrometers MS/MS^{3,15,16,17,18,19}, collision-induced dissociation (CID) MS/MS²⁰ time-of-flight mass spectrometers (TOF)^{16,18,21,22,23,24}, ion-trap mass spectrometers¹⁹, quadrupole/ion-trap mass spectrometers^{15,25}, and the MALDI (Matrix-assisted laser desorption/ionization) technique used for mass spectrometry^{6,23}, etc.

In the bio-chemical field mass spectrometry is widely used in order to identify the peaks resulting from a chromatographic separation.²⁶ The most common approach to solve the problem for unknowns on whom very little other structural information is available is the use of a retrieval algorithm and a reference mass-spectra database.

There are large reference databases of mass spectra at the NIST and Wiley libraries. The NIST/EPA/NIH mass spectral databases²⁷ contain, in the 2008 version, 220,460 spectra of 192,108 unique compounds (for electron-impact mass spectrometry), and 14,802 spectra of 5308 precursor ions for tandem mass spectrometry.

The largest database is the Wiley's Registry of Mass Spectral Data²⁸, in 2008 containing 560,000 different spectra, over 348,000 spectra with chemical structures. It is one of the most comprehensive mass spectral libraries ever published. There are also specially designed mass-spectra search programs to make use of these vast databases.

In vacuum science there are again two major categories of how mass spectrometry is used. The first, which is in terms of operation very close to the bio-chemical

uses, is the vacuum-system leak detection.²⁹ The tracer gas is introduced to the system and again one gas fragmentation pattern is monitored by a mass spectrometer.

Another and yet much more complicated category is residual gas analysis, which is a general term for the analysis of gas and vapour species in vacuum chambers and vacuum processes. The main feature of all the previously mentioned methods is that the main objective of it is the detection and analysis of various species that compose the vacuum-chamber atmosphere simultaneously. It is no more the case where one or a very small number of species is to be detected and compared to the known spectra in a database. Here, the number of "expected" vacuum-chamber atmosphere constituent gases is to be combined in such a way as to provide the partial pressures of each and every one of them.

A search over the internet reveals that the field is far less equipped with software than is the case with bio-chemical mass spectrometry. Among the features found in the literature³⁰, the software (MASsoft³⁰, Merlin Research³¹, Questor 5 Process Analysis software³¹) provides the following interesting features:

- Histogram, Trend Analysis and Analog peak displays.
- Mixed mode scanning, e.g., Trend, Histogram and Analog peaks in multiple-windows
- Simultaneous real-time display of graphical and tabular trend analysis data.
- Peak-height identification.
- Real-time background subtraction.
- Automatic mass-scale alignment.
- Statistical analysis of data in real time
- Partial pressure ratios
- Quantitative or normalised composition analysis
- Visualisations

In this article we focus on a special approach to qualitative and quantitative residual gas analysis.

1.1 Mass spectra as vectors

The fragment patterns of atoms and molecules that may coexist in a vacuum system are composed of a sequence of number pairs, as shown by the CH₄ example in **Table 1**.³²

Looking at this annotation from another perspective, one can see that the sequence of numbers (**Table 1** left) represents only a fraction of all possible m/u components (only from $m/u = 12$ to $m/u = 17$). The complete "picture" of the CH₄ standard fragmentation pattern is presented in **Table 1**, on the right.

The same is true for all the other constituents of a vacuum-chamber atmosphere. The fragmentation pattern can be rewritten in vector form as follows:

$$\mathbf{G}_{\text{CH}_4} = (0, 0, 0, 0, 0, 0, 0, 0, 0, 0, 0, 0, 2.4, 7.7, 15.6, 85.8, 100, 1.2) \quad (1)$$

Table 1: CH₄ fragmentation pattern**Tabela 1:** Fragmentacijski vzorec CH₄

m/u	Normalized amplitude	m/u	Normalized amplitude
12	2.4	1	0
13	7.7	2	0
14	15.6	3	0
15	85.8	4	0
16	100	5	0
17	1.2	6	0
		7	0
		8	0
		9	0
		10	0
		11	0
		12	2.4
		13	7.7
		14	15.6
		15	85.8
		16	100
		17	1.2

This is a classical vector annotation, where the number of all the used m/u components defines the dimensionality of the vector space.

Any peak in a mass spectrum of a mixture of gases may consist of a combination of molecular ions and/or fragment ions. The contributions add linearly and the peak height for the discrete m/u is equal to the sum of the individual peak heights that would be produced if each constituent were alone in the system. This is the classical presumption of superposition.³²

$$S_i = \sum_j s_{ij} \quad (2)$$

The sum in (2) is taken over all gases currently present in the vacuum chamber. The consecutive gas is marked by the index j ; S_i is the total peak height at the mass number i ; s_{ij} is the peak height contribution from gas j at the m/u number i .

s_{ij} is related to the fragmentation pattern, the analyzer sensitivity, and the partial pressure of gas j by the equation:

$$s_{ij} = A_j P_j g_{ij} \quad (3)$$

Where A_j is the analyzer's sensitivity to the gas j ; P_j is the partial pressure of gas j ; the principal peak of the standard fragment pattern is always set to 1. Other peaks at $m/u = i$ represent the ratio to the principal peak and are denoted by g_{ij} .

In a formal vector annotation the mass spectrum is a weighted sum of the constituent fragment patterns, such as:

$$S = \sum_j w_j G_j; \quad w_j = a_j p_j \quad (4)$$

S is the vector of the total peak heights; w_j is the weight, valid for the j -th constituent fragment pattern; and vector G_j , is the j -th gas-standard fragment pattern.

However, the equation exactly models the ideal situation, where all the constituent components of the atmosphere are known a priori. In practice one must always expect the unknown substances to be present in the vacuum system and contribute to the mass spectra. Another problem that additionally complicates the interpretation of mass spectra is the inevitable noise produced by the instrumentation equipment. Both components add to the so-called noise. The equation can be therefore rewritten as:

$$S = \sum_j w_j G_j + N; \quad w_j = a_j p_j; \quad N = S_u + N_e \quad (5)$$

Where N is the vector representing the noise. The overall noise N is composed of two components: S_u – the spectral components of unknown constituents, and N_e – the electrical noise.

1.2 The ambiguity of mass spectra

The equations (4) and (5) formally represent the synthesis of the mass spectra. On the other hand, from the practical point of view, we are interested in a reverse process, i.e., analysis. The basic question of mass spectrometry is which constituents are composing the given mass spectra and in what quantities.

From the mathematical theory, it is very well known that such a task is only achievable under the very strict condition of orthogonality, which must be fulfilled for all the constituent vectors. If this is not the case, the result can still be achieved, but it is never unique.

Table 2: The example of mass-spectra ambiguity

Tabela 2: Primer večličnosti masnega spektra

Standard Fragmentation Patterns	m/u	Constituent A	Constituent B	Constituent C	
	1	1	2	1	
	2	1	1	2	
Case 1	Multiplication factors 1	2	1	3	
	m/u	Constituent A	Constituent B	Constituent C	Point T
	1	2	2	3	7
	2	2	1	6	9
Case 2	Multiplication factors 2	1	1.333	3.333	
	m/u	Constituent A	Constituent B	Constituent C	Point T
	1	1	2.666	3.333	7
	2	1	1.333	6.666	9

Let us suppose we have three constituent gases, and that we observe only two m/u values: $m/u = 1$ and $m/u = 2$.

The experiment to demonstrate the basic ambiguity of the mass spectra is shown in **Table 2**. For this purpose, the standard fragmentation patterns for three virtual gases were set. The next step is to generate the mass spectra that contains the three gases, For this, the multiplication factor for each constituent must be set and the mass spectra is created, according to equation (4), taking into account that all the sensitivity factors a_j are

set to 1. The result of the mass-spectra synthesis is the actual spectra, or "target" point T, which represents the superposition of all three constituent gases, multiplied by their factors.

The next step is the inverse process, meaning that we have the mass spectra – point T, and we seek the multiplication factors that produce that mass spectra. The figures in **Table 2** clearly show that the same mass spectra can be achieved by the factors 2, 1, 3, and 1, 1.333, 3.333 as well. The experiment is graphically illustrated in **Figure 1**.

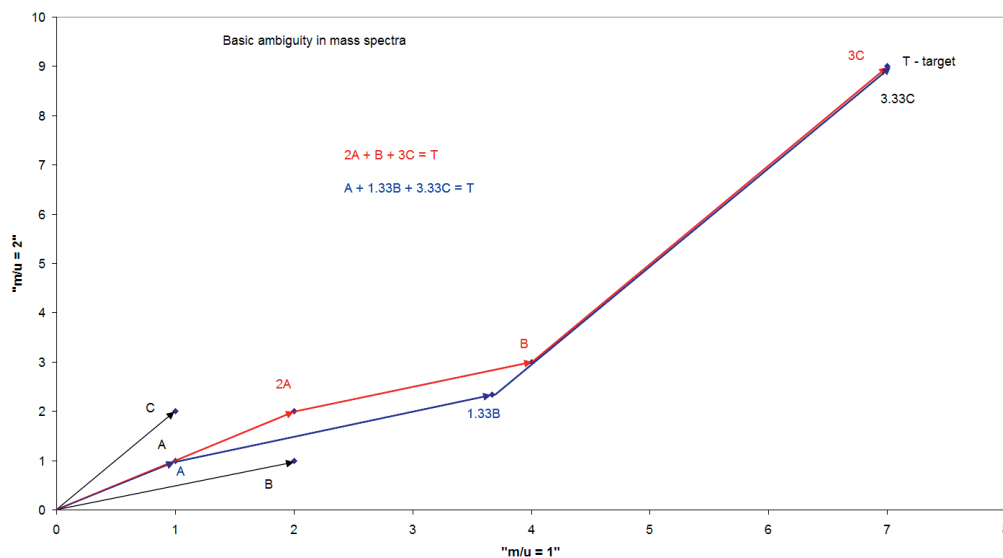


Figure 1: The illustration of mass-spectra ambiguity

Slika 1: Ilustracija večličnosti masnega spektra

When the mass spectra are considered to be vectors, the ambiguity in its interpretation can be clearly demonstrated.

1.3 Interpretation of mass spectra for residual gas analysis – general considerations

It is obvious that from knowing only the resulting mass spectra it is next to impossible to reconstruct the proper contribution for each constituent spectrum.

The first step in the mass-spectra analysis is the identification of the residual gases that constitute the observed spectrum.

It is to be expected that the major residual constituents in vacuum systems are inorganic gases, such as H_2O , H_2 , CO_2 , CO , O_2 , N_2 , Ar , Ne , etc. Most inorganic gas molecules found in vacuum systems are composed of 2, 3, or 4 atoms. Their fragment patterns are therefore simple. These gases are relatively easy to identify in the overall mass spectrum.

There are some simple rules at the basis of the experimental work with mass spectrometry. These rules are extremely important for the understanding of mass-spectra properties. As such they can provide the valuable additional information needed for a more accurate mass-spectra identification.³²

- The spectra of simple inorganic gas molecules generally have even mass numbers. For these inorganic gas molecules a simple ionization is more probable than fragmentation.
- The parent peaks of almost all inorganic gases are the largest. They are found at an even mass number.
- Mass spectra should not contain large quantities of highly reactive gases (F_2 , O_2 , etc.). Generally these gases are most easily adsorbed by the vacuum system walls. In cases where the mass-spectra analysis gives large quantities of such gases, the algorithm should be capable of suppressing their quantities (or to signal possible erroneous events, e.g., vacuum-system leaks)
- If the mass peak at $m/u = 14$ (mostly N^+) is larger than the mass peaks at $m/u = 12$ and 16 (C^+ and O^+ from CO) then an air leak is very possible.
- The noble gases, He , Ne , Ar , etc., are usually not the dominant residual gases. They have a highly unreactive nature and they can scarcely be found in the atmosphere. Like with the atmosphere, in vacuum systems where gas reactivity is important for efficient pumping, noble gases (especially Ar and Ne) can be observed in appreciable quantities.
- A $m/u = 1$ peak greater than a few percent of $m/u = 2$ is often a sure indication of significant amounts of water vapor in the system. Please note that except for water, H^+ is not a significant fragment of any gas usually seen in a vacuum system. Even with the standard spectra for H_2O , the $m/u = 1$ is not plotted. The partial pressures of gases like H_2O , CO , CO_2 ,

etc. can provide useful information about the progress of vacuum-system bakeouts.

- A mass spectrum with a series of peaks that are separated by $\Delta m/u = 14$ or $\Delta m/u = 15$ indicates that there are hydrocarbons present in the vacuum system.
- Organic gases are unstable, thus the parent peaks may not appear in the spectrum. Fragments often represent the dominant mass peaks.
- Fragments with odd m/u numbers are expected to be the most populated.
- The m/u peaks 57, 55, 53; or 43, 41, 39; or 29, 27; or combinations of these are a sure indication of organic species in the vacuum system. If the highest m/u of each of these series is the largest peak then the organic is of the saturated type, (forepump oil). If a lower mass number in the series is the largest, this is generally an indication of some degree of unsaturation (Multi-bonded carbon-carbon) and can be caused by some polymeric substance.

1.4 Descent techniques

One of the numerous methods available to solve the problem of mass-spectrum identification is the use of the descent method. There are, in fact, several descent methods. In our research, the classical gradient method has been altered to the so-called pseudo-gradient descent method. We are well aware that any used method cannot overcome the basic problem of mass spectra: the ambiguity, therefore, is that one cannot expect the results of the proposed method to be flawless. Our aim is to find a method that will provide results that are good enough for practical use.

Descent techniques³³ are generally used for the solution of unconstrained minimization problems. In our case we are trying to find the combination of standard fragment patterns that yield the target, i.e., measured spectra. The standard fragment patterns are formalized as vectors, and we are seeking the set of multiplication factors, i.e., the weight that in the weighted sum forms the target vector. The distance from the calculated weighted sum to the target vector is measured by means of the classical Euclidean distance. The distance function is also often called the error function. This is the classical optimization problem. The unconstrained minimization problem is $\min D(\mathbf{w}, \mathbf{x})$. Here, a value of the variable vector $\mathbf{w} = (w_1, \dots, w_n)^T$ is sought that minimizes the objective, in our case the distance function $D(\mathbf{w}, \mathbf{x})$. The distance is calculated in m -dimensional Euclidean space, spanned over the unit vector $\mathbf{x} = (x_1, \dots, x_m)^T$. The problem $\min D(\mathbf{w}, \mathbf{x})$ is a special case of the general nonlinear programming or optimization problem. For the sake of simplicity, the distance function $D(\mathbf{w}, \mathbf{x})$ is often denoted by $D(\mathbf{w})$, bearing in mind that the distance function is primarily changed by \mathbf{w} , but is calculated in the space defined by \mathbf{x} .

A new descent direction is generated for each iteration. The descent iteration may involve the evaluation of the first and possibly the higher order derivatives of the objective distance function. Each step of the descent process yields a considerable improvement of the objective function.

The descent techniques involve a series of iterations that generally consist of three parts:

- 1) Determination of the direction of descent s^k ,
- 2) Determination of the descent length λ^k ,
- 3) Calculation of the descent step $w^{k+1} = w^k + \lambda^k w^k$.

The descent direction is an n -dimensional vector $s = (s_1, \dots, s_n)^T$. It exists in the same space as the weights do and represents the direction in which weights should be changed in order to decrease the distance function. At the k -th iteration the direction vector s^k originates at the current point w^k . It points in a descent or "downhill" direction, i.e., the value of the objective function decreases from w^k to a point at some distance in that direction. A unit vector s^k is said to be the descent direction, with respect to the objective function $D(w)$ at w^k , if there is a $\lambda_p > 0$, such that for all λ satisfying $\lambda_p \geq \lambda > 0$ we have

$$D(w^{k+1}) = D(w^k + \lambda s^k) < D(w^k) \quad (6)$$

If $D(w)$ is differentiable, s^k is a descent direction if

$$\lim_{\lambda \rightarrow 0} \frac{D(w^k + \lambda s^k) - D(w^k)}{\lambda} = \left. \frac{dD(w^k + \lambda s^k)}{d\lambda} \right|_{\lambda=0} = (s^k)^T \nabla D(w^k) < 0 \quad (7)$$

Where the $\nabla D(w)$ denotes the gradient of the objective function $D(w)$ evaluated at the point w^k . If $D(w)$ is differentiable, the product $(s_k)^T \nabla D(w)$ of the directions s^k and the gradient $\nabla D(w)$ is, by definition, the directional derivative of $D(w)$ in the direction s^k evaluated at w^k . If this directional derivative exists and is negative, then s^k is a descent direction.

The descent step-length λ is a scalar. It is a measure of the distance along the descent direction s^k between two successive iteration points w^k and w^{k+1} . In other words, at the k -th iteration a step of length λ^k is taken from point w^k to the point w^{k+1} .

The Descent Iteration

A typical descent iteration can be summarized in the following steps:

- 1) Compute a descent direction $s^k = (s_1^k, \dots, s_n^k)^T$
- 2) Compute a descent step-length λ^k
- 3) Perform a descent step to obtain a new point

$$w^{k+1} = w^k + \lambda^k s^k \quad (8)$$

The k -th descent step is defined as follows

$$\Delta w^k = w^{k+1} - w^k = \lambda^k s^k \quad (9)$$

A sequence of k descent steps leads from a starting point w^0 to a point w^k given by

$$w^k = w^0 + \sum_{l=0}^{k-1} \lambda^l s^l = w^0 + \sum_{l=0}^{k-1} \Delta w^l \quad (10)$$

At the k -th iteration a matrix $\Delta \bar{W}_k$ is defined by

$$\Delta \bar{W}_k = [\Delta w^0, \Delta w^1, \dots, \Delta w^{k-1}] \quad (11)$$

That is, the columns of $\Delta \bar{W}_k$ are the k descent steps $\Delta w^0, \Delta w^1, \Delta w^{k-1}$ preceding Δw^k .

The choice of the locally steepest direction as a descent direction leads to the steepest descent techniques. A locally steepest direction is obtained if the descent step Δw^k minimizes

$$\Delta D = \sum_{i=1}^n \frac{\partial D(w^k, x^k)}{\partial w_i} \Delta w_i^k \quad (12)$$

The distance between two points x^1 and x^2 in the m -dimensional space is defined as

$$D(x^1, x^2) = [(x^1 - x^2)^T A (x^1 - x^2)]^{1/2} \quad (13)$$

A is a positive definite $m \times m$ symmetric metric matrix. The definition of positive definiteness ensures that $D(x^1, x^2) > 0$ for any nonzero x^1 and x^2 . In general, it is not necessary to use the same unit of distance along the different coordinate axes.

The choice of I , $m \times m$ identity matrix as a metric, i.e., $A = I$, leads to the first-order steepest descent technique. Rescaling of the variables, e.g., $\bar{x} = Bx$, is equivalent to introducing a new metric matrix relative to the old coordinate system x . It is not necessary to use the same metric matrix throughout the whole iterative process of a descent technique.

2 EXPERIMENTAL WORK

Our aim is to design an algorithm that is able to perform qualitative and quantitative mass-spectra analysis. It is not possible to undertake the task without the formation of a virtual, simulated environment where various aspects of mass-spectra analysis can be addressed. In real vacuum systems, it is very expensive and time-consuming work to create a large amount of different situations to test primarily the algorithms. We want to establish the situation where the creation of analyzed spectra is completely under our control. Undivided attention can therefore be placed on the studied algorithms. All the problems are then concentrated on algorithms alone. When in a situation where the behaviour of the algorithm is very thorough, it can be implemented on real vacuum systems, giving the chance to assess its behaviour in real circumstances. At this stage of the implementation of the algorithm in "real life" is a process where the majority of problems is due to the used equipment, while the algorithm's behaviour is known, tested and understood.

Such an approach is not a very common one, and it is almost general practise that two problems are studied at

once, i.e., the mass spectra in a real situation and the algorithm.

2.1 The environment

The environment that binds together the generation of the mass spectra, the various algorithms for the mass-spectra identification, the experiments database and the evaluation procedures was established. The first step is to create the environment where static mass-spectra analysis can be performed.

By static, it is meant that the mass spectrum is created and the algorithm to analyze the spectrum is activated. During the analysis time, the mass spectrum is fixed. Our intention is to create the environment where mass spectrum is generated as the time variant spectrum, i.e., dynamic.

The environment (Figure 2) enables the study of behaviour of different algorithms in noisy conditions.

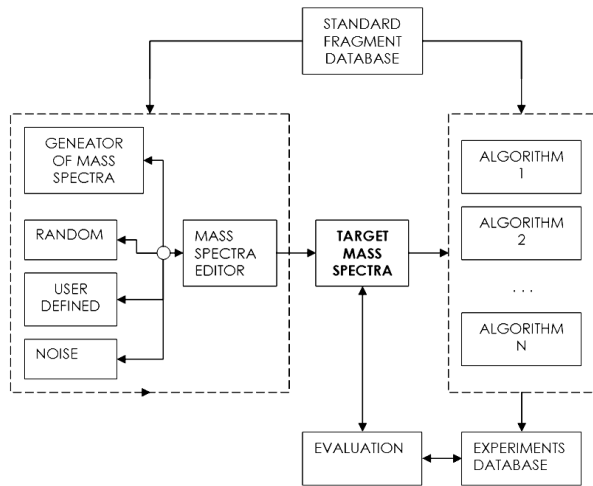


Figure 2: The environment for the generation of mass spectra, algorithms for the mass-spectra constituents analysis, the experiments database and evaluation

Slika 2: Okolje za generiranje masnih spektrov, algoritmi za analizo, podatkovna baza za shranjevanje podatkov poskusov in njihovih obdelav

m/u	1	2	3	4	5	6	7	8	9	10	11	12	13
	H2	He	CH4	NH3	H2O	Ne	C2H2	C2H4	N2	CO	C2H6	NO	CH4O
1	0.0500	0.0000	0.0000	0.0000	0.0000	0.0000	0.0000	0.0000	0.0000	0.0000	0.0000	0.0000	0.0000
2	1.0000	0.0000	0.0000	0.0000	0.0000	0.0000	0.0000	0.0000	0.0000	0.0000	0.0000	0.0000	0.0000
3	0.0000	0.0000	0.0000	0.0000	0.0000	0.0000	0.0000	0.0000	0.0000	0.0000	0.0000	0.0000	0.0000
4	0.0000	1.0000	0.0000	0.0000	0.0000	0.0000	0.0000	0.0000	0.0000	0.0000	0.0000	0.0000	0.0000
5	0.0000	0.0000	0.0000	0.0000	0.0000	0.0000	0.0000	0.0000	0.0000	0.0000	0.0000	0.0000	0.0000
6	0.0000	0.0000	0.0000	0.0000	0.0000	0.0000	0.0000	0.0000	0.0000	0.0000	0.0000	0.0000	0.0000
7	0.0000	0.0000	0.0000	0.0000	0.0000	0.0000	0.0000	0.0000	0.0000	0.0000	0.0000	0.0000	0.0000
8	0.0000	0.0000	0.0000	0.0000	0.0000	0.0000	0.0000	0.0000	0.0000	0.0000	0.0000	0.0000	0.0000
9	0.0000	0.0000	0.0000	0.0000	0.0000	0.0000	0.0000	0.0000	0.0000	0.0000	0.0000	0.0000	0.0000
10	0.0000	0.0000	0.0000	0.0000	0.0000	0.0000	0.0000	0.0000	0.0000	0.0000	0.0000	0.0000	0.0000
11	0.0000	0.0000	0.0000	0.0000	0.0000	0.0000	0.0000	0.0000	0.0000	0.0000	0.0000	0.0000	0.0000
12	0.0000	0.0000	0.0240	0.0000	0.0000	0.0000	0.0250	0.0210	0.0000	0.0450	0.0000	0.0000	0.0000
13	0.0000	0.0000	0.0770	0.0000	0.0000	0.0000	0.0560	0.0350	0.0000	0.0000	0.0000	0.0000	0.0000
14	0.0000	0.0000	0.1550	0.0220	0.0000	0.0000	0.0020	0.0630	0.0720	0.0050	0.0340	0.0750	0.0000
15	0.0000	0.0000	0.8590	0.0750	0.0000	0.0000	0.0000	0.0000	0.0000	0.0000	0.0460	0.0240	0.0000
16	0.0000	0.0000	1.0000	0.8000	0.0110	0.0000	0.0000	0.0000	0.0000	0.0090	0.0000	0.0150	0.0000
17	0.0000	0.0000	0.0120	1.0000	0.2300	0.0000	0.0000	0.0000	0.0000	0.0000	0.0000	0.0000	0.0000
18	0.0000	0.0000	0.0000	0.0040	1.0000	0.0000	0.0000	0.0000	0.0000	0.0000	0.0000	0.0000	0.0190
19	0.0000	0.0000	0.0000	0.0000	0.0010	0.0000	0.0000	0.0000	0.0000	0.0000	0.0000	0.0000	0.0000
20	0.0000	0.0000	0.0000	0.0000	0.0030	1.0000	0.0000	0.0000	0.0000	0.0000	0.0000	0.0000	0.0000
21	0.0000	0.0000	0.0000	0.0000	0.0030	0.0000	0.0000	0.0000	0.0000	0.0000	0.0000	0.0000	0.0000
22	0.0000	0.0000	0.0000	0.0000	0.0000	0.9990	0.0000	0.0000	0.0000	0.0000	0.0000	0.0000	0.0000
23	0.0000	0.0000	0.0000	0.0000	0.0000	0.0000	0.0000	0.0000	0.0000	0.0000	0.0000	0.0000	0.0000
24	0.0000	0.0000	0.0000	0.0000	0.0000	0.0000	0.0560	0.0370	0.0000	0.0000	0.0000	0.0000	0.0000
25	0.0000	0.0000	0.0000	0.0000	0.0000	0.0000	0.2010	0.1170	0.0000	0.0000	0.0420	0.0000	0.0000

Figure 3: The standard mass-spectra pattern database (section)

Slika 3: Podatkovna baza standardnih masnih spektrov (izrez)

Name	Size
Exp1_1	42 KB
Exp1_2	42 KB
Exp1_3	42 KB
Exp1_4	42 KB
Exp1_5	42 KB
Exp1_6	42 KB
Exp1_7	42 KB
Exp1_8	42 KB
Exp1_9	42 KB
Exp1_10	42 KB
Exp1_11	42 KB
Exp1_12	42 KB
Exp1_13	42 KB
Exp1_14	42 KB
Exp1_15	42 KB
Exp1_16	42 KB
Exp1_17	42 KB
Exp1_18	42 KB
Exp1_19	42 KB
Exp1_20	42 KB
Exp1_21	42 KB
Exp1_22	42 KB
Exp1_23	42 KB
Exp1_24	42 KB
Exp1_25	42 KB

Figure 4: The structure of the experiments database

Slika 4: Struktura podatkovne baze poskusov

The core of the environment is the database, including the standard fragment patterns for molecular ions and/or fragment ions (Figure 3).

In our experiments, 47 gases, with m/u ratios from 1 to 47 formed the database. However, by no means is the system limited to these figures. The database leaves the user to freely add or remove the standard fragmentation patterns. The database is a vital element of the environment since it provides the standard fragment patterns as vectors. The data is used for the generation of the mass spectra, which is done in two different ways. One is random generation, where the multiplication factors w_j from equation (4) are chosen randomly. Another option is the user-defined selection of w_j , where the user can make the selection of gases to compose the vacuum-system atmosphere. The third option makes it possible to add noise to the generated spectrum – equation (5). Once the spectrum is generated it can be edited by the user.

The spectrum-generation process results in the vector annotation of mass spectra. As such it is prepared to be analyzed by various algorithms.

Each experiment is saved in the so-called experiments database, which consists of separate files, each for a separate experiment. Figure 4 depicts the structure of the experiments database.

Each experiment file holds the data of the generated spectrum and the results of its analysis by the algorithm.

The following data and the graphical representations describe the experiment:

- 1) Each experiment starts with the random generation (Figure 2) of virtual vacuum system atmosphere composition in terms of multiplication factors w . Multiplication factors are stored, and shown in

ITERATION	DISTANCE TO TARGET	M/e	COMPOSITION	CALCULATION	GAS	COMPOSITION	CALCULATION	NUMBER OF ITERATIONS
1	43.0708193	1	0.3528	0.3827	1H2	7.8555	7.8555	2015
51	0.33384531	3	0.0000	0.0000	2He	5.3342	5.3337	
102	0.511781417	4	5.3342	5.3337	3CH4	5.7952	5.7231	RMS error
153	0.418772299	5	0.0000	0.0000	4NH3	2.8956	2.8516	
204	0.387576708	6	0.0000	0.0000	5H2O	3.9155	3.9034	
255	0.323156221	7	0.0000	0.0000	6Ne	7.7474	7.7497	
306	0.295292137	8	0.0000	0.0000	7C2H2	0.1402	0.4475	
357	0.266205987	9	0.0000	0.0000	8C2H4	7.6072	6.2493	
408	0.249817983	10	0.0000	0.0000	9N2	8.1449	5.8928	
459	0.228797754	11	0.0000	0.0000	10CO	7.0904	8.4564	
510	0.219576477	12	1.3889	1.3213	11C2H6	0.4533	2.6963	
561	0.205376054	13	0.9045	0.8591	12NO	4.1403	2.8292	
612	0.200806236	14	3.2771	3.2439	13CH4O	8.6262	8.2227	
663	0.190043284	15	6.0919	6.1132	14O2	7.9048	8.1767	
714	0.187456842	16	10.5885	10.5846	15H2S	3.7354	3.7354	
765	0.178423953	17	4.6728	4.6759	16A	9.6195	9.6208	
816	0.176274957	18	3.6169	3.6157	17C3H6	8.7145	8.7023	
867	0.166873905	19	0.1795	0.1888	18C3H8	0.6624	0.6353	
918	0.167444196	20	8.7857	8.7882	19CO2	9.4956	7.8719	
969	0.159892937	21	0.0225	0.0232	20H2O	3.6429	5.3161	
1020	0.158987269	22	0.8809	0.8617	21C2H4O	5.2487	5.1593	
1071	0.15198037	23	0.0000	0.0000	22C2H5O	7.6711	8.0771	
1122	0.151120278	24	3.7133	3.3988	23H2	0.5365	0.8638	
1173	0.144489602	25	1.1931	1.1865	24CH2O2	5.9248	5.6398	
1224	0.143716745	26	7.5891	7.5947	25CAH18	4.6870	4.7032	
1275	0.137419367	27	12.8905	12.8851	26C3H8O	2.8817	2.8392	
1326	0.136706161	28	28.8744	28.8891	27C2HCl3	6.2270	6.2263	
1377	0.130718876	29	21.7338	21.7257				
1428	0.130053973	30	6.5761	6.5763				
1479	0.124355166	31	16.3175	16.3159				
1530	0.123688152	32	15.3253	15.3252				
1581	0.118834389	33	1.8628	1.8633	9N2	2.2527	2.2527	
1632	0.117724759	34	3.7670	3.7681	11C2H6	2.2428	2.2428	
1683	0.113512133	35	2.5779	2.5777	20N2O	1.6759	1.6759	
1734	0.112584044	36	0.1885	0.1885	18C2H4	1.6237	1.6237	
1785	0.109204349	37	2.0448	2.0445	12NO	1.4477	1.4477	
1836	0.107581023	38	1.8748	1.8749				
1887	0.104849186	39	6.2295	7.2422				
1938	0.103727511	40	12.1625	12.1622				
1989	0.100912234	41	10.3545	10.3514				
		42	7.5788	7.5776				
		43	9.7785	9.7754				
		44	16.2742	16.2763				
		45	5.8164	5.8077				
		46	5.1170	5.1251				
		47	1.6071	1.6072				

Figure 5: The data stored in the experiment file
 Slika 5: Podatki, shranjeni v datoteki, ki pripadajo enemu poskusu

Figure 5 in rightmost table (the column entitled COMPOSITION). The same data is graphically represented in Figure 6, lower graph. Please note that the randomly generated data is presented as the left (blue) bars in a bar graph.

- Once the randomly generated composition is known, the mass spectrum is formed (Equation 4), where standard fragmentation patterns (Figure 3) and the corresponding weights are combined to form the spectra (the column COMPOSITION in the middle table of Figure 5). The same data is graphically shown in Figure 6 middle bar graph. Again the generated spectrum is shown by the left (blue) bars. These data form the so called "target" for the mass spectrum analysis algorithm.
- At this stage the spectrum generation process is complete the data is stored and graphically presented. The reverse process of spectrum analysis can commence. The pseudo gradient algorithm (or any other) works on a spectrum (column COMPOSITION in middle table of Figure 5) and seeks the multiplication factors w that best fit the target spectrum. The calculated weights are stored in column CALCULATION in rightmost table of Figure 5. The same data is graphically presented in lower bar graph (the right (red) bars) of Figure 6. Similarly the calculated spectrum is stored in column CALCULATION in middle table of Figure 5, and graphically presented in middle bar graph (again the right (red) bars).
- The data that describe the convergence of the used algorithm (the leftmost table of Figure 5) consisting of consequent iteration counter (column ITERATION), and the current distance to the given target spectrum (column DISTANCE TO TARGET) is stored. The same data is graphically represented in Figure 6 – upper graph.

- The lower right table in Figure 5 summarizes the five mass spectra constituents where the errors produced by the tested algorithm were absolutely the largest.
- In addition the number of iterations required to fulfil the preset algorithm termination criteria, and the overall RMS error for all mass spectra constituents (Figure 5 upper right part) are presented.

In this stage, the system is prepared to generate and analyze static mass-spectra vectors. The design of the environment is such that a dynamic module can easily be added in order to generate and simultaneously analyze the time profiles of the mass spectra.

2.2 The pseudo-gradient descent algorithm

The classical gradient approach requires the calculation of the first derivative of the distance to the target function $D(w, x)$. The distance function in the $D(. , x)$ is the standard Euclidean distance (13), unfortunately the dependence $D(w, .)$ is more complicated. In our approach we have decided to calculate the differences produced by the small changes of w rather than produce the necessary step directions from the formal first derivative of the function. Therefore, the formal gradient descent algorithm becomes the pseudo-gradient algorithm.

- Read the data from the standard fragment pattern database.
- Calculate increments for all gases (These are the differences used for the calculation of pseudo gradients. Increments mean that each m/u component of the standard fragment pattern is multiplied by a small value – 0.001).
- Define the memory data space for the error function. For each iteration, the error value represents the distance from the current mass spectrum produced as the result of current weight values, and the target spectrum. The error function is the dependence of the error and the iteration counter.
- Read the target spectrum.
- Set the initial weights for all possible gases included in the database to 0.01 – this is the starting point where the gradient descent starts.
- Calculate the first distance from the spectra that uses the initial weights and the target spectrum.
- Calculate the step-length λ^k for the current iteration. The algorithm uses the variable step-length λ^k , which is set to 1/20 of the current distance (Equation 13). This step is necessary to ensure the smooth convergence of the algorithm.
- Start the iteration loop, which is executed until the actual distance remains larger than 0.1 or the repetition counter remains under 3000.
 - Calculate the differences in distance that are caused by making very small differences – increments in the gas factors – weights. Both directions are

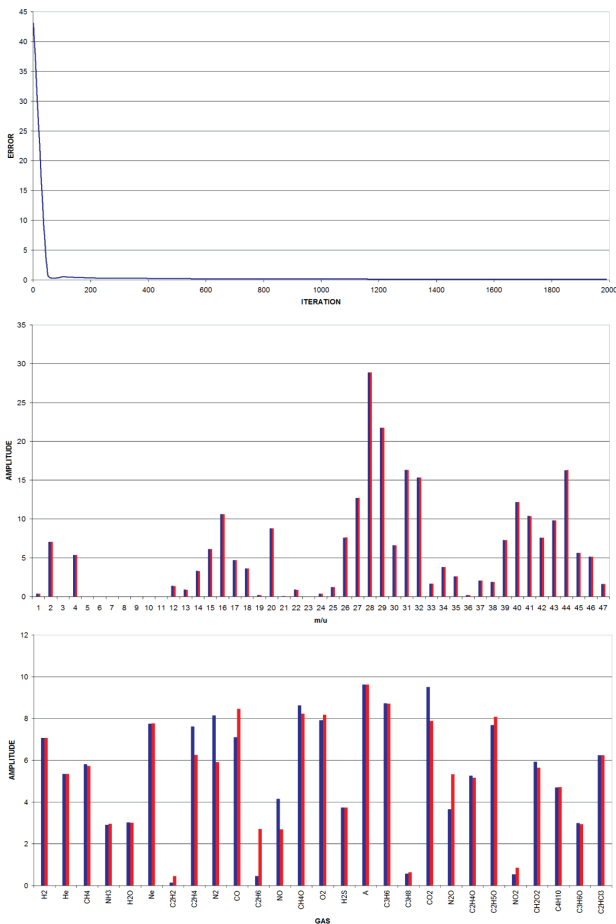


Figure 6: The graphical representation of mass-spectra analysis data
Slika 6: Grafična predstavitev podatkov analize masnih spektrov

probed and the change that produces the reduction of distance to the target is maintained. Special care must be taken during reduction, while the weights for each constituent gas must always remain positive. The lowest possible weight value is therefore 0.

- o Keep only incremental changes that produce a reduction of the distance to the target.
- o Find the direction of downhill change – the pseudo gradient (12).
- o Use the step-length and direction vector to form the new, closer set of weights.
- o Calculate the new distance (6).
- o Calculate the new step-length λ^{k+1} , again as 1/20 of the actual distance to the target.
- As the algorithm executes iterations, the data structures (**Figures 5 and 6**) are consequently filled with data.

3 RESULTS AND DISCUSSION

The mass spectrum is the linear superposition of the individual peak heights of the constituent gases. The

standard fragmentation patterns of the constituent gases are not orthogonal; therefore, the algorithms that are used for the mass-spectra identification produce ambiguous results.

The experiment was designed to probe the pseudo-gradient descent algorithm for 1000 randomly generated spectra.

The pseudo gradient algorithm shows excellent convergence. In all 1000 examples the convergence was without any detected instabilities. For all the performed tests the error function is a monotonously decreasing one. It is important to note that the algorithm seeks the values for weights that produce the mass spectrum as close as possible to the given spectra. This means that the end spectrum is always as near as possible to the preset error tolerance in the m/u "space", while the actual weight values can sometimes produce serious errors in the weight space.

The average starting error for all 1000 tests was 23.84, and the error tolerance to stop the algorithm was arbitrarily set to 0.1.

A total of 142 tests out of 1000 did not fulfil the pre-set condition of error tolerance in 3000 iterations. All the others did the job in an average 802 iterations. The average error for the 142 failed tests was 0.14. The problem of 142 unfinished tests could be easily solved by moving the number of allowed iterations from 3000 to some higher value. The arbitrarily set error tolerance is also very easy to change – according to the needs posed by the concrete problem.

Figure 7 plots the root-mean-square errors (of the calculated weights) for all the constituent gases and for all 1000 tests. Since the mass spectrum analysed by the tested algorithm is always exactly known (it is generated by the mass-spectrum generator), the error of the performed analysis can always be calculated (not only assessed, as is the case during the analysis of real data).

The root-mean-square error (RMS) is calculated by equation 14.

$$E_j = \sqrt{\frac{\sum_{i=1}^N (w_{ij} - wt_{ij})^2}{N}} \quad (14)$$

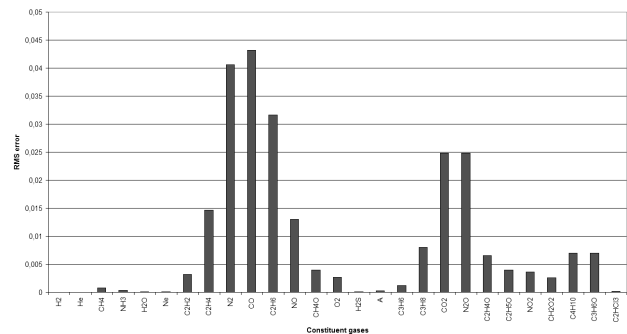


Figure 7: Root-mean-square error for the calculated weights of the constituent gases

Slika 7: Srednjekvadratna napaka izračunanih uteži plinov, ki sestavljajo atmosfero v vakuumskem sistemu

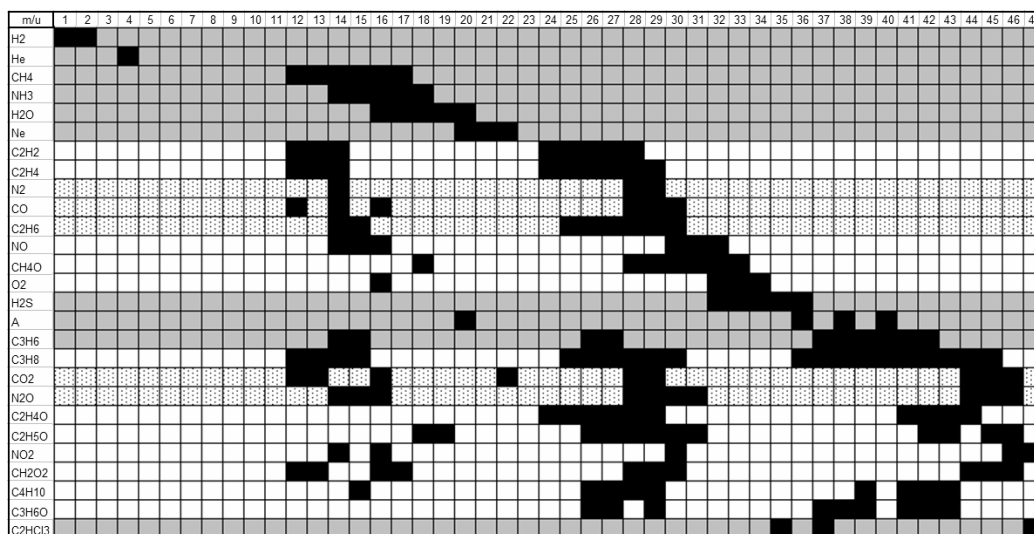


Figure 8: Mass-spectra standard fragment patterns – the black squares represent the presence of a peak
Slika 8: Standardni masni spektri – črni kvadrati predstavljajo prisotnost posameznega vrha v spektru

Where E_j represents the RMS error for the j -th constituent gas, the index i is the test counter that runs from 1 to 1000, w_{ij} is the weight of the j -th constituent gas (the result of the analysis) during the i -th test, wt_{ij} is the target weight (of the generated spectrum) of the j -th constituent gas during the i -th test. The value for N is, in our case, 1000.

From **Figure 7** we can conclude that there is a group of constituent gases where analysis gives excellent results, almost without noticeable errors. Such gases are: H_2 , He, CH_4 , NH_3 , H_2O , Ne, H_2S , A, C_3H_6 , C_2HCl_3 .

The group of constituent gases with a "medium" error would consist of C_2H_2 , C_2H_4 , NO, CH_4O , O_2 , C_3H_8 , C_2H_4O , C_2H_6O , NO_2 , CH_2O_2 , C_4H_{10} , C_3H_6O .

The largest errors are detected for N_2 , CO, C_2H_6 , CO_2 , N_2O .

The reason for the errors is mainly in the mentioned mass-spectra ambiguity. Putting it another way: the standard fragmentation patterns for the gases overlap, so it is very hard to distinguish which is which.

In **Figure 8** the existence of the peak in the fragment pattern is symbolized as a black square. The constituent gasses that can be recognised precisely are shown with a grey background, while the dotted area represents the gasses with the poorest results.

4 CONCLUSION

The presented work is a foundation for the comprehensive study of mass-spectrum analysis techniques. It introduces several new ideas in the field of mass spectrometry. The most important concept is the virtual environment that provides the mass-spectrum generator, the space for the various algorithms that can test various approaches to the mass-spectrum identification, the database of the achieved results, which is extremely important for the comparison of different algorithms, the

backbone for the dynamic mass-spectra generation and analysis. The environment also makes it possible to analyse the immunity to noise for all algorithms.

The main purpose of the virtual environment is the controlled mass-spectra data, which allows an exact evaluation of the errors produced by the studied algorithm. Normally, such algorithms are developed and tested directly on "live" data, which combines the problems that originate from the measurements environment with those produced by the algorithm, often without a real chance of dividing the two. The approach with the virtual environment makes it possible to study problems regarding the algorithms alone, prior to applying them to the "live" environment.

Such an approach also makes it possible to run numerous tests in a relatively short time, which would never be possible with real vacuum systems.

The pseudo-gradient descent algorithm for mass-spectrum identification was proposed and tested. The results are promising, taking into account that additional work will be needed to overcome the mass-spectrum ambiguity. The steps that will be tested are:

- 1) Introduction of "common knowledge" regarding the mass spectrometry and identification techniques.
- 2) Finding out how does the selection of the initial point influence the algorithm's performance.
- 3) Introduction of several steps in the identification process – after the first run of the algorithm the constituent gasses that can be detected with the highest precision should be removed and the algorithm should be run again for the remaining gasses. This step should be repeated several times.

Another problem is the study of a dynamic mass spectrum, i.e., the analysis of mass-spectrum time

profiles. The virtual environment is prepared to enable such studies.

5 REFERENCES

- ¹ K. Schulz, K. Schlenz, S. Malt, R. Metasch, W. Römhild, J. Dreßler, D. W. Lachenmeier, *Journal of Chromatography A*, 1211 (2008), 1–2, 113–119
- ² I. S. Sheoran, A. R. S. Ross, D. J. H. Olson, V. K. Sawhney, *Plant Science*, 176 (2008), 99–104
- ³ J. Chena, X. Li, C. Suna, Y. Pana, U. P. r Schlunegger, *Talanta*, 77 (2008), 152–159
- ⁴ A. Cingöz, F. Hugon-Chapuis, V. Pichon, *Journal of Chromatography A*, 1209 (2008), 95–103
- ⁵ <http://www.matrixscience.com/>
- ⁶ H. M. Santosa, C. Mota, C. Lodeiroa, I. Mouraa, I. Isaacb, J.L. Capelo, *Talanta*, 77 (2008), 870–875
- ⁷ <https://products.appliedbiosystems.com/>
- ⁸ <http://www.thermo.com/com/cda/product/detail/0,1055,1000001009250,00.html>
- ⁹ T. Murakamia, T. Kawasakia, A. Takemuraa, N. Fukutsua, N. Kishia, F. Kusud, *Journal of Chromatography A*, 1208 (2008), 164–174
- ¹⁰ http://www.scientific-computing.com/products/product_details.php?product_id=207
- ¹¹ S. Shia, Y. Zhaob, H. Zhouc, Y. Zhanga, X. Jianga, K. Huanga, *Journal of Chromatography A*, 1209 (2008), 145–152
- ¹² <http://www.chem.agilent.com>
- ¹³ <http://scientific-computing.com>
- ¹⁴ <http://www3.appliedbiosystems.com>
- ¹⁵ L. Lionetto, A. M. Lostia, A. Stigliano, P. Cardelli, M. Simmaco, *Clinica Chimica Acta*, 398 (2008), 53–56
- ¹⁶ M. Mezcuca, C. Ferrer, J. F. García-Reyes, M.J. Martínez-Bueno, M. Sigrist, A. R. Fernández-Alba, *Food Chemistry*, 112 (2009), 221–225
- ¹⁷ K. M. Robinson, J. T. Morr, J.S. Beckman, *Archives of Biochemistry and Biophysics*, 423 (2004), 213–217
- ¹⁸ M. Y. Zhanga, N. Kagana, M. A. Sungb, M. M. Zaleskab, M. Monaghanb, *Journal of Chromatography B*, 874 (2008), 51–56
- ¹⁹ W. C. Chau, J. Wu, Z. Cai, *Chemosphere*, 73 (2008), S13–S17
- ²⁰ X. Deng, G. Gao, S. Zheng, F. Li, *Journal of Pharmaceutical and Biomedical Analysis*, 48 (2008), 562–567
- ²¹ L. Qi, J. Cao, P. Li, Q. Yu, X. Wen, Y. Wang, C. Li, K. Bao, X. Ge, X. Cheng, *Journal of Chromatography A*, 1203 (2008), 27–35
- ²² H. Qu, B. Li, X. Li, G. Tu, J. Lü, W. Sun, *Microchemical Journal*, 89 (2008), 159–164
- ²³ E. Vanlaere, K. Sergeant, P. Dawyndt, W. Kallow, M. Erhard, H. Sutton, D. Dae, B. Devreese, B. Samyn, P. Vandamme, *Journal of Microbiological Methods*, 75 (2008), 279–286
- ²⁴ R. Wihlborg, D. Pippitt, R. Marsili, *Journal of Microbiological Methods*, 75 (2008), 244–250
- ²⁵ J. Radjenović, S. Péreza, M. Petrović, D. Barcelóa, *Journal of Chromatography A*, 1210 (2008), 142–153
- ²⁶ R. Oprean, L. Oprean, M. Tamas, R. Sandulescu, L. Roman, *Journal of Pharmaceutical and Biomedical Analysis*, 24 (2001), 1163–1168
- ²⁷ <http://www.sisweb.com/software/ms/nist.htm>
- ²⁸ <http://eu.wiley.com/WileyCDA/Section/id-301546.htm>
- ²⁹ A. Calcatelli, M. Bergoglio, D. Mari, *Vacuum*, 81 (2007), 1538–1544
- ³⁰ <http://www.hiddenanalyticalinc.com>
- ³¹ <http://www.extrel.com>
- ³² M. J. Drinkwine, D. Lichtman, *Partial pressure analyzers and analysis*, American Vacuum Society, Milwaukee, 1979
- ³³ J. L. S. Samuel, *Iterative methods for nonlinear optimization problems*. Prentice HALL, Englewood Cliffs, 1972

SCHEMES OF METAL-WORKING PROCESSES AND THE RELATED TRIBOLOGICAL EQUATIONS OF FLUID MECHANICS

SHEME PROCESOV PREDELAVE KOVIN IN TRIBOLOŠKE ENAČBE MEHANIKE FLUIDOV ZANJE

Dušan Čurčija, Ilija Mamuzić

University of Zagreb, Faculty of Metallurgy Sisak, Aleja narodnih heroja 3, 44000 Sisak, Croatia
mamuzic@simet.hr

Prejem rokopisa – received: 2007-10-15; sprejem za objavo – accepted for publication: 2008-10-02

We present a survey of the most frequently used equations for applications in cold drawing and rolling, for smooth and rough surfaces, for the effect of lubricant inertial forces, for more advanced theoretical solutions as well as the equations for cold drawing with a solid lubricant and the combination solid lubricant-emulsion. The compression processes are described using cylindrical coordinates. Also, the basic equations for the flowing of the lubricant on inclined planes related to screw rolling and for the forming of metals with fluids are given.

Key words: lubrication, metal forming Reynolds differential equation, Monte-Carlo method

Podan je pregled najbolj pogosto uporabljenih enačb pri hladnem valjanju in vlečenju, za gladke in hrapave površine, za vpliv vztrajnostnih sil, za bolj napredne teoretične rešitve in enačb za vlečenje s trdnim mazivom in kombinacijo trdo mazivo – emulzija. Tlačni procesi so opisani s cilindričnimi koordinatami. Podane so tudi osnovne enačbe za tok maziva na nagnjeni površini, ki se nanašajo na navojno valjanje in za oblikovanje kovine s fluidi.

Ključne besede: mazanje, preoblikovanje kovin, Reynoldova diferencialna enačba, metoda Monte Carlo

1 INTRODUCTION

The investigations and development of modern plastic working technology covers the following topics: physical modelling and simulation, computer simulation and characteristics and the behaviour of the material during processing.

The gradients representing the changes of temperature and mechanical stresses are greater for a greater per-pass (partial) deformation. In **Figure 1** the compression force F , the heat flow H , the deformation direction D and the rolling direction K for simple rolling

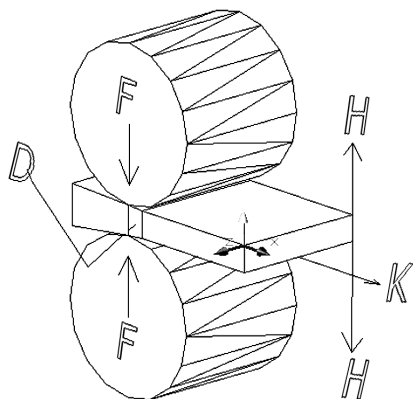


Figure 1: Directions of the gradients in a physical simulation of metal rolling¹

Slika 1: Smeri gradientov pri fizikalni simulaciji valjanja kovin¹

are shown. The physical simulation, as a laboratory representation of the process, is based on the law of similarity and allows only a limited extrapolation. The simulation of the rolling process occurs by applying the principles of viscoplasticity and the use of analytical solutions increases with the rapid development of modern theoretical and experimental methods for the investigation of the plastic deformation of metals. A torsional plastometer was applied with success for the determination of the rolling force (**Figure 2**) and the obtained data can be applied for the correction of the

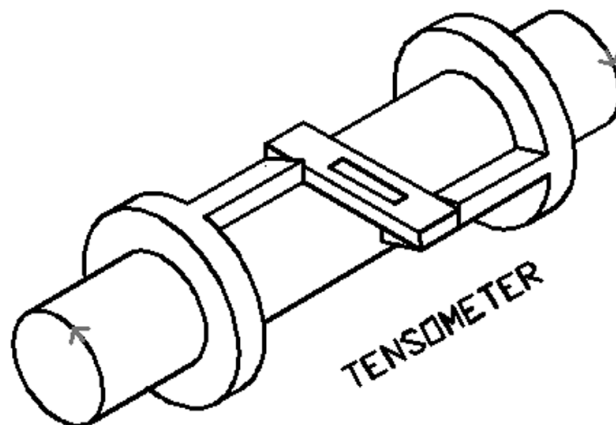


Figure 2: Torsionmeter²

Slika 2: Merilec torzije²

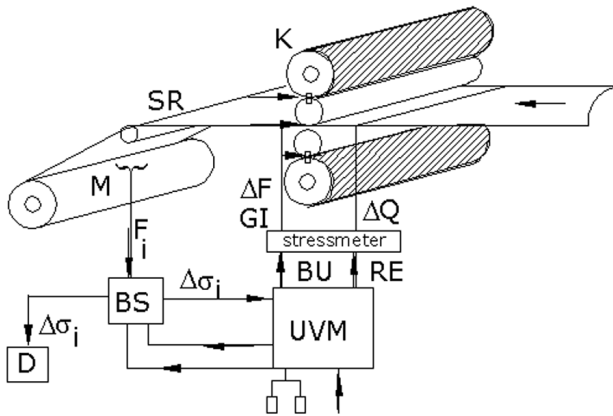


Figure 3: Measuring the surface stresses on a sheet's surface
Slika 3: Merjenje površinskih napetosti na traku

calibration as well as the regulation of the rolling gap for continuous rolling stands.

In **Figure 3** a scheme is given for measuring the stresses on the sheet surface with a stressmeter³.

2 FLUID MECHANICS

The concept of the boundary layer (**Figure 4**) was proposed by Prandl in 1904. The thickness of the fluid layer (δ_x) can differ significantly from the flowing line 2. The layer has, however, a constant flow velocity. Below the laminar part of the layer 3, the flowing velocity (v) decreases and on the solid surface the fluid is at a standstill, ϕ is the boundary laminary layer, ω is the transition area and κ is the turbulent part of the boundary layer 1. The representation in **Figure 3** shifts the Navier-Stokes and Reynolds equations in the domain of velocity.

The use of emulsions for the plastic working of metals led to a significant lowering of production costs and to savings with expensive natural oils. In **Figure 5** the equilibrium is shown for the surface tension of a drop of light liquid on the surface of a heavier liquid:

$$\sigma_{12} = \sigma_{13} \cos\theta_2 + \sigma_{23} \cos\theta_1 \quad (1)$$

For $\theta_2 \rightarrow 0$ the adhesion work (W) is calculated using the Jung-Dupre equation

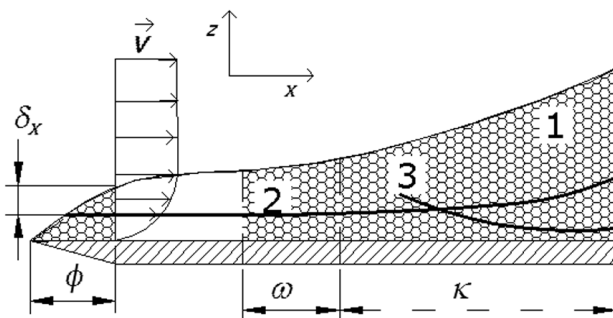


Figure 4: Boundary layer for the flow of fluid on the flat plane⁴
Slika 4: Mejni sloj za tok maziva na ravni površini⁴

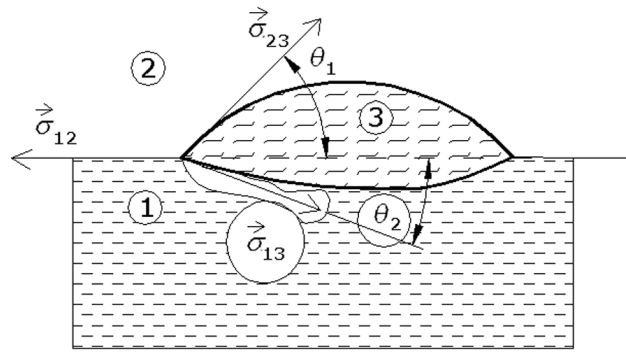


Figure 5: Equilibrium of the surface tension σ for a light liquid (3) on a heavier liquid (1) in air 2⁵

Slika 5: Ravnotežje površinske napetosti σ za lahko tekočino (3) na težji tekočini (1) in na zraku (2)⁵

$$W = \sigma_{23} (1 + \cos\theta_1) \quad (2)$$

Investigations of the use of equation (2) in metallurgy were carried out by Ju. P. Abdulov⁶. In a fluid mechanical metallurgical investigation different equations are used for the flat (**Figure 5**) and for the inclined plane (**Figure 6**).

The case of lubrication of a surface with vertical movement is met, also (**Figure 7**).

In this work we will examine the fluid friction (friction with hydrodynamic lubricant), for which Newton's law is applied:

$$F = z S v / h \quad (3)$$

where F is the friction force, z is the flowing capacity, S is the sliding surface, v is the velocity of the relative transfer, and h is the thickness of the lubricant layer.

For a description of the case of liquid friction in the plastic deformation of metals the Nady equation is used. Let us start with an analysis on the basis of **Figure 8**. The sheet of thickness h is covered with the lubricant layer $\epsilon(x)$ ahead of the section entering the deformation zone, for a wedge-shaped rolling gap a with the gap

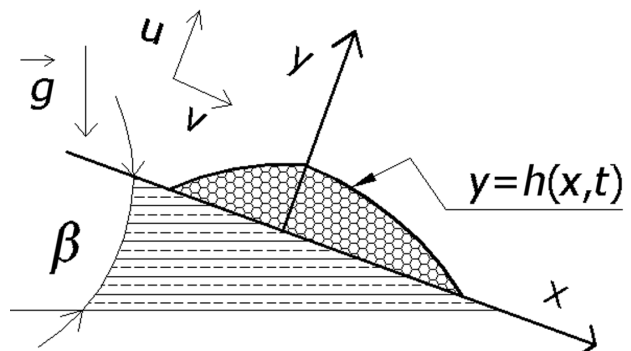


Figure 6: Shaping of a drop of liquid on an inclined plane⁷ where x, y are the Descartes coordinates; u, v are the corresponding flowing velocities; t is the time; g is the acceleration due to gravity; and β is the angle of inclination

Slika 6: Oblikovanje kapljice tekočine na nagnjeni površini x, y Descartesove koordinate; u, v hitrosti pretokov; t čas; g konstanta gravitacije; β kot nagiba

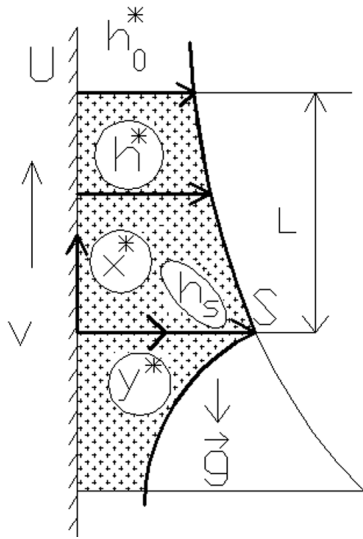


Figure 7: The dragging of fluid on a vertically moving metal surface⁸ where h_s is the thickness of the fluid layer on the stagnation line of a metal surface moving with the constant velocity of U , h_0^* is the thickness of the dragged fluid layer on the metal sheet, and v is the sheet velocity

Slika 7: Vlečenje maziva na površino s pokončnim gibanjem⁸ h_s – deblina sloja maziva na mirujoči točki metalne površine, ki se premika s stalno hitrostjo U , h_0^* – deblina sloja maziva, ki ga vleče kovinska površina, v – hitrost traka

angle α , sheet velocity v_0 , rolls velocity v_R and rolls radius R .

The Reynold's differential equations of fluid mechanics describing the representation in **Figure 8** are:

$$dp/dx = 6\mu(v_0 + v_R) / \varepsilon^2(x) - 12\mu Q / \varepsilon^3(x) \quad (4)$$

$$\tau = \mu(v_R - v_0) / \varepsilon(x) - (\varepsilon(x)/2) dp/dx \quad (5)$$

For $x = 0$ we have $\varepsilon(x) = \varepsilon_0$ in the entering section of the deformation zone. For the change of pressure gradient $dp/dx = 0$ the tangential stress in the lubricant layer (τ) is:

$$\tau = \mu(v_R - v_0) / \varepsilon(x) \quad (6)$$

In equation (6), attributed to Nady, μ is the lubricant dynamic viscosity, Q is the lubricant flow, $\varepsilon(x)$ is the lubricant layer thickness ahead of the section entering the deformation zone and dp/dx is the pressure gradient in the lubricant.

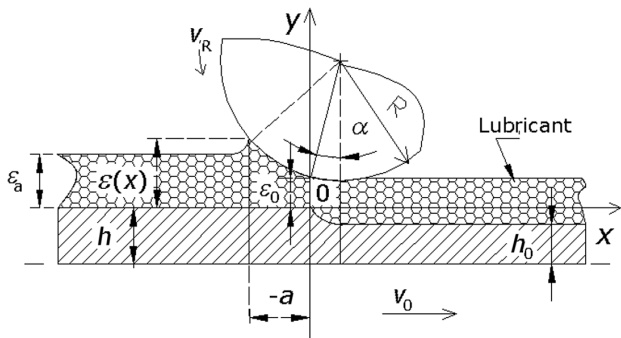


Figure 8: Cold rolling with a lubricant⁹

Slika 8: Hladno valjanje z mazanjem⁹

3 TECHNOLOGY OF THE PLASTIC WORKING OF METALS

This technology depends strongly on the quality of the technological lubricants used that:

- diminish the contact friction,
- remove the heat, cool the tool and diminish the wear,
- diminish the deformation resistance and the deformation work,
- diminish the sticking to the tool and keep the surface of the product clean.

The basic groups examined in this work are:

- liquid emulsions,
- fats and compounds,
- consistent lubricants,
- transparent – glass lubricants,
- powder lubricants,
- metallic lubricants.

The friction in cold deformation is, in principle, of the boundary type, and it is characterised with a great working pressure. The approaches in the development of the theory of friction are:

- geometrical, with the friction coefficient $\mu = \text{tg}\alpha$,
- molecular, with attraction based on a kinetical conception,
- deformation, based on the deformation work for a determined volume,
- a combination of different approaches.

The first calculations for the lubricant layer were by Mizuno¹⁰. According to Figure 8, the thickness of the lubricant layer is:

$$\varepsilon_0 = 3\mu_0\gamma(v_0 + v_R) / \alpha(1 - \exp(-p_0\gamma)) \quad (7)$$

with γ being the piezocoefficient lubricant viscosity, p_0 the rolling pressure, α the rolling angle, μ_0 the lubricant viscosity at atmospheric pressure, v_0 and v_R the working velocities of the tool and the rolling.

Also, new solutions were suggested, for example, Perlina, Grudeva and Kolmogorova for the technology of the cold drawing of metals,¹¹ according to **Figure 9**. The tube **3** moves with a velocity v_0 through the matrix **1** with the entering gap ψ ; it is covered with the lubricant **2** of thickness ε in the entrance section of the deformation zone.

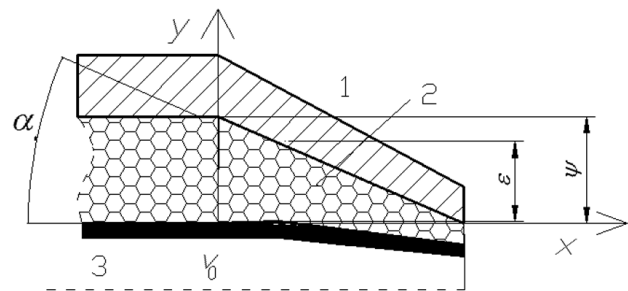


Figure 9: Cold drawing of metals with lubricant¹¹

Slika 9: Hladno vlečenje z mazanjem¹¹

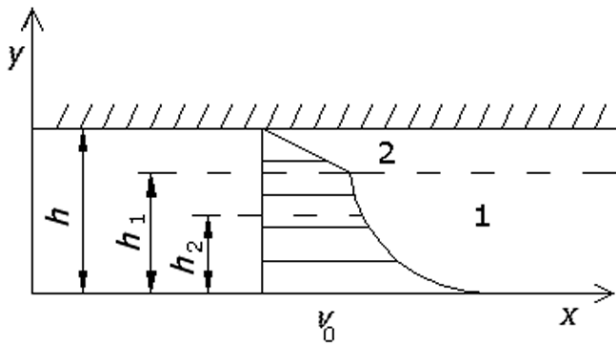


Figure 10: Distribution of velocity for the drawing of tubes with fat lubricant¹²

Slika 10: Porazdelitev hitrosti pri vlečenju cevi z masnim mazivom¹²

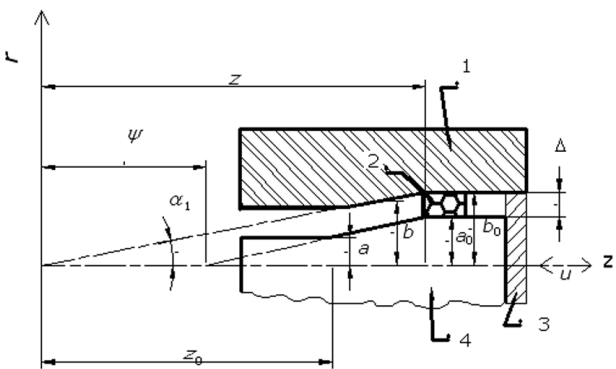


Figure 11: Pressing of metals¹³

Slika 11: Prešanje kovin¹³

The calculation is more complex for the case of combined liquid-solid lubrication. In Figure 10 the solid lubricant is the part 1 and the emulsion is the part 2. For the case in Figure 10 the maximum velocity of the emulsion is approximately 0.4 of the rolling velocity¹².

The pressing plastic deformation would be impossible without lubricant. The mathematical modelling in cylindrical coordinates is based on the scheme in Figure 11, with 1 being the round matrix, 2 the lubricant, 3 the mandrel, 4 the pressed metal and u the pressing velocity.

The forming with hydraulic fluid at the pressure 2 occurs over the membrane 1 (Figure 12). The liquid can have the role of either the matrix or of the extractor. For this process, a smaller number of toolings is used, the

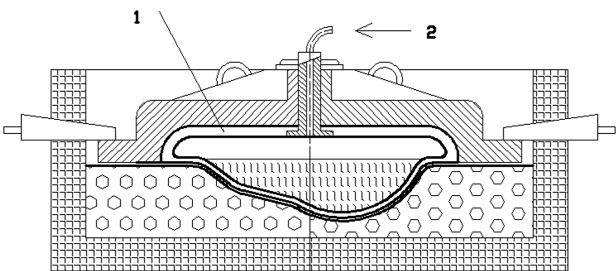


Figure 12: Hydraulic forming of a sheet

Slika 12: Hidravlično oblikovanje traka

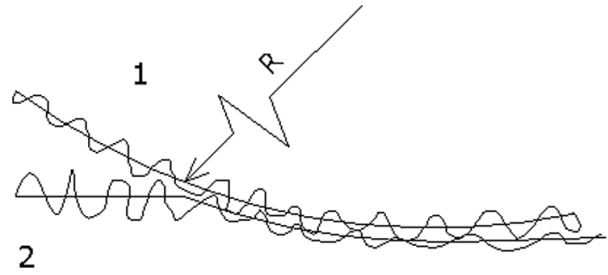


Figure 13: Uniform roughness of the rolls 1 and the sheet 2 surface¹⁴
Slika 13: Enakomerna hrpavost površine valja 1 in površine traka 2¹⁴

production costs are lower and complex forms are achieved more easily than when using conventional deep drawing.

The use of computers enabled us to also consider the surface roughness in the calculations (Figure 13) and the inertia of the lubricant with a great metal deformation velocity. In Table 1 are the differential equations for the average roughness.

The development of mathematical calculations for Pilger rolling are in the initial phase because of the complexity of the working surface of the Pilger rolls (Figure 14).

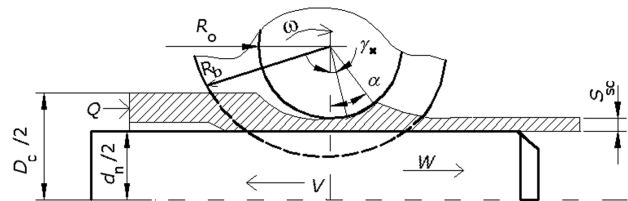


Figure 14: Scheme of Pilger rolling¹⁵, where v is the rolling direction, w is the direction of the tube D_C movement, α is the gripping angle, ω is the constant angle rotation of the Pilger rolls, γ_x is the angle of the neutral section, R_a and R_b are the radii of the rolls' calibers, $d_n/2$ is the mandrel radius, S_{SC} is the thickness of the tube wall and Q is the direction of the material flow.

Slika 14: Shema Pilgerjevega valjanja: v – smer valjanja, w – smer cevi, D_C smer gibanja, α – kot prijema, ω – constantna kotna hitrost Pilgerjevih valjev, γ_x – kot nevtralnega prereza, R_a in R_b – polmera kalibrov valjev, $d_n/2$ – polmer trna, S_{SC} – debelina stene cevi in Q – smer toka materiala

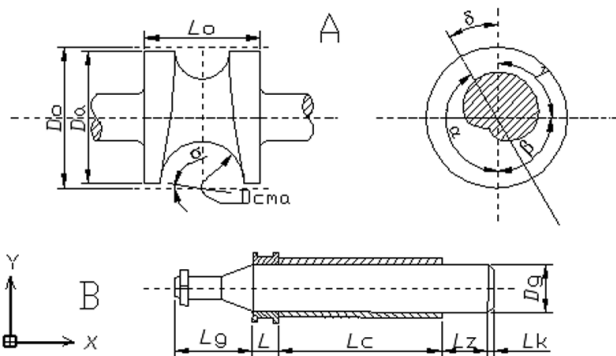


Figure 15: Elements of the Pilger stand: A is the roll, B is the mandrel¹⁶

Slika 15: Elementi Pilgerjevega ogrodja: A – valj, B – trn¹⁶

Table 1: The most frequently used differential equation of fluid mechanics applied for the description of the lubricant behaviour for different metal working processes

Tabela 1: Najbolji pogosto uporabljene enačbe in mehanike loma za opis vedenja maziva pri različnih procesih preoblikovanja kovin

Equation	Figure
<p>1. Smooth surface of the roll and of the metal worked (rolling, drawing, wire drawing)</p> $\partial p/\partial x = \mu \partial^2 v_x/\partial y^2; \partial p/\partial y = 0; \tau = \mu(v_R - v_0)/\varepsilon(x) - (\varepsilon(x)/2) dp/dx$ $\partial p/\partial z = \mu \partial^2 v_z/\partial y^2; \partial v/\partial x + \partial v/\partial y + \partial v/\partial z = 0$ <p>where v_z, v_x are the corresponding lubricant velocities, $\varepsilon(x)$ is the lubricant-layer thickness, dp/dx is the pressure gradient, τ is the tangential stress, μ is the lubricant dynamic viscosity, and v_R and v_0 are the working velocities for the tool and the material</p>	8 9
<p>2. Average roughness of the tool and of the material</p> $[dp/dx] = 6\mu(v_0 + v_R) \{ [1/\varepsilon^2(x_0)] - [1/\varepsilon_0^2] / [1/\varepsilon_0^3] \cdot [1/\varepsilon^3(x_0)] \}$ <p>$[]$ is the operator of the mathematical probability, $\varepsilon(x_0)$ is the random lubricant layer thickness, depending on the roughness of the tool and of the material, ε_0 is the lubricant-layer thickness in the access section of the zone of metal deformation</p>	14
<p>3. Sheet oiling</p> $H^3 d^3 H / C a d z^3 - (\gamma C a)^{3/2} (T/5)(H^2 - 2H_s^2/3) dH/dz + (3H - H_s - T^2 H^3) = 0$ $H_s = 3 - T^2; H = 1 + \alpha; dH/dz = -c\alpha; d^2 H/dz^2 = c^2 \alpha; \alpha = A \exp(-cz); z = x^*/h^*$ $C a = \mu U/\sigma; T = h_0^* (\rho g/\mu U)^{1/2}; \gamma = \sigma(v^4 g)^{-1/3} \rho; H = h^*/h_0^*$ <p>h_0^* is the ordinate of the free liquid surface, H is the dimensionless ordinate of the free surface, T is the dimensionless thickness h^*/h_0^* of the layer dragged on the metal surface, U is the velocity of the sheet withdrawal, z is the coordinate, v is the kinematical viscosity, and σ is the surface tension</p>	7
<p>4. Lubricant shaping on an inclined surface (inclined bending rolling)</p> $\partial p/\partial x = \mu \partial^2 u/\partial x^2 + \rho g \sin \beta - \partial \Phi/\partial x$ $\partial p/\partial y = -\rho g \cos \beta - \partial \Phi/\partial y; \partial h/\partial t + \mu \partial h/\partial x = v$ <p>Shaping of a drop on the horizontal plane (cylindrical coordinates)</p> $\partial p/\partial r = \mu \partial^2 v_x/\partial x^2$ <p>$\partial p/\partial r$ is the cylindrical coordinate system, Φ is the potential of the diffusion forces resulting from the interaction of lubricant molecules and the metal surface</p> $\Phi \approx 10^{-20} ((\text{tg} \alpha)^2 - \alpha^2)/h^3; t$ is the flowing time for a drop of lubricant; v is the velocity	6 18
<p>5. Metal pressing (extrusion), cylindrical coordinates</p> $(1/r)(\partial/\partial r(r \partial v_r/\partial r)) = (1/\mu) \partial p/\partial z$ <p>μ_t = the lubricant viscosity, depending on the temperature and pressure according to the Barussa equation.</p>	11
<p>6. Tube drawing with fat lubricant</p> $\tau_1 = -\tau_0 - dp/dx(h_2 - y);$ $\tau = \tau_0 + K \gamma_0 ^{m-1} \gamma_0$ $v = (h_2 - y)^{c+1}/(c+1) \cdot (1/K) (dp/dx)$ <p>τ_1, τ_0 are the critical tangential stresses at the boundary tool and worked piece, h is the gap height between the tool and the worked piece, γ is the worked piece velocity, K, m, c are the rheological characteristics of the fat.</p>	10
<p>7. Effect of inertia and of the smooth tool and worked piece surfaces</p> $\partial p/\partial x = 6\mu(v_0 + v_R)/\varepsilon^2(x) + C_1 \mu/\varepsilon^3(x) + \rho \text{tg} \alpha (16v_0^2 \varepsilon^2(x) - C_1^2)/120 \varepsilon^3(x)$ $C_1 = k/2 - (k^2/4 + 2v_0 \varepsilon_0 (8v_0 \varepsilon_0 + 3k))^{1/2}; k = 120v/\text{tg} \alpha$ $\varepsilon(x) = \varepsilon_0 - \alpha x + x^2/2R - \alpha x^3/2R^2 + \dots$ <p>α is the gripping or drawing angle, R is the roll's radius, v_0, v_R are the working velocities for the tool and the worked piece, and v is the kinematical viscosity</p>	8
<p>8. New approaches to the mathematical modelling (rolling of metals)</p> $dk/d(\varphi/\alpha) = 6W(\Delta h/\varepsilon_0)^2(H_{0S} - H_{HS})/H_{HS}^3 e^{Mk}; W = \mu_0(v_0 + v_R)/\sigma_T \Delta h \alpha$ $H_{HS} = \Delta h/2\varepsilon_0 [(\varphi/\alpha)^2 - 1] + H_{0S} [C_1/\Delta_1(\varphi/\alpha - (1 - \Delta_1)) + k] +$ $+ R_{za}/2\varepsilon_0 \sin[2\pi(\varphi/\alpha - (1 - \Delta_1))/C_{a0}\Delta_1 + C_{a1}] +$ $+ R_{zn}/2\varepsilon_0 \sin[2\pi(\varphi/\alpha - (1 - \Delta_1))/C_{n0}\Delta_1 + C_{n1}] -$ $- (1 + R_{za}/2\varepsilon_0 \sin C_{a1} + R_{zn}/2\varepsilon_0 \sin C_{n1})k + 1$ <p>where C_{a1}, C_{n1} are the roughness of the rolls and the sheet, C_1 is the coefficient considering the shape of the wedge-shaped lubricant gap (zone 1), Δh is the absolute reduction, φ is the local angle in the deformation zone, α is the gripping angle, μ_0 is the dynamical viscosity at air pressure, R_{zn}, R_{za} are the sheet and rolls roughness, $\Delta_1 = \sigma_T/(2\delta E_E)$, σ_T is the module of flowing, δ is the relative reduction, E_E is the module of elasticity, $k = p/\sigma_T$, p is the rolling pressure, $M = \theta \sigma_T$, θ is the piezocoefficient of viscosity, e is the base of the natural logarithm, $H_{0S} = \varepsilon_1/\varepsilon_0$, $H_{HS} = \varepsilon/\varepsilon_0$, ε_0 is the thickness of the lubricant layer at the access of the deformation zone, C_{a0}, C_{n0} are the roughness amplitudes for the rolls and the sheet, v_0 and v_R are the working velocities for the rolls and the sheet</p>	20

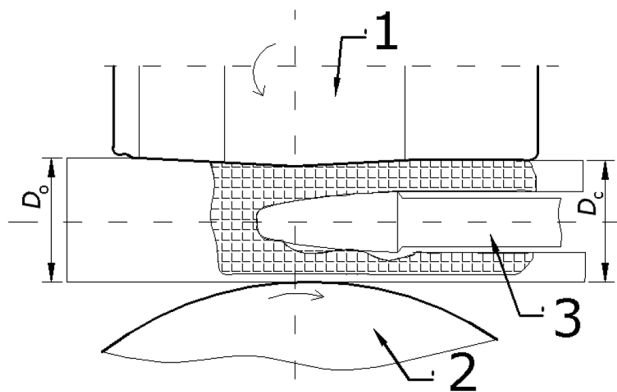


Figure 16: Scheme of the drilling of the rolling in a modern bending stand¹⁷

Slika 16: Shema prebijanja valjanca v modernem upogibnem ogrodju¹⁷

Pilger rolling is a periodic process and it is one of the most complex processes of plastics, since it deforms metals and combines the characteristics of rolling and forging with metal forming in the caliber of the changing section (Figure 15).

The Pilger rolling stand in Figure 15 has three parts inside the working caliber:

- the front part, where the basic metal deformation is achieved, α ,
- the polishing part, where the final tube size is achieved, β ,
- and the longitudinal part, where the transition from the polishing to the final barren part occurs, γ .

The methods of the plastic deformation of metal between the drawing, rolling, and pressing with already developed calculations of the behaviour of the lubricant layer and the insufficiently investigated Pilger rolling are:

- the drilling on the Diescher disc (Figure 16),
- bending (inclined) drilling (Figure 17),
- three-rolls rolling stands rolling (Figure 18).

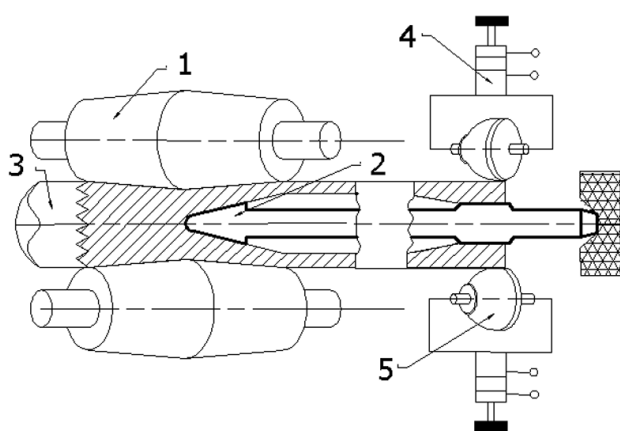


Figure 17: Scheme of the drilling stand for bending rolling with barrel-shaped rolls¹⁸

Slika 17: Shema prebijalnega ogrodja za upogibno valjanje s sodastimi valji¹⁸

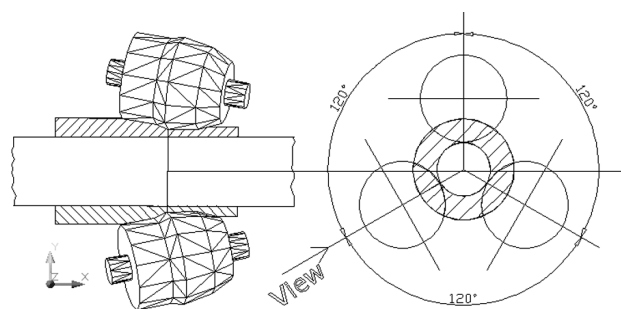


Figure 18: Scheme of the tube deformation in the three-rolls high rolling stand¹⁹

Slika 18: Shema deformacije cevi v triovaljalnem ogrodju¹⁹

The drilling mandrel (3) advances through the pierced round of diameter D_0 . Above the rolling is the working stand (1) and below it is the Diescher disc (2).

The mandrel 2 drills the rolling 3 with the rotation of the barrel-shaped rolls 1 with support from the hydraulic cylinders 4 and the barrel-shaped rolls 5.

The working rolls of the three-rolls high rolling stand are set at an angle of 120° . The gripping angle is selected in the range 0° to 10° and the rolling angle in the range 3° to 7° . Specific to the stands is the shape of the working rolls that increase the regularity of the metal

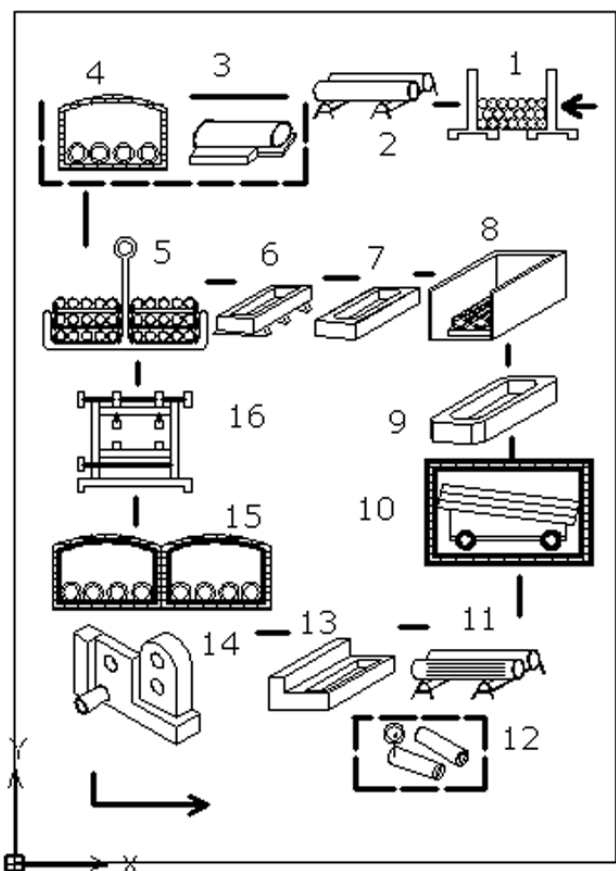


Figure 19: Technological scheme of the manufacturing of tubes with cold rolling²⁰

Slika 19: Tehnološka shema za izdelavo cevi s hladnim valjanjem²⁰

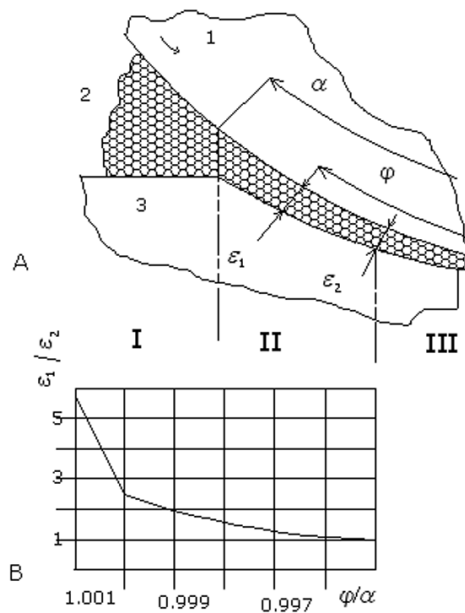


Figure 20: Mathematical modelling of the rolling with lubricant and the approach to the deformation zone²⁵
Slika 20: Matematično modeliranje valjanja z mazivom in približek za zono deformacije²⁵

flow and the tube quality. (1, the gripping cone; 2, the rolls ridge; 3, polishing cone; and 4, the release cone).

In **Figure 19** the technological scheme of the manufacturing of tubes with cold rolling is shown with: 1) billets storehouse; 2) inspection; 3) cutting of tube ends; 4) heat treatment; 5) collecting of tubes in packets; 6) decapping; 7) rinsing with hot water; 8) rinsing with cold water; 9) neutralization; 10) drying; 11) inspection; 12) repairing; 13) lubrication; 14) rolling on the cold Pilger stand; 15) intermediate heat treatment; 16) straightening.

5 DIFFERENTIAL EQUATIONS

In **Table 1** the equations describing the lubricant behaviour for different metal-working processes are given.

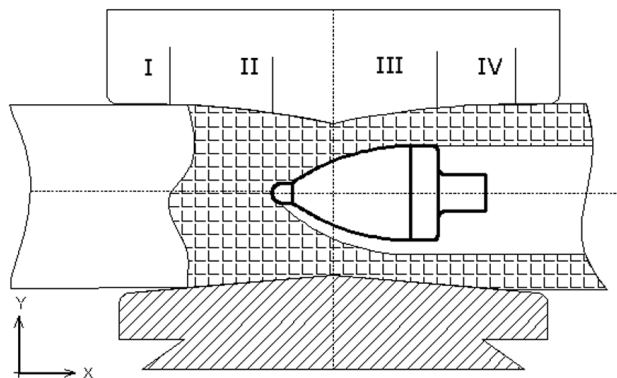


Figure 21: Deformation zone by bending rolling
Slika 21: Zona deformacije pri upogibnem valjanju

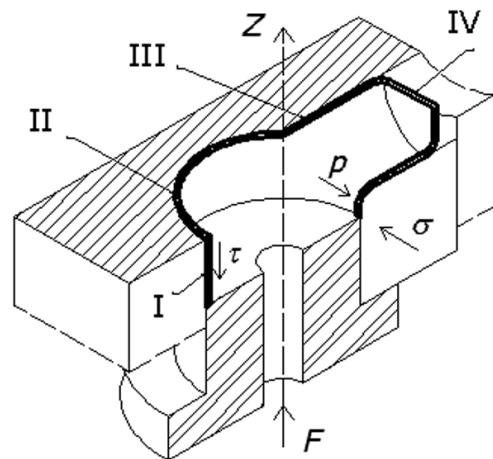


Figure 22: Forming of the T-shaped tube end (F is the axial force, p is the fluid pressure, σ and τ are the normal and tangential stresses)
Slika 22: Oblikovanje konca cevi v obliko T (F – aksialna sila, p – pritisk tekočine, σ in τ – normalne in tangencialne napetosti)

The use of lubricant in the plastic-deformation processes has increased greatly the working velocity, which required a consideration of the inertia effects in the calculations of the lubricant layer²⁶. Computer calculations made it possible to also consider the effects of roughness^{27,28}, the mathematical modelling based on the Fourier series²⁹ and the reduction in lubricant use, considering the shape of the lubricant wedge ahead of the access section of the zone of plastic deformation³⁰ (**Figure 20**).

In parallel with the investigations of the lubrication for the plastic working of metals^{31,32}, more efficient lubricants were also developed^{33,34}. It is to be expected that fluid mechanics will also be applied for a description of the lubricant behaviour in the processes of bending rolling, shown in **Figure 21**.

On the longitudinal section of the deformation zone of bending rolling the following zones are distinguished:

1. the drilling zone (from plane I to plane II),
2. the rolling on the mandrel zone (from plane II to plane III),
3. the reduction of the worked piece in the absence of the mandrel zone (from plane III to plane IV).

The application of the Reynolds' differential equation will probably start with the zone of rolling on the mandrel.

New findings of the forming of tubes with a fluid are presented in ref.³⁶ with the forming of the T-shaped end tubes shown in **Figure 22**.

- Four characteristic zones are distinguished:
- I – the zone of the main tube (flat stress-state)
 - II – the zone of the tube translating into drainage (volume stress-strain state)
 - III – the drainage zone (pressure and stretching stresses)
 - IV – the drainage peak zone (pressure and stretching stresses)

6 CONCLUSION

The use of fluid mechanics for the calculation of the behaviour of the lubricant layer in the metal deformation zone for most of the metal working processes has greatly increased with the application of computers. In the article a survey is given over the scheme of different metal-working processes and of the differential equations used for the description of the lubricant behaviour. Mostly, the derived equations are based on the Reynolds' differential equation and only some are also based on the Navier-Stokes' equation.

In modern methods of modelling of the lubricated plastic deformation of metals supplementary equations are also included to better consider the parameters of the working process. Actually, the calculations are applied mostly for the processes of the cold drawing and the rolling of metals³⁵, while for the Pilger processing they are being developed.

7 REFERENCES

- ¹ I. Mamuzić, V. M. Drujan: Teorija, Materijali, Tehnologija čeličnih cijevi, Hrvatsko Metalurško Društvo, Zagreb **1996**, str. 9
- ² V. F. Garbuz, S. A. Kaširskij, V. S. Marin: Stalj (**1998**) 1, 37
- ³ D. Čurčija: Tribološki aspekti primjene maziva u plastičnoj preradi metala, Institut za metalurgiju Sisak, **1988**, str.102, ukupno 210 stranica
- ⁴ F. Zdanski: Mehanika fluida, Univerzitet u Beogradu, Tehnološko Metalurški fakultet, Beograd **1989**, str. 195
- ⁵ J. Egert, L. Hok, G. M. Švob: Udžbenik Fizičke hemije, Naučna knjiga Beograd, **1964** str. 634
- ⁶ Ju. P. Abdulov, V. A. Kopilenko: Izvestija AN SSSR Metalli 14 (**1972**) 4, 147–150
- ⁷ A. S. Romanov: Izvestija Neft i Gaz 30 (**1987**) 7, 66
- ⁸ Z. P. Šulman, V. I. Bajkov, K. Engelgardt: Teoretičeskie osnovii himičeskoj tehnologiji 19 (**1985**) 2, 21
- ⁹ D. Čurčija, I. Mamuzić: Tehnika-RGM 34 (**1983**) 8, 1075–1078
- ¹⁰ T. Mizuno: Japon J. Soc. Techn. Plast 66 (**1966**) 7, 383–389
- ¹¹ D. Čurčija, I. Mamuzić: Mater. Tehnol. 39 (**2005**) 3, 61–76
- ¹² D. Čurčija, I. Mamuzić: Mater. Tehnol. 41 (**2007**) 1, 21–27
- ¹³ D. Čurčija: Mater. Tehnol. 37 (**2003**) 5, 237–250
- ¹⁴ V. L. Mazur, V. I. Timošenko, I. E. Varivoda: Izvestija Černaja metallurgija 50 (**1980**), 81–85
- ¹⁵ Ibid 1, p. 160
- ¹⁶ Ibid 1, p. 260
- ¹⁷ Ibid 1, p. 123
- ¹⁸ Ibid 1, p. 196
- ¹⁹ Ibid 1, p. 209
- ²⁰ Ibid 1, p. 394
- ²¹ D. Čurčija, I. Mamuzić: Proračun mazivoga sloja kod valjanja cijevi u kavezima, 40 Symposium Lubricants; Društvo za goriva i maziva, Zagreb, Pula, 23.–25.10.2007
- ²² D. Čurčija, I. Mamuzić: Lubricating film shape at band dressing, 38 Symposium Lubricants, Društvo za goriva i maziva, Zagreb, Rovinj, 19.–21.10.2005
- ²³ D. Čurčija: Modeliranje mazivoga sloja kod valjanja bešavnih cijevi, 13 International Conference MATRIB 08 /Krešimir Grilec urednik/, Hrvatsko društvo za materijale i tribologiju Zagreb, **2008**, Vela Luka, 35–50
- ²⁴ D. Čurčija, I. Mamuzić: Materiali in Tehnologije 42 (**2008**) 2, 59–65
- ²⁵ I. Mamuzić, D. Čurčija, F. Vodopivec: Lubricant for Rolling and Drawing of Metals; Metalurgija 45 (**2006**) 3, 196 (Summarie)
- ²⁶ O. P. Maksimenko, O. E. Lejko: Sučasni problemi metalurgii, 8 (**2005**) 93–99
- ²⁷ D. Čurčija, I. Mamuzić, Metalurgija 44 (**2005**) 2, 113–117
- ²⁸ D. Čurčija: Strojstvo, 30 (1988) 3–4,191–197.
- ²⁹ D. Čurčija, I. Mamuzić: Metalurgija 44 (**2005**) 4, 295–300
- ³⁰ D. Čurčija, I. Mamuzić: Metalurgija 44 (**2005**) 3, 221–226
- ³¹ D. Čurčija, I. Mamuzić: Goriva i maziva 46 (**2007**) 1, 23–44
- ³² D. C. Zacccone, J. J. Bodnar, R. G. Elko, J. M. Grivna: J. Mater. Manuf., 107 (**1988**), 26–34
- ³³ M. M. Me, S. P. Liu, J. F. Zheng: Met. Form. Technol. 20 (**2002**) 5, 29–32
- ³⁴ S. A. Kuznetsov, S. Y. Semenov, A. I. Vinogradov, E. A. Graber: Proizvod. Prokatka (**1999**) 7, 26–28
- ³⁵ Y. T. Keun, B. H. Lee, R. H. Wagner: J. Mater. Process. Technol. 130 (**2002**), 60–63
- ³⁶ S. V. Mazur: Sučasni problemi metalurgii 8 (**2005**) 447–452
- ³⁷ M. Jurković, I. Mamuzić, E. Karabegović: Metalurgija 43 (**2004**) 4, 315–322

THE BRITTLE TENSILE FRACTURE AND CLEAVAGE STRENGTH OF A STRUCTURAL STEEL WITH A SIMULATED WELD-AFFECTED-ZONE MICROSTRUCTURE

TRDNOST PRI KRHKEM PRELOMU IN CEPILNA TRDNOST ZA KONSTRUKCIJSKO JEKLO S SIMULIRANO MIKROSTRUKTURO TOPLOTNE CONE ZVARA

Gorazd Kosec¹, Boris Arzenšek², Jelena Vojvodič Tuma², Franc Vodopivec²

¹SIJ, d. d., Acroni, d. o. o., Kidričeva 44, 4270 Jesenice, Slovenia

²Institute of Metals and Technology, Lepi pot 11, 1000 Ljubljana, Slovenia
gorazd.kosec@acroni.si

Prejem rokopisa – received: 2008-11-13; sprejem za objavo – accepted for publication: 2008-12-23

Tensile tests were carried out on specimens of the same micro-alloyed structural steel after different thermal treatments, with the aim being to obtain the microstructure in a weld's heat-affected zone. The mechanical properties were determined at a temperature below the brittle threshold transition Charpy temperature, the fracture surfaces were examined, the cleavage strength was deduced and the space orientation of the cleavage facets was determined. No relation was found between the results of the tensile tests and the previously determined Charpy properties after an identical thermal treatment.

Key words: micro-alloyed structural steel, cleavage strength, fracture surface morphology, cleavage facet orientation

Opravili smo raztržne preizkuse mikrolegiranega konstrukcijskega jekla, ki je bilo toplotno obdelano za dosego nekaterih mikrostruktur v toplotni zoni zvara. Določili smo mehanske lastnosti pri temperaturi pod pragom krhkega Charpyjevega preloma, pregledali prelomne površine, izračunali cepilno trdnost in določili prostorsko orientacijo cepilnih ploskev. Našli nismo nobene povezave med rezultati te raziskave in značilnostmi Charpyjevega preloma jekla po enaki toplotni obdelavi.

Ključne besede: mikrolegirano konstrukcijsko jeklo, cepilna trdnost, značilnosti krhkega preloma, prostorska orientacija cepilnih ploskev

1 INTRODUCTION

With the aim being to explain the difference in the Charpy toughness transition temperatures of the welds in steel plates of different thicknesses from the same structural steel with a yield stress of 490 MPa, the transition temperature was determined for ten types of microstructure: the initial microstructure of fine-grained tempered martensite, the coarse- and fine-grained primary martensite and bainite, the coarse- and fine-grained primary bainite and these basic microstructures with the secondary martensite obtained by reheating the specimens in the two-phase region – ferrite+ austenite – and air cooling¹. We found that after reheating the transition temperature was increased and the upper-shelf toughness decreased the most for the microstructure of bainite, especially for coarse-grained bainite¹. These experimental findings confirmed the assumption that the coarse bainite microstructure was the most likely to form LBZs (local brittle zones) in the heat-affected zone of the welds^{1,2}.

In this article we present and discuss the results of an investigation aimed to determine whether the transition temperature was related to the brittle tensile strength and

the cleavage strength of different microstructures, as quenched and after a reheat.

2 EXPERIMENTAL WORK

A fine-grained steel (0.11 C, 0.5 Mn, 0.54 Cr, 0.34 Mo, 0.014 Ti and 0.032 Nb) with an initial microstructure of tempered martensite and ferrite and a linear intercept length of 3 μm was investigated. The specimens were quenched at 920 °C and 1250 °C in water at 70 °C or in a lead bath at 400 °C. To simulate the heat cycle during the deposition of the next welding pass, half of the specimens were submitted to reheating for 3 s at 750 °C and air cooling. All the tensile tests were performed on two parallel specimens with a circumferential notch with a shape and size the same as that used in the laboratory for determining the fracture toughness of tool steels with a low notch toughness³, and similar to those used for investigations of the cleavage strength of structural steels^{4,5,6}. The diameter of the cylindrical part of the specimen was 10 mm, with a diameter of 8 mm in the notch. The cross-head speed was 5 mm min⁻¹ and the testing temperature was –120 °C, some 30 °C or more lower than the lower-shelf notch toughness threshold temperature⁷. Notched specimens

were used because for flat tensile specimens at approximately $-130\text{ }^{\circ}\text{C}$, some $30\text{ }^{\circ}\text{C}$ lower than the nil ductility temperature, the steel exhibited ductile fracturing with a 65 % reduction of the area. However, with notched specimens the brittle fracturing was obtained already at $-115\text{ }^{\circ}\text{C}$ ⁸.

From the obtained dependences it was possible to determine the range of elastic and plastic deformation of the specimen before fracture, the elastic stress at the onset of plastic deformation and the fracture stress. The fractured surfaces were examined visually and on an SEM, and special care was given to the fracture micro-morphology along the notch tip, to the transition area and to the boundary area between the ductile ring and the brittle central area. The orientation of the brittle

facets was determined for some specimens with EBSD (electron back-scatter diffraction).

3 BRITTLE TENSILE STRENGTH AND EXTENT OF PLASTIC DEFORMATION

In **Figures 1 to 4** the characteristic recorded dependences of the tensile force versus the deformation are given: a case with the fracture virtually in the range of proportionality force-deformation in **Figure 1** (type A), two cases with an increasing extent of plastic deformation in **Figures 2 and 3** (type B) and a case with a clear yielding in **Figure 4** (type C). In **Table 1** the extent of the plastic deformation before the fracture (*PD*), the brittle tensile strength (*BFS*), the deduced value of the cleavage strength, the Vickers hardness, the width of the ring of plastic shearing at the notch tip as,

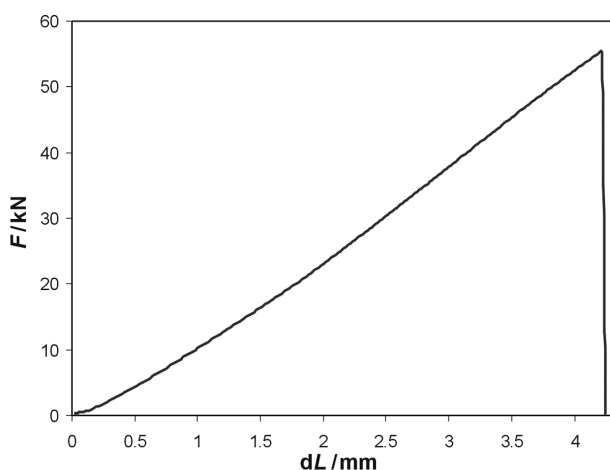


Figure 1: Dependence of force vs. extension for a specimen quenched from $1250\text{ }^{\circ}\text{C}$ and reheated at $750\text{ }^{\circ}\text{C}$. Microstructure: coarse-grained tempered primary martensite and secondary martensite.

Slika 1: Odvisnost sila-podaljšek za preizkušane, kaljen v vodi s $1250\text{ }^{\circ}\text{C}$ in segreti pri $750\text{ }^{\circ}\text{C}$. Mikrostruktura: popuščeni grobozrnati primarni martenzit in sekundarni martenzit

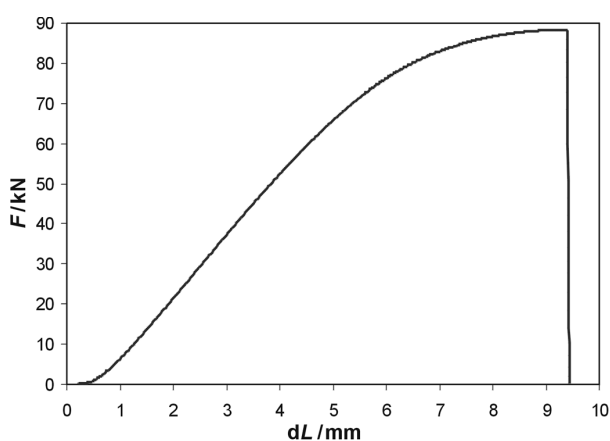


Figure 3: Dependence of force vs. extension for a specimen quenched in water from $920\text{ }^{\circ}\text{C}$ (a). Microstructure: fine-grained martensite

Slika 3: Odvisnost sila-podaljšek za preizkušane, kaljen v vodi s $1250\text{ }^{\circ}\text{C}$. Mikrostruktura: drobno zrnati martenzit

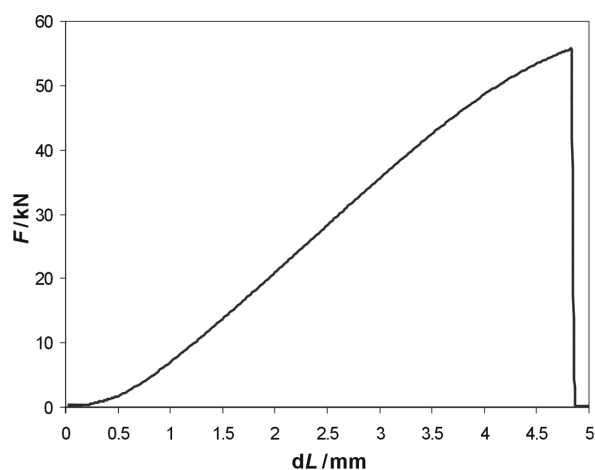


Figure 2: Dependence of force vs. extension for the specimen quenched from $1250\text{ }^{\circ}\text{C}$ in a lead bath at $400\text{ }^{\circ}\text{C}$ and reheated at $750\text{ }^{\circ}\text{C}$. Microstructure: coarse-grained bainite and secondary martensite

Slika 2: Odvisnost sila-podaljšek za preizkušane, ohlajen v svincu s $1250\text{ }^{\circ}\text{C}$ in segreti pri $750\text{ }^{\circ}\text{C}$. Mikrostruktura: grobozrnati bainit in sekundarni martenzit

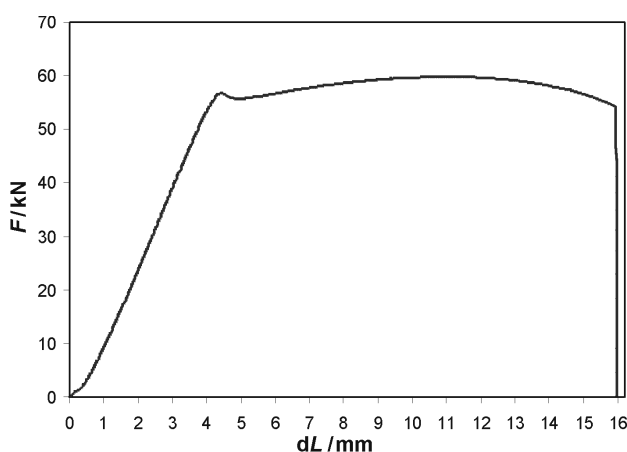


Figure 4: Dependence of force vs. extensions for a specimen with the initial microstructure reheated at $750\text{ }^{\circ}\text{C}$. Microstructure: fine-grained tempered martensite–ferrite and secondary martensite

Slika 4: Odvisnost sila-podaljšek za preizkušane z začetno mikrostrukturo, segreti pri $750\text{ }^{\circ}\text{C}$. Mikrostruktura: popuščena fino zrnati martenzit in ferit ter sekundarni martenzit

the Charpy fracturing energy at 0 °C (CV0) and the lower-shelf Charpy temperature-temperature of cleavage fracture (CVC) are given. In the discussion the characteristics of the specimen with the initial microstructure are used for the comparison.

The steel with the initial microstructure of tempered martensite shows the dependence force versus the extension (tensile curve) of the C type, a significant plastic extension and a reduction of the area of 8.1 %. After reheating at 750 °C, the hardness and the brittle tensile strength (*BFS*) are higher, the tensile curve is of the C type with clear yielding and the plastic extension is increased to 2.41 mm, while the reduction of the area is lowered to 3.7 %. The differences between both specimens are attributed to the presence of secondary martensite in the microstructure of the specimen reheated at 750 °C.

After water quenching from 920 °C the tensile curve is of the B type; the hardness and especially the *BFS* are greater than for the steel with the initial microstructure. As would be expected for the microstructure of quenched fine-grained martensite, the plastic extension is similar to that for the initial microstructure and the reduction of the area below the detection limit. After reheating, the type of the tensile curve is not changed; however, all the characteristics are lowered and indicate that the effect of tempering of the primary martensite exceeded the effect of the presence of secondary martensite. After water quenching from 1250 °C, the tensile curve is of the A type, the hardness is strongly increased, the *BFS* slightly, the plastic extension is at the detection limit and much lower than after quenching from 920 °C. After reheating, the type of tensile curve is not changed, the hardness is significantly lower, the *BFS* is slightly changed and the plastic extension is very low.

After cooling in a lead bath from 920 °C, the tensile curve is of the B type, the hardness is slightly higher, the *BFS* significantly increased and the plastic extension was virtually equal to that for the initial microstructure. After reheating the tensile curve is unchanged, the hardness is changed little and the *BFS* and the plastic extension are lower. After lead cooling from 1250 °C the tensile curve is of the B type, the hardness is unchanged, the *BFS* is slightly increased and the plastic extension slightly decreased. After reheating, the tensile curve is unchanged, the hardness is significantly higher, the *BFS* slightly lower and the plastic extension much lower.

The change of hardness reflects the characteristics of the microstructure and its changes after reheating. The hardness is increased more after water quenching and especially after quenching from 1250 °C. After reheating, the hardness is slightly higher for the specimens with the initial and bainite microstructures, while it is lower for the martensite microstructure. It is concluded that the softening effect of the tempering of primary martensite exceeds the effect of the presence of secondary martensite.

The brittle fracture strength (*BFS*) was very different for the different microstructures and in all cases, with the exception of the as-delivered microstructure, it was slightly lower after reheating. Somewhat surprisingly, after quenching from 1250 °C the hardness is increased more than the *BFS*, while after reheating the hardness is decreased and the *BFS* virtually unaffected.

These findings indicate that the reheating affects differently the Charpy properties, not only the transition temperature of the ductile-to-brittle fracture¹, but also the hardness of the martensite and bainite and *BTS* and also show that the hardness is not related to the *BTS*. In comparison to the initial microstructure, the plastic extension is lower for all the other specimens, and it is especially low for the martensite obtained with water quenching from 1250 °C. After reheating it is higher for the initial microstructure and lower for all the other tested microstructures. These findings indicate that the hardness of the different microstructures in the weld-affected zone cannot be used as a reliable measure of the other properties of these microstructures.

4 CLEAVAGE STRENGTH

The cleavage strength (E_{cl}) depends on the brittle fracture strength (*BFS*) and on the specimen's geometrical shape. It is deduced from the nominal fracture stress (E_n) considering the specimen (r_{ns}) and the notch radius (r_n)^{8,9}:

$$E_{cl}/E_n = 1 + \ln(1 + r_{ns}/r_n) \quad (1)$$

For notched specimens the real stress at the notch tip depends on the stress-concentration factor¹⁰ K_p :

$$K_p = 1 + \ln(1 + R/r_c) \quad (2)$$

With R being the radius (extension of the plastic zone ahead of the crack notch) tip and r_c being the crack-tip radius. With instrumented Charpy tests the stress-concentration factor was, in the temperature range 60 °C to -20 °C, 3.22 to 3.35 for a 0.17 % C – 1.28 % Mn steel and 2.42 to 2.62 for the steel investigated¹¹. This factor was termed as a ratio of the yield stress obtained with the Charpy instrumented tests and the yield stress of the tensile cylindrical specimens. Using the average value for the stress-concentration factor of 2.52 and the steel yield stress of 490 MPa a stress concentration of 1234 MPa is deduced. On notched specimens the brittle tensile strength of 1250 MPa was found for the investigated steel at¹². Experimental findings show that the stress-concentration factor also depends on the properties of the steel that probably determine the acuity of the propagating crack tip. The crack tip radius is calculated as¹²:

$$r_c = 0.32 (E/E_{cl})\delta \quad (3)$$

or for a sharp crack:

$$r_c = (1/6\pi) (K_{IC}/E_{cl})^2 \quad (4)$$

Table 1: Characteristics of the tensile and Charpy notch tests and of the tensile fracture surfaces**Tabela 1:** Značilnosti raztržnega preizkusa, Charpyjevih preizkusov in raztržnih prelomov

Specimen	Hardness <i>HV</i> 5	<i>BFS</i> MPa	<i>CS</i> MPa	<i>PE</i> mm	<i>WDS</i> mm	<i>CT0</i> J	<i>CTT</i> °C
Initial	205	1063	1934	1.33	0.41	240	-100
" + 750 °C	249	1231	2240	2.41	0.37	95	-80
920 °C wat.	282	1449	2637	1.35	0.13	120	-100
" + 750 °C	244	1329	2402	0.65	0.07	50	-50
1250 °C wat.	383	1257	2287	0.23	0.07	45	-40
..." + 750 °C	320	1230	2238	0.11	0.06	20	-40
920 lead	222	1208	2198	0.97	0.09	250	-100
" + 750 °C	241	1106	2012	0.59	0.07	27	-20
1250 lead	204	1255	2284	0.82	0.11	205	-80
" + 750 °C	248	1052	1914	0.35	0.08	14	0

BFS – brittle fracture strength

CS – cleavage strength

PE – plastic extension

WDS – width of the ring of ductile shearing

CT0 – Charpy notch toughness at 0 °C

CTT – Cleavage threshold temperature

with E equal to the elastic modulus, δ being the crack-opening displacement and K_{IC} the fracture toughness.

In the transition zone of the ductile-to-brittle fracture of the fracture surface of the notched specimens fractured below the lower-shelf notch toughness threshold a layer of smaller dimples was observed that passed over to the cleavage area with an area of plane shearing¹². In this investigation it was found that the cleavage crack extension did not start at the notch tip, but from an initial shearing crack started at the notch. This observation is in agreement with the finding¹³ that the plastic yielding is a necessary precursor to the cleavage and that maybe slip or twinning is involved in the nucleation of a cleavage fracture. In this investigation a shearing ring was found on all the tensile fractures at the notch tip. Accordingly, it is assumed that the thickness of the plastic deformation layer ahead of the de-cohesion tip decreases gradually until a critical value of the notch tip radius (r_c) is obtained, and that at this point the cleavage de-cohesion is initiated. For the value of the critical crack tip a radius of $6.2 \cdot 10^{-8}$ m was calculated⁸ using the modified equation (5)

$$r_c = (1/6\pi) (K_{IC}/E_{cl})^2 (d_c/d)^3 \quad (5)$$

Where d_c is the critical size of the dimples ahead of the ductile shearing layer and d is the dimples' size for ductile crack propagation.

It is necessary to stress that in our tests a significant plastic deformation occurred without clear yielding and the effect of the grain size on the cleavage strength was confirmed only for the martensite microstructure^{14,15}.

In this investigation the specimen and the notch tip radius were 5 mm and 0.2 mm. Applying equation (1) the cleavage strength of $E_{cl} = 1.82 E_n$ is deduced.

The cleavage strength in **Table 1** was deduced for every specimen considering the accurate diameter of the cylindrical specimen and the diameter of the fracture surface. In comparison with the initial microstructure, the cleavage strength is higher after reheating and for all the as-quenched microstructures, particularly for the martensite obtained with quenching from 920 °C. In all cases, except for the initial microstructure, the cleavage strength is lower after reheating. The explanation could be the internal stresses generated by the formation of secondary martensite. The cleavage strength is lower for both bainitic microstructures.

No indication was found for an eventual effect of plastic straining on the cleavage strength. Little of the energy is spent for the cleavage propagation, mostly for the displacement of the crack tip in the cleavage plane of the new grain with a different space orientation and less for the overcoming of the dislocations that generates river patterns on the cleavage surface. Thus, it is assumed that the presence of a greater number of dislocations generated by the plastic extension, that is different for different microstructures, did not significantly affect the value of the cleavage strength.

5 FRACTURE MORPHOLOGY AND ORIENTATION OF THE CLEAVAGE FACETS

The fracture surface of all the specimens consisted of a ring of shearing at the notch tip of different widths and a central area of cleavage (**Figure 5**). On all specimens two or even three crack initials were found in the notch tip (**Figure 6**) that joined rapidly in a ring of plane shearing. On this surface an increasing number of dimples were found at greater distances from the notch tip. At the boundary of the shearing ring, the fracture changed sharply to cleavage with facets, the size of



Figure 5: Fracture surface of a notched tensile specimen of steel quenched in water from 1250 °C. Microstructure: coarse-grained martensite

Slika 5: Prelomna površina razteznega preizkušanca, kaljenega v vodi s 1250 °C. Mikrostruktura: grobozrnati martenzit

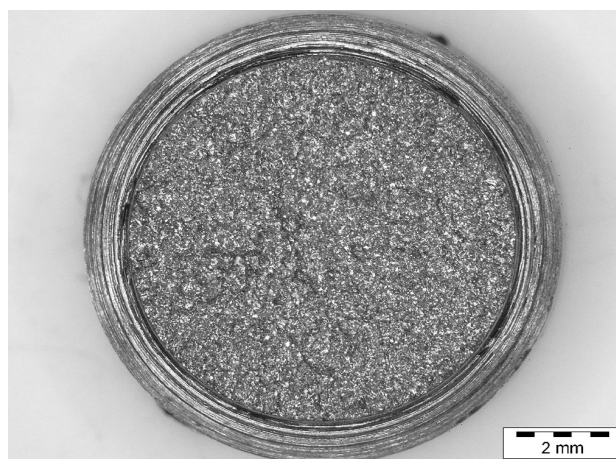


Figure 7: Fracture surface of a notched tensile specimen cooled in a lead bath from 1250 °C. Microstructure: coarse-grained bainite

Slika 7: Prelomna površina razteznega preizkušanca, ki je bil ohlajen v svincu s 1250 °C. Mikrostruktura: grobozrnati bainit



Figure 6: Fracture surface of a notched tensile specimen quenched in water from 920 °C and reheated at 750 °C. Microstructure: tempered primary fine grained martensite and secondary martensite

Slika 6: Prelomna površina razteznega preizkušanca, ki je bil kaljen v vodi s 920 °C in segret pri 750 °C. Mikrostruktura: popuščeni finozrnati primarni martenzit in sekundarni martenzit

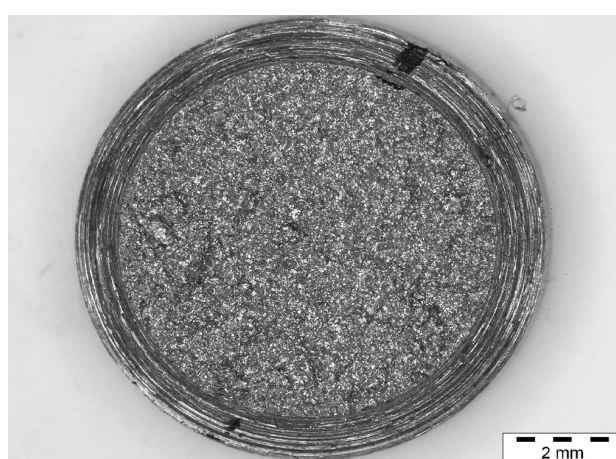


Figure 8: Cleavage surface of the steel cooled in lead bath from 920 °C. Microstructure: fine-grained bainite only

Slika 8: Cepilna površina jekla, ki je bilo ohlajeno v svincu s 920 °C. Mikrostruktura: drobnozrnati bainit

which depended on the austenite grain size before the quenching (**Figures 7 and 8**). No difference in the cleavage morphology is found that could be attributed to the presence of secondary martensite after reheating at 750 °C.

The width of the ring at the notch tip was different for different specimens. It was much greater for the steel with an initial and reheated microstructure that had a tensile curve of the type C with clear yielding and a greater plastic extension. For all the other specimens it was much smaller and even smaller after reheating. It is assumed that the ring consists partly of the layer of metal deformed at the cutting of the notch and partly of the shearing extension when the crack tip decreased to the size required for the change of propagation from shearing to cleavage. The different width also suggests

that the critical crack tip radius is not equal for all the investigated microstructures. Since the plastic extension and the shearing width ring are smaller for the as-reheated microstructures, with the exception of the initial microstructure, it is concluded that the internal stresses generated by the formation of a secondary martensite also affect the stress-concentration factor K_s and the critical crack tip radius given in equations (2), (3), (4) and (5).

The cleavage facets on the brittle fracture of a structural steel could have the space orientations (011) and (001)¹⁶. On some fracture surfaces an EBS diffraction was carried out to determine if the cleavage facets' spatial orientation was different for the different microstructures. To obtain a clear diffraction pattern, the angle between the specimen surface of the electron-collecting window must be approximately 70°. It was

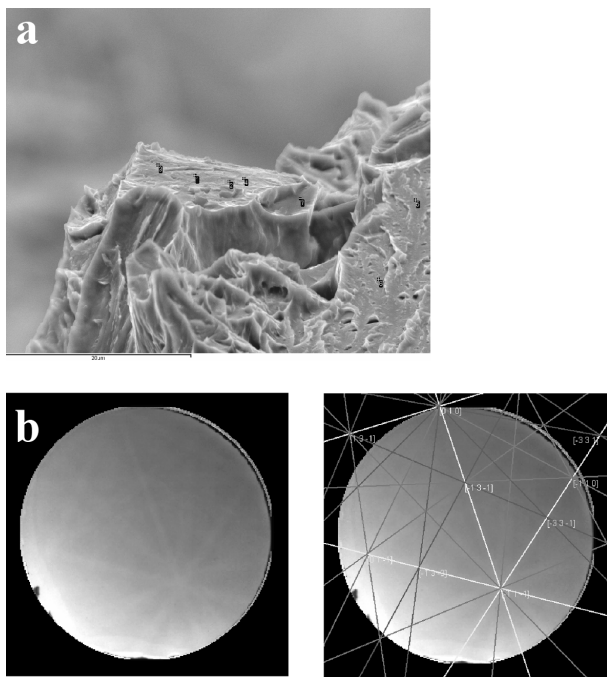


Figure 9: Specimen quenched in water from 1250 °C. Microstructure: coarse-grained martensite. Microfractography, diffraction lines, resolved diffraction lines and space-orientation indexes for the marked cleavage facet

Slika 9: Preizkušanec, kaljen v vodi s 1250 °C. Mikrostruktura: grobozrnati martenzit. Mikrofraktografija, difrakcijske črte, razločene difrakcijske črte in indeksi prostorske lege za označeno cepilno ploskev

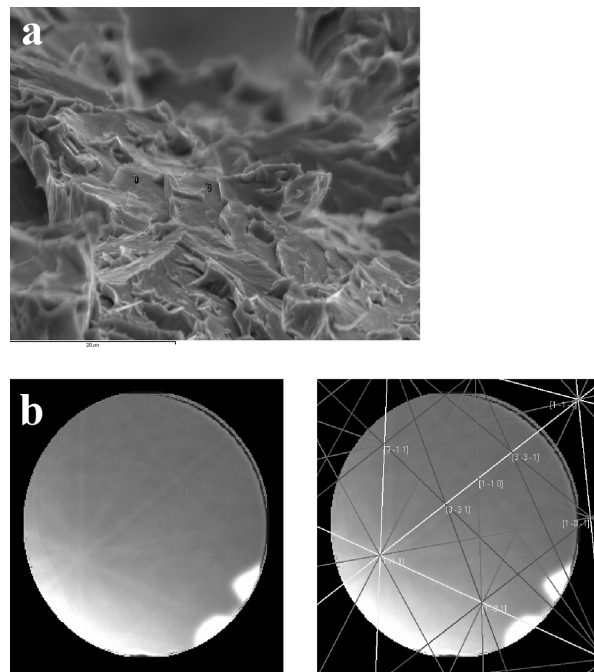


Figure 11: Specimen from fig. 9 reheated at 750 °C. Microfractography, diffraction lines, resolved diffraction lines and space-orientation indexes for the marked cleavage facet

Slika 11: Preizkušanec, kaljen v vodi s 1250 °C in segret pri 750 °C. Mikrostruktura: popuščeni grobozrnati martenzit in sekundarni martenzit. Mikrofraktografija, difrakcijske črte, razločene difrakcijske črte in indeksi prostorske lege za označeno cepilno ploskev

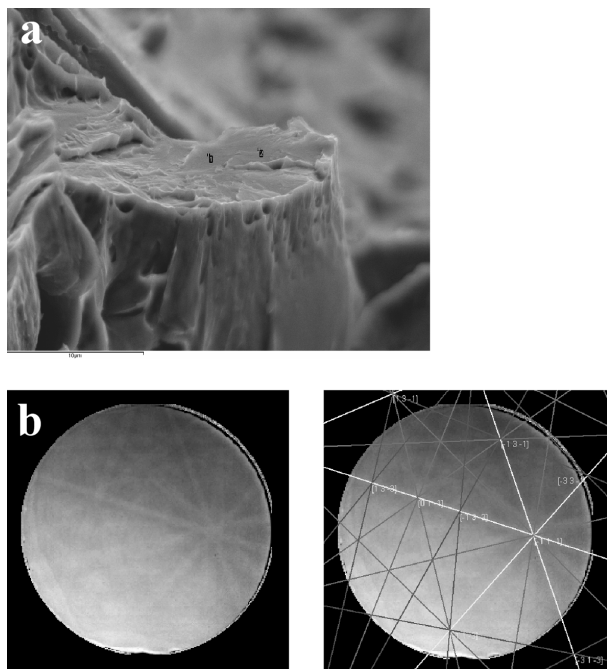


Figure 10: Specimen cooled in lead bath from 1250 °C. Microstructure: coarse-grained bainite. Microfractography, diffraction lines, resolved diffraction lines and space-orientation indexes for the marked cleavage facet

Slika 10: Preizkušanec, ohlajen v svincu 1250 °C. Mikrostruktura: grobozrnati bainit. Mikrofraktografija, difrakcijske črte, razločene difrakcijske črte in indeksi prostorske lege za označeno cepilno ploskev

virtually impossible to obtain the required position of the cleavage facets on the rugged brittle fracture surface. For this reason, the diffraction did not produce the theoretical low orientation indexes characteristic for the spatial orientations (001) and (011), but high indexes with a marked difference in intensity approaching the (001) plane. In **Figures 9 and 10** the obtained diffraction lines and the computer identification of diffraction lines are shown for the fracture of martensite and bainite obtained with water and lead cooling from 1250 °C¹. The indexes of the cleavage facets approach in all cases the (010) plane, while the vertical axis approaches the direction of (012). A virtually identical space orientation was obtained for cleavage facets on specimens which were reheated at 750 °C and air cooled (**Figure 11**). It is concluded that the microstructure does not affect the space orientation of the cleavage facets.

6 RELATION OF THE LEAVAGE STRENGTH AND THE CHARPY TOUGHNESS CHARACTERISTICS

In **Table 1** the date of the Charpy tests are given,¹ selected as characteristics for the comparison of the Charpy behaviour of the tested microstructure and their tensile characteristics as well as the cleavage strength. The experimental findings do not show a clear connection between the characteristics of both kinds of

testing. Also, these data do not indicate a relation between the brittle threshold temperature and the cleavage strength for the tested microstructures, although the assumption that the brittle fracture should occur at a higher temperature and with a lower cleavage strength seems to be logical. It is assumed that the eventual connection is probably masked by the effect of the diversity in the loading mode and the difference in the test rate of the Charpy notch toughness flexion test and the tensile test of the notched axial specimen at a much smaller deformation rate.

7 CONCLUDING REMARKS

The tensile tests of notched specimens of the same steel with an initial microstructure and a microstructure of quenched fine- and coarse-grained martensite and bainite and with the microstructure obtained with a short annealing in the two-phase – austenite + ferrite – region show that the brittle fracture, cleavage strength and the plastic extension before the fracture are not related to the hardness. Also, no connection was established between the tensile characteristics and the temperature of the cleavage fracture with the Charpy notch toughness tests.

The fracture of all but two specimens occurred after plastic deformation. While the yielding was found only for the specimens with the initial and reheated microstructures. The fracture surface of all the specimens consisted of a narrow ring of plastic shearing ahead of the notch tip and a central cleavage area.

The plane of the cleavage facets was (001) and this was independent of the microstructure and the plastic deformation before the fracture. The shearing ring was found on all the fractures, as well as on specimens fractured with a very low plastic deformation, and its width was greater with a greater plastic deformation. On all the specimens at least two shearing initials were formed at the notch tip that joined after a different extension, which may be related to the distance

necessary for the crack tip radius to decrease to a critical value characteristic for the microstructure.

The general conclusion is that all the relations between the tensile and Charpy characteristics for the same type of steel microstructure are masked by the difference in the specimen geometry and the test rate between the Charpy flexion test that occurs in 0.01 s^{-1} and the tensile test with a several orders of magnitude smaller rate.

The authors are indebted to the Ministry of Science and High Education of Slovenia for funding the project.

8 REFERENCES

- ¹ G. Kosec, F. Vodopivec A. Smolej, J. Vojvodič Tuma. Steel Research, submitted for printing
- ² F. Vodopivec, G. Kosec, S. Grbič, D. Kmetič: Mater. Tehnol. 38 (2004), 149
- ³ B. Ule, V. Leskovšek, B. Tuma: Eng. Fracture Mechanics 65 (2000), 559–572
- ⁴ C. Betegon, F. J. Belzunce, C. Rodriguez: Acta Materialia 33 (1996), 1055–1061
- ⁵ S. R. Bordet, A. D. Karstensen, D. M. Knowles, C. S. Wisner: Engineering Fracture Mechanics 72 (2005), 453–473
- ⁶ C. J. Esser, F. Grimpe, W. Dahl: Steel Research 66 (1995), 259–263
- ⁷ J. Vojvodič Tuma: Journal of Materials Processing Technology 121 (2002), 323–331
- ⁸ F. Vodopivec, B. Breskvar, B. Arzenšek, D. Kmetič, J. Vojvodič Tuma: Mat. Sci. Techn. 18 (2002), 61–67
- ⁹ P. W. Bridgeman: Studies in Large Plastic Flow and Fracture; McGraw-Hill New York, 1952, p. 9. Loc cit. Ref. 12
- ¹⁰ H. Kurishita, H. Nayano, M. Narui, M. Yamazaki, Y. Kano, I. Shibahara: Mater. Trans. JIM, 34 (1993), 1042–1052
- ¹¹ F. Vodopivec, B. Arzenšek, D. Kmetič, J. Vojvodič Tuma: Mater. Tehnol. 37 (2003), 317–326
- ¹² J. F. Knott: Met. Sci. 14 (1980), 327–336
- ¹³ D. A. Curry: Met. Sci. 14 (1980), 319–326
- ¹⁴ R. Sandström, Y. Bergson Met. Sci. 18 (1984), 177–186
- ¹⁵ D. A. Curry, J. F. Knott: Met. Sci. 10 (1976), 1–6
- ¹⁶ S. T. Mandziej: Metall. Trans. A 24A (1993), 545–552
- ¹⁷ F. Vodopivec, L. Kosec B. Breskvar: Metalurgija 39 (2003), 139–140

THE ELECTROCHEMICAL STUDY OF DUPLEX STAINLESS STEEL IN CHLORIDE SOLUTIONS

ELEKTROKEMIJSKE RAZISKAVE DUPEKSNEGA NERJAVNEGA JEKLA V KLORIDNIH RAZTOPINAH

Aleksandra Kocijan, Črtomir Donik, Monika Jenko

Institute of Metals and Technology, Lepi pot 11, 1000 Ljubljana, Slovenia
aleksandra.kocijan@imt.si

Prejem rokopisa – received: 2008-12-01; sprejem za objavo – accepted for publication: 2008-12-12

The evolution of the passive film formed on duplex stainless steel 2205 in a chloride solution was studied using cyclic voltammetry and potentiodynamic measurements. The anodic peaks in cyclic voltammograms at -0.6 V, 0 V and 1.1 V were identified with the formation of $\text{Fe}(\text{OH})_2$, FeOOH and the transpassive oxidation of $\text{Cr}(\text{III})$ to $\text{Cr}(\text{VI})$ and $\text{Ni}(\text{II})$ to $\text{Ni}(\text{IV})$, respectively. The reduction peaks at 0.3 V, -0.6 V and -0.8 V are attributed to valence transitions in solid state associated with the chromium and iron in the oxide, respectively. None of the current peaks detected in the voltammetric curves can be attributed to the Mo species alone.

Keywords: duplex stainless steel, potentiostatic, cyclic voltammetry, passive films

Raziskovali smo tvorbo pasivne plasti na površini dupleksnega nerjavnega jekla 2205 v kloridnih raztopinah s ciklično voltmetrijo in potenciodinamsko polarizacijo. Anodne vrhove v cikličnih voltamogramih pri potencialih $-0,6$ V, 0 V in $1,1$ V pripisujemo tvorbi $\text{Fe}(\text{OH})_2$, FeOOH in transpasivni oksidaciji $\text{Cr}(\text{III})$ v $\text{Cr}(\text{VI})$ in $\text{Ni}(\text{II})$ v $\text{Ni}(\text{IV})$. Pojav katodnih vrhov je povezan z redukcijo kromovih in železovih oksidov znotraj trdne faze. Nobenega od opaženih vrhov ne pripisujemo Mo.

Ključne besede: dupleksno nerjavno jeklo, potenciostatske meritve, ciklična voltmetrija, pasivna plast

1 INTRODUCTION

Duplex stainless steels (DSSs) are widely used as structural materials in the oil and gas industries as well as for special applications in chemical, waste-water and marine-plant engineering, where a high mechanical strength and good corrosion resistance are required. The combination of ferrite and austenite phases in the volume ratio of about 1:1 results in a beneficial influence on the corrosion characteristics in various aqueous environments¹. The high Cr content together with high Mo and N contents gives rise to a high pitting-corrosion resistance in chloride solutions. The chromium adds to the overall resistance through a passivation process with forming a complex spinel-type passive film $(\text{Fe}, \text{Ni})\text{O}(\text{Fe}, \text{Cr})_2\text{O}_3$ ². Molybdenum increases the stability of the passive film and, therefore, the ability of the stainless steel to resist the localised corrosion, including pitting and crevice corrosion, particularly in environments containing chloride ions². The presence of approximately 50 % (by volume) of ferrite phase results in an increase in the strength compared with austenitic stainless steels^{3,4}.

Various electrochemical techniques have been used to study the corrosion behaviour of duplex stainless steels⁵⁻⁸. Souto et al.⁵ studied the passivation and the resistance to pitting corrosion of duplex stainless steel in neutral and alkaline buffered solutions, with and without chloride ions. The presence of NaCl enhanced the metal's electrodisolution through the passive layer. The

interpretation of the results was based on the presence of Cr and Ni in the alloy. Debala et al.⁶ showed that the corrosion resistance of superduplex stainless steel increased during annealing at heat-treatment temperatures lower than 1300 °C due to the improvement in the corrosion resistance of ferrite, which grows rich in Ni with temperature. Ahmad et al.⁷ studied the corrosion resistance of duplex stainless steel in sea water. It was found that 2205 duplex stainless steel showed good corrosion resistance in chlorinated and unchlorinated sea water at 25 °C, but at 50 °C it failed to resist. Torres et al.⁸ investigated 2205 duplex stainless steel in a chloride solution after various heat-treatments. The results showed that the simulated sensitisation had an adverse influence on the corrosion resistance, indicating that the corrosion rates increased by increasing the sensitisation temperatures.

In the present work 2205 duplex stainless steel is studied in various sodium chloride solutions. The study was conducted using the electrochemical techniques of cyclic voltammetry and potentiodynamic measurements.

2 EXPERIMENTAL

Duplex 2205 stainless steel was investigated. Its composition was confirmed by analytical chemical methods, as shown in **Table 1**.

The experiments were carried out in 0.9 %, 2 % and 3.5 % solutions of sodium chloride. All the chemicals were from Merck, Darmstadt, Germany.

Table 1: The composition of 2205 duplex stainless steel (w/%)**Tabela 1:** Sestava dupleksnega nerjavnega jekla 2205 (w/%)

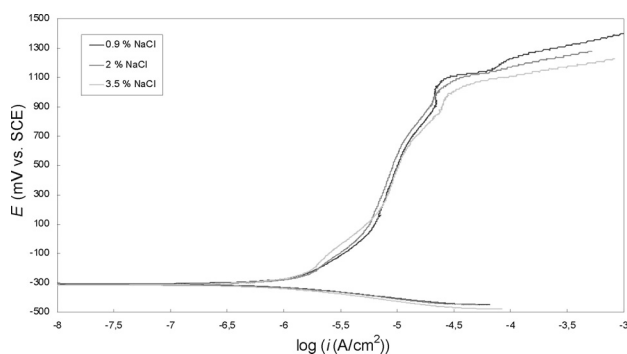
Material	Cr	Ni	Mn	Si	P	S	C	Mo
duplex 2205	22.74	5.74	1.37	0.38	0.032	0.001	0.03	2.57

The test specimens were cut into discs of 15 mm diameter. The specimens were grounded with SiC emery paper down to 1000 grit prior to the electrochemical studies, and then rinsed with distilled water. The specimens were then embedded in a Teflon PAR holder and employed as a working electrode. The reference electrode was a saturated calomel electrode (SCE, 0.242 V vs. SHE) and the counter electrode was a high-purity graphite rod.

The cyclic voltammetry and potentiodynamic measurements were recorded using an EG&G PAR PC-controlled potentiostat/galvanostat Model 263 with M252 and Softcorr computer programs. In the case of potentiodynamic measurements the specimens were immersed in the solution 1 h prior to the measurement in order to stabilize the surface at the open-circuit potential. The potentiodynamic curves were recorded, starting at 250 mV more negative than the open-circuit potential. The potential was then increased, using a scan rate of 1 mV s⁻¹, until the transpassive region was reached. In cyclic voltammetry a scan rate of 20 mV s⁻¹ was used, unless stated otherwise.

3 RESULTS

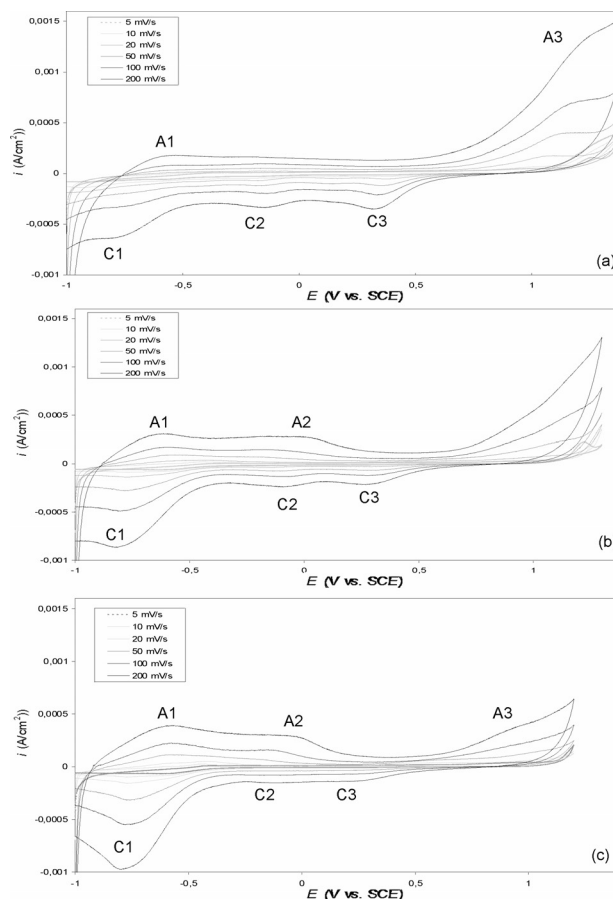
Figure 1 shows the potentiodynamic curves for 2205 DSS in mass fractions 0.9 %, 2.0 % and 3.5 % of sodium chloride solutions. After 1 h of stabilization at the open-circuit potential, the corrosion potential (E_{corr}) for 2205 DSS in all three solutions was approximately of -0.300 V. Following the Tafel region, the alloy exhibited passive behaviour. The extent of the passive range slightly decreased with the increasing chloride concentration. The passive range is limited by the breakdown potential (E_b), which corresponds to the oxidation of water and the transpassive oxidation of metal species.

**Figure 1:** Polarisation curves recorded for 2205 duplex stainless steel in chloride solutions of three different concentrations

Slika 1: Polarizacijske krivulje dupleksnega nerjavnega jekla 2205 v raztopinah natrijevega klorida z različnimi koncentracijami

The breakdown potential for 2205 DSS in a 0.9 % chloride solution was approximately 1.10 V, and this moved towards more negative values with an increasing chloride concentration, i.e., to 1.03 V and 1.00 V, respectively.

The cyclic voltammograms of 2205 DSS recorded in three different chloride solutions make it possible to compare the current peaks and the corresponding electrochemical processes taking place on the material investigated as well as the influence of the potential scan rate (ν) (**Figure 2**). The cyclic voltammograms were recorded at different scan rates in the potential range from -1 V to 1.2 V, 1.3 V and 1.4 V in 3.5 %, 2 % and 0.9 % NaCl, respectively. As can be seen, the main characteristics of the cyclic voltammograms are similar, with minor deviations in all three chloride solutions. In

**Figure 2:** Cyclic voltammograms recorded for 2205 duplex stainless steel with an increasing scan rate in (a) 0.9 % NaCl, (b) 2 % NaCl and (c) 3.5 % NaCl

Slika 2: Ciklični voltamogrami dupleksnega nerjavnega jekla 2205 pri različnih hitrostih spreminjanja potenciala s časom v: (a) 0.9 % NaCl, (b) 2 % NaCl in (c) 3.5 % NaCl

the presence of the 0.9 % NaCl, five peaks are observed (**Figure 2a**). The first anodic peak A1 at a potential -0.6 V can be ascribed to the electro-formation of Fe(II) hydroxide upon the Cr(III)-containing passivating layer, existing on the electrode at such negative potentials⁵. It is followed by the region with a constant current density, up to 0.5 V. Another peak in the anodic cycle A3 is observed in the transpassive region at a potential of 1.1 V, and this is associated with the oxidation of Cr(III) to Cr(VI)⁹. The Ni(II) species formed during the passivation process might have been oxidised to Ni(IV) oxide (NiO₂) in this potential range, too. In the reduction cycle in the potential range of peak C3 at 0.3 V Cr(VI) is reduced to Cr(III) and the iron oxide-hydroxide layer is largely reduced to Fe(II) in the potential range of peak C2, which is furthermore reduced in the potential range of peak C1 at -0.8 V⁹. In the presence of 2 % and 3.5 % NaCl another peak A2 at a potential range of 0 V is observed that corresponds to the conversion of the Fe(OH)₂ constituent to Fe(III) oxy-hydroxide FeOOH⁵ (**Figure 2b and c**).

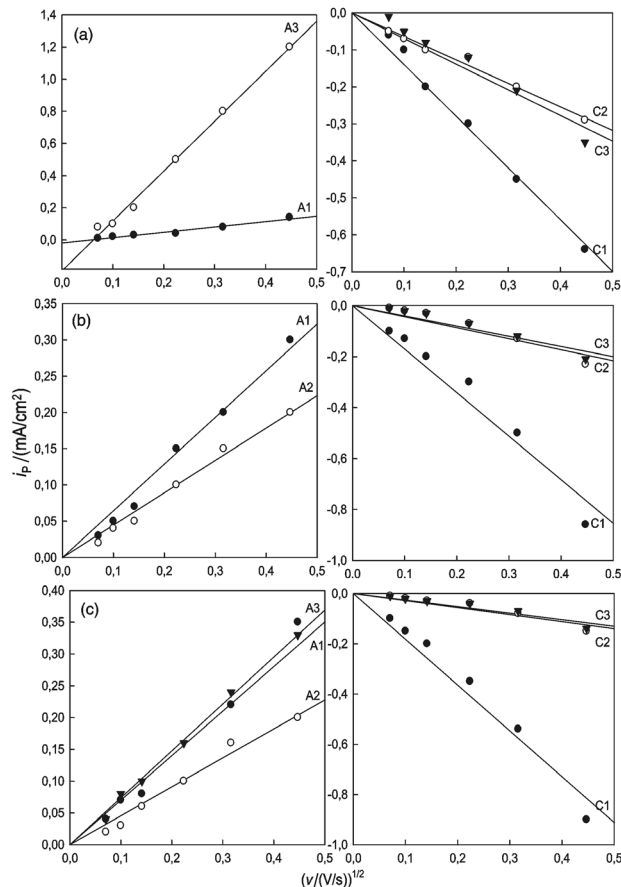


Figure 3: Calculated values of the peak current densities as a function of $\nu^{1/2}$ for 2205 duplex stainless steel in (a) 0.9 % NaCl, (b) 2 % NaCl and (c) 3.5 % NaCl

Slika 3: Izračunane vrednosti višine vrhov gostote toka i_p v odvisnosti od $\nu^{1/2}$ za duplexno nerjavno jekli 2205 v: (a) 0.9 % NaCl, (b) 2 % NaCl in (c) 3.5 % NaCl

Figure 3 shows the calculated values of the peak current densities as a function of $\nu^{1/2}$. In the presence of 0.9 % NaCl it is clear that the current densities of the anodic peaks A1 and A3 increase with increasing sweep rate. The plot of peak current densities vs. $\nu^{1/2}$ gives straight lines with slopes of 0.27 for peak A1 and 2.70 for peak A3. The line of peak A1 passes through the origin, while that of peak A3 meets the current axis at a negative current value. These results suggest that the oxidation process within the potential range of peak A1 is mainly diffusion controlled according to Delahay's equation¹⁰, while that which occurred in the potential range of peak A3 is a mixed controlled process. The straight lines of the cathodic peak current densities i_p vs. $\nu^{1/2}$ originate at the origin in accordance with Delahay's equation¹⁰ and have slopes of -1.40 , -0.63 and -0.69 , respectively. In the presence of 2 % and 3.5 % NaCl the straight lines of the anodic and cathodic peak current densities i_p vs. $\nu^{1/2}$ originate at the origin in accordance with Delahay's equation¹⁰ and are therefore mainly diffusion-controlled processes.

4 DISCUSSION

The corrosion-passivation processes of a duplex stainless steel polarised in neutral chloride solutions were investigated by using electrochemical techniques. Increasing the chloride concentration causes the surface films to become less stable and eventually film breakdown may occur. In this case, the potential range for passivity is subsequently reduced, and further growth of the oxide film is hindered as the metal electro-dissolution becomes the dominant electrochemical process⁵. Pit initiation appears to be related to both a loss in the protective characteristics of the passive layer, which increases as the applied potential moves in the positive direction, and to the presence of aggressive chloride ions in the electrolyte⁵. The passivity of stainless steels arises from the high corrosion resistance exhibited by the Cr(III) oxide-hydroxides present in the passivating layers. The role of the alloyed chromium in enhancing the passivity of stainless steels is frequently explained in terms of a percolation model of passivation⁵. It is assumed that chromium forms insoluble Cr₂O₃, and a continuous network of Cr-O-Cr-O is then produced, which prevents the dissolution of iron.

Though nickel additions have been claimed to benefit the corrosion resistance of ferritic steels where nickel is frequently present, some investigations with superferritic alloys without nickel suggested superior characteristics of the latter⁵. Therefore, Ni(II) must be regarded as less effective than Cr(III) in anchoring the water molecules and the hydroxyl ions, which are directly bounded to the metal ions forming complex species. In this way, chloride ions can migrate through the passivating layer by replacing the water and hydroxyl groups, accumulate

in the metal-oxide interface and cause localised corrosion.

Molybdenum increases the stability of the passive film and, therefore, the ability of the stainless steel to resist the localised corrosion, including pitting and crevice corrosion, particularly in environments containing chloride ions². This induced modification in the film can explain the increasing Cr³⁺/Cr⁶⁺ process in the voltammograms for DSS, which indicates the better corrosion characteristics of molybdenum-containing alloys.

5 CONCLUSIONS

An electrochemical study of the passive film generated in a chloride-containing medium on DSS 2205 was performed, and the results were analysed. Cyclic voltammograms obtained in the chloride solution showed characteristic peaks. The anodic peaks at -0.6 V, 0 V and 1.1 V were identified with the formation of Fe(OH)₂, FeOOH and the transpassive oxidation of Cr(III) to Cr(VI) and Ni(II) to Ni(IV), respectively. The reduction peaks at 0.3 V, -0.6 V and -0.8 V are attributed to valence transitions, occurring in the solid state, associated with the chromium and iron in the oxide, respectively.

None of the current peaks detected in the voltammetric curves can be attributed to the Mo species

alone, which indicates that molybdenum mainly enhances the effect of other passivating species, i.e., Cr, more than acting directly in the passivating process in chloride media. This conclusion explains the improved corrosion resistance of duplex stainless steels.

6 REFERENCES

- ¹ S. T. Tsai, K. P. Yen, H. C. Shih, *Corros. Sci.*, 40 (1998), 281–295
- ² J. A. Platt, A. Guzman, A. Zuccari, D. W. Thornburg, B. F. Rhodes, Y. Ossida, D. W. Thornburg, B. F. Rhodes, Y. Ossida, B. K. Moore, *American Journal of Orthodontics and Dentofacial Orthopedics*, 112 (1997), 69–79
- ³ F. Tehovnik, F. Vodopivec, L. Kosec, M. Godec, *Mat. Tech.*, 40 (2006), 129–138
- ⁴ A. Kocijan, Č. Donik, M. Jenko, *Corros. sci.*, 49 (2007), 2083–2098
- ⁵ R. M. Souto, I. C. Mirza Rosca, S. Gonzales, *Corrosion*, 57 (2001), 300–306
- ⁶ M. Debala, I. Calliari, A. Variola, *Journal of Materials Engineering and Performance*, 13 (2004), 237–240
- ⁷ S. Ahmad, A. U. Malik, *J. Appl. Electrochem.*, 31 (2001), 1009–1016
- ⁸ F. J. Torres, W. Panyayong, W. Rogers, D. Velasquez-Plata, Y. Oshida, B. K. Moore, *Bio-Medical Mat. Eng.*, 8 (1998), 25–36
- ⁹ N. Ramasubramanian, N. Preocanin, R. D. Davidson, *J. Electrochem. Soc.*, 132 (1985), 793–798
- ¹⁰ P. Delahay, *New instrumental methods in electrochemistry*. Interscience, New York, London, 1954, 115–145

A NUMERICAL SIMULATION OF METAL INJECTION MOULDING

NUMERIČNE SIMULACIJE BRIZGANJA KOVINSKIH PRAŠNATIH MATERIALOV

Boštjan Berginc¹, Miran Brezočnik², Zlatko Kampuš¹, Borivoj Šuštaršič³

¹University of Ljubljana, Faculty of Mechanical Engineering, 1000 Ljubljana, Aškerčeva 6, Slovenia

²University of Maribor, Faculty of Mechanical Engineering, 2000 Maribor, Smetanova ulica 17, Slovenia

³Institute of Metals and Technology, 1000 Ljubljana, Lepi pot 11, Slovenia

Prejem rokopisa – received: 2008-03-18; sprejem za objavo – accepted for publication: 2008-10-10

Metal injection moulding (MIM) is already a well-established and promising technology for the mass production of small, complex, near-net-shape products. The dimensions and mechanical properties of MIM products are influenced by the feedstock characteristics, the process parameters of the injection moulding, as well as the debinding and the sintering. Numerical simulations are a very important feature of the beginning of any product or technology development. In the article two different techniques for measuring the rheological properties of MIM feedstocks are presented and compared. It was established that capillary rheometers are more appropriate for MIM feedstocks, while on the other hand, parallel-plate rheometers are only suitable for shear rates lower than 10 s^{-1} . Later on we used genetic algorithms to determine the model coefficients for some numerical simulation software. The results of the simulation of the filling phase and a comparison with the experimental results are presented in the article.

Keywords: metal injection moulding, numerical simulation, genetic algorithms

Brizganje kovinskih prašnatih materialov (MIM) je uveljavljena tehnologija, primerna za izdelavo majhnih, kompleksnih izdelkov visoke natančnosti. Dimenzije in mehanske lastnosti MIM-izdelkov so odvisne od lastnosti mešanic, procesnih parametrov brizganja, odstranjevanja veziva in sintranja.

Numerične simulacije so pri razvoju novih izdelkov oziroma tehnologij zelo pomembne. V prispevku je narejena primerjava in predstavitev dveh metod za merjenje reoloških lastnosti MIM mešanic. Ugotovljeno je bilo, da je kapilarni reometer primernejši za meritve pri višjih strižnih hitrostih, medtem ko je reometer z vzporedno ploščo primeren le za strižne hitrosti do 10 s^{-1} . V nadaljevanju je bila uporabljena metoda genetskih algoritmov za določitev koeficientov matematičnega modela, ki se uporablja v programski opremi za numerične simulacije brizganja. Na koncu so predstavljeni rezultati simulacije polnjenja orodne votline, narejena pa je tudi primerjava z eksperimentalnimi rezultati.

Ključne besede: brizganje kovinskih prašnatih materialov, numerične simulacije, genetski algoritmi

1 INTRODUCTION

Powder injection moulding (PIM) or metal injection moulding (MIM) is a combination of four sequential technological processes – mixing, injection moulding, debinding and sintering – all of which have an effect on the characteristics of the final parts. The feedstock, which has to be as homogeneous as possible, is made by intensive mixing of the metal powder and the binder, and in the next phase a green part is made by injection moulding. Then the binder is removed from the green part in various debinding processes. The brown part that is produced retains its shape due to the friction between the particles of the metal powder. This part is very brittle and needs to be sintered carefully to achieve its final sintered density and the desired mechanical, chemical and dimensional properties. The final properties of the product can be further improved with additional heat and mechanical treatments.^{1,2}

A rheological characterisation of the selected feedstock, ADVAMET 316L, was performed using a parallel-plate and a capillary rheometer. On the basis of the viscosity measurement the coefficients of the

selected mathematical model were then determined and used for a numerical simulation with the Moldflow simulation software.

2 MIM FEEDSTOCK CHARACTERISATION

2.1 Viscosity measurement

MIM feedstocks usually consist of a binder, which is based on polymers and waxes, and metal particles. During the injection moulding their behaviour is similar to other shear thinning fluids. The increase in the shear rate causes the fluid's viscosity to decrease, which is well made use of in the injection-moulding process. A precise feedstock characterisation is thus needed for a complete understanding of the whole process as well as for finite-element-method-based (FEM-based) numerical simulations of injection moulding.

The viscosity of the ADVAMET 316L feedstock was measured with a Rheologic 5000 Twin Bore capillary rheometer and an Anton Paar Physica MCR 301 parallel-plate rheometer. The material ADVAMET 316L consists of a wax-polymer binder and spherical, austenitic stainless-steel powder particles with a diameter

smaller than 18 μm. L stands for the low carbon content, which is less than 0.03 %.

The Anton Paar rheometer was used to measure the melts' viscosity using a cylindrical rotating plate of diameter 21 mm. The shear stress is measured from the torque, which appears because of the material's resistance to flow. The sample of material was placed between the rotating disk and the immovable plate at a distance of 0.98 mm, while the temperature was held at 195 °C. The accuracy of this method is based on the supposition that the velocity of the melt at the rotating disk is the same as the velocity of the disk. The errors during the measurement are unavoidable at high velocities and for low-viscosity materials. The disadvantage of this method is that the shear rate is not the same throughout the whole cross-section of the disk. Therefore, the cone plate disks are more appropriate, but here a minimum distance between the rotating cone and the immovable plate that is only a few micrometers must be achieved. The metal particles in the MIM feedstock could hinder the disk rotation, and so a torque measurement would be incorrect. The basic principles of a viscosity measurement acquired with a parallel-plate rheometer are presented in **Figure 1**.

The apparent shear rate is calculated from the angle velocity ω, the distance δ and the plate radius r using the following relation:

$$\dot{\gamma}_{ap} = \frac{r \cdot \omega}{\delta} \quad (1)$$

while the shear stress τ is calculated from the torque M, measured on the axis using equation (2).

$$\tau = \frac{3M}{2\pi r} \quad (2)$$

These rheometers can be used for determining viscoelastic information about the tested material (creep test, zero-shear viscosity, relaxation modulus G, elastic modulus G' and viscous modulus G''), the data about the molecular structure and the rheological characteristics during a prolonged exposure to shear stress.^{3,4} **Figure 2** shows the shear-rate intervals for viscosity measurements with different measuring methods.

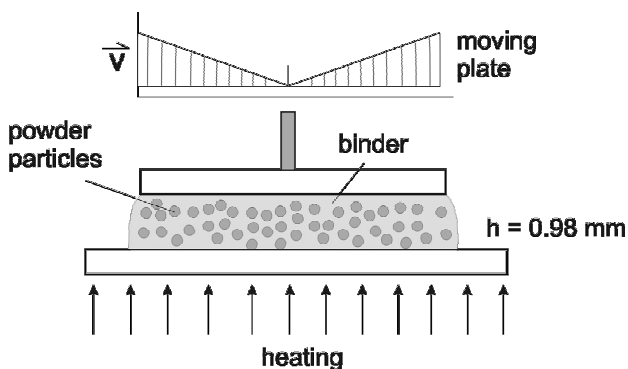


Figure 1: Parallel-plate rheometer
Slika 1: Reometer z vzporedno ploščo

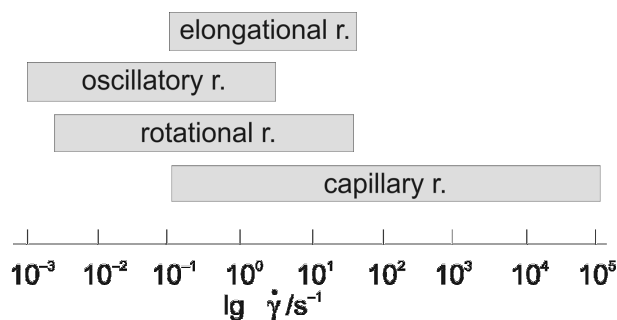


Figure 2: Shear rate for viscosity measurements with different methods

Slika 2: Območja strižnih hitrosti pri različnih metodah merjenja viskoznosti

With the capillary rheometer the volume flow rate of the extruded melt through a capillary of diameter 1 mm and length 20 mm was measured according to ISO 114433. The measurements were made in the temperature interval between 180 °C and 200 °C, while the shear rate was between 10⁻¹ and 10 000 s⁻¹. This method is appropriate for viscosity measurements on polymer materials, because the real conditions during the injection moulding and extrusion are similar to those during the viscosity measurement. The viscosity can be measured at high shear rates, and at the same time the measurements are accurate enough for further evaluation. The biggest disadvantages are a pressure drop at the entrance to the capillary, melt heating, and the dependence of viscosity on pressure. For an exact determination of the viscosity for non-Newtonian fluids the Weissenberg-Rabinowitsch and Bagly corrections are used (ISO 11443). The Bagley correction is used to determine the true shear stress due to the pressure drop at the entrance and exit of the capillary die.

The viscosity of non-Newtonian fluids calculated from the flow rate Q and shear stress τ, which is determined from the pressure drop Δp in the capillary, is the so-called apparent viscosity η_{ap}. The shear rate γ̇_{ap} and shear stress τ are calculated using equations (3) and (4):

$$\dot{\gamma}_{ap} = \frac{32Q}{\pi \cdot D^3} \quad (3)$$

$$\tau = \frac{\Delta p \cdot D}{4 \cdot L} \quad (4)$$

and so the apparent viscosity is

$$\eta_{ap} = \frac{\tau}{\dot{\gamma}_{ap}} \quad (5)$$

where D and L are the capillary diameter and the length. The Newtonian fluids are independent of shear rate, while the viscosity of the viscoelastic fluids is lowered by the increased shear rate. Thus, the Rabinowitsch correction for capillary-die rheometers is used afterwards to determine the true viscosity, which is calculated using equation (6):

$$\dot{\gamma} = \frac{\dot{\gamma}_{ap}}{4} \left(3 + \frac{d \lg \dot{\gamma}_{ap}}{d \lg \tau} \right) \quad (6)$$

where $d \lg \dot{\gamma}_{ap} / d \lg \tau$ is the slope of the curve $\lg \dot{\gamma}_{ap} = f(\lg \tau)$. The difference between the apparent viscosity and the true viscosity is usually smaller than 30 %. The apparent viscosity is accurate enough for determining the fluid's behaviour, and usually the true viscosity does not need to be calculated. On the other hand, it is recommended that we determine the true viscosity for an analysis with numerical simulations; however, in our case we did not have the resources to perform three viscosity measurements using different D/L capillary ratios in order to use the Bagley correction. Instead, we used the apparent viscosity for a numerical simulation of the filling phase using a Moldflow Plastic Insight 5.0. The comparison between the apparent viscosity and the true viscosity is presented in **Figure 3**.

Figures 4 and 5 show the results of viscosity measurements for the selected feedstock using both methods. The viscosity measurement using a parallel plate (**Figure 4**) shows that the shear stress increases only to the point when the shear rate reaches 10 s^{-1} , after which it decreases. The shear rates during high-pressure MIM can be up to 1000 times the stated shear rate. As regards the measurements, we would like to approach the actual processing conditions, but this was not possible with this method. The decrease of the shear stress could be the result of a thin layer of the binder near the wall (wall slip), which acts as a lubricant and lowers the friction of the fluid flow or because of a fracture of the test sample's edge. These effects probably already appeared when the shear rate was 5 s^{-1} , because above this value the shear stress increases more slowly.

A serious edge effect can appear with high-viscosity fluids like polymers and MIM feedstocks, where at low shear rates $\dot{\gamma} < 10 \text{ s}^{-1}$ the sample appears to cut at the midplane. Before this effect is visible it can be detected by a drop in the torque ⁵. The wall-slip effect can be partially avoided by using a roughened parallel-plate

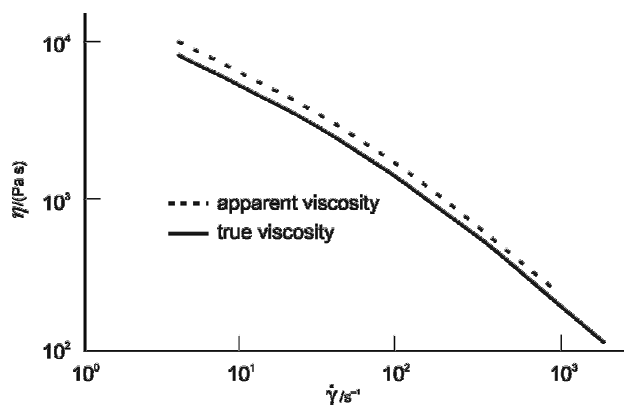


Figure 3: An example of the apparent and the true viscosity calculated using the Rabinowitsch correction

Slika 3: Primer navidezne in prave strižne viskoznosti, izračunane z Rabinowitschevo korekcijo

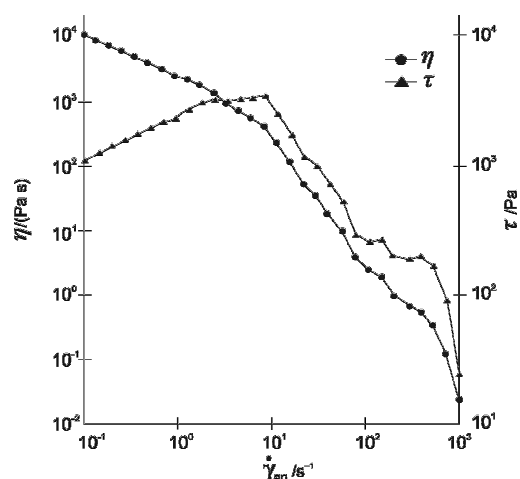


Figure 4: Viscosity and shear stress of ADVAMET 316L feedstock measured with the parallel-plate rheometer.

Slika 4: Z reometrom z vzporedno ploščo izmerjena strižna viskoznost in napetost za material ADVAMET 316L

surface or by making grooves and notches ⁶. The wall-slip effect of filled materials was investigated in several studies ⁶⁻⁹. For shear rates higher than 10 s^{-1} , when a critical shear stress is probably reached, the melt fractures and the shear stress and viscosity decrease rapidly. The adhesion and cohesion between the molecules is lower for materials filled with solid particles. Therefore, the shear stress decreases or oscillates when the adhesion restores or breaks ³.

The viscosity determined with the capillary rheometer decreases linearly in a log-log diagram in the interval between 10 s^{-1} and 10000 s^{-1} (**Figure 5**). After the comparison of the two methods for the viscosity determination of MIM feedstocks we established that the parallel-plate method is only suitable for lower shear

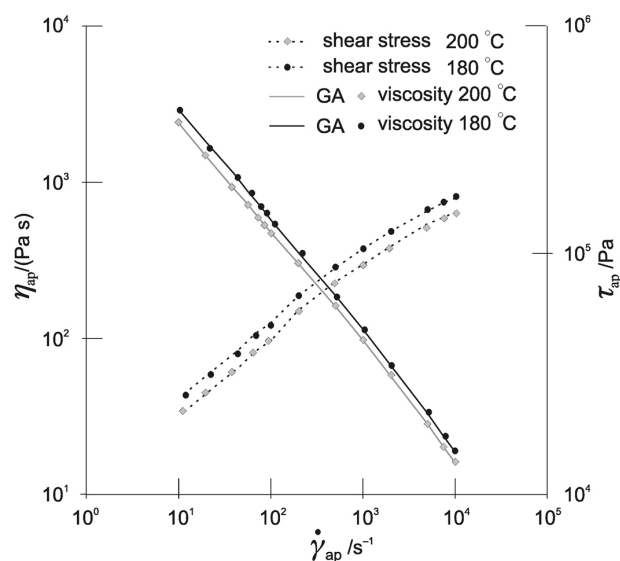


Figure 5: Viscosity and shear stress of ADVAMET 316L feedstock measured with the capillary rheometer

Slika 5: S kapilarnim reometrom izmerjena strižna viskoznost in napetost za material ADVAMET 316L

rates, while higher share-rate measurements should be made with capillary rheometers. The conditions in the latter method are similar to the real process conditions.

2.2 The determination of the model coefficients for a numerical simulation

To successfully perform a numerical simulation the rheological and thermal data as well as a pressure-volume-temperature (pVT) diagram must be obtained. In this investigation we focused on a characterisation of the feedstock's rheological properties; the determination of the pVT diagram for this material is set for a future investigation.

According to a recent paper ¹⁰ it is possible to use commonly available commercial software for the simulation of thermoplastic injection moulding to make useful numerical simulations of the MIM process because the material properties of the thermoplastic and metal feedstocks are quite similar, from the point of view of numerical simulations.

For numerical simulations of the injection-moulding process it is normal to use two mathematical models, which show the dependence of the shear viscosity, η , the shear rate, $d\gamma/dt$, and the temperature, T . The first one is the so-called Cross-WLF model, and the other one is a second-order model. From these two mathematical models we chose the latter, because it is more suitable for materials with a decreased viscosity across the whole range of shear rates (**Figure 5**). The second-order model is given with the following equation:

$$\ln \eta = A + B \cdot \ln \dot{\gamma} + C \cdot T + D (\ln \dot{\gamma})^2 + E \cdot T \cdot \ln \eta + F \cdot T^2 \quad (7)$$

where η , $d\gamma/dt$ and T are the viscosity (Pa s), shear rate (s^{-1}) and temperature ($^{\circ}C$), respectively, while A to F are data-fitted coefficients.

The coefficients were determined using genetic algorithms (GAs) (Table 1). The coding of the organisms was as follows: the initial random population $P(t)$ consisted of real-valued vectors (organisms) and of the constants A , B , C , D , and F . The variable t is the generation time. The absolute deviation $D(i,t)$ of an individual organism i in generation time t was introduced as the fitness measure. It was defined as:

$$D(i,t) = \sum_{j=1}^n |E(j) - P(i,j)| \quad (8)$$

where $E(j)$ is the experimental value for the measurement j , $P(i,j)$ is the predicted value returned by the individual organism i for the measurement j , and n is the maximum number of measurements. Of course, the predicted value $P(i,j)$ is calculated by inserting the constants A to F into the second-order model (7). Eq. (8) is a standard fitness measure for solving regression problems, proposed by Koza ¹¹. The aim of the optimisation task is to find such a model (7) that Eq. (9) would give as low an absolute deviation as possible. However, because it is not necessary that the smallest values of

the above equation also mean the smallest percentage deviation of this model, the average absolute percentage deviation of all the measurements for an individual organism i was defined as:

$$\Delta(i) = \frac{D(i,t)}{|E(j)|n} \cdot 100 \% \quad (9)$$

The altering of the population $P(t)$ is affected by reproduction, crossover, and mutation. For the crossover operation, two parental vectors are selected randomly. Then the crossover takes place between two randomly selected parental genes having the same index. Two offspring genes are created according to an extended intermediate crossover, considered by Mühlenbeim and Schlierkamp-Voosen ¹². In the mutation operation, one parental vector is selected randomly. Then, the mutation takes place in one randomly selected parental gene. In both crossover and mutation the number of crossover and mutation operations performed on parental vector(s) is selected randomly.

The evolutionary parameters were as follows: population size, 100; maximum number of generations to be run, 4000; probability of reproduction, 0.1; probability of crossover, 0.3; and probability of mutation, 0.6. The method of selection for all three genetic operations was a tournament selection with a group size of 4.

Table 1: Coefficients of the second-order model determined with a GA

Preglednica 1: Koeficienti modela drugega reda, določeni z GA

A	16.0317	C	$-5.52 \cdot 10^{-2}$	E	$1.01 \cdot 10^{-3}$
B	$-7.81 \cdot 10^{-1}$	D	$-1.16 \cdot 10^{-2}$	F	$1.03 \cdot 10^{-4}$

3 EXPERIMENTS

The experiments were made on a KraussMaffei KM50/220c injection-moulding machine (**Figure 6**),



Figure 6: A photograph of the testing area with the injection-moulding machine and the surveyor's chain

Slika 6: Slika preizkuševališča s strojem za brizganje in merilno verigo



Figure 7: Green and sintered specimens used for the analyses
Slika 7: Zeleni in sintrani kos, uporabljen za analizo

with a standard 30-mm diameter screw. The pressure and temperature in the cavity were measured using Kistler’s sensor 6190A0,8 with a NiCr-Ni Type-K thermoelement, positioned 20 mm from the gate. The pressure charge signal was then amplified with Kistler’s charge amplifier 5039A222, which was connected to the PC through a digital acquisition card PCI-9114(A) DG/HG. We were able to measure the pressure in the cavity with the pressure sensor and then compare it to the machine’s injection pressure. The pressure data was later used for a comparison with the numerical simulation.

The test specimen used for the injection-moulding analysis is presented in **Figure 7**. The coefficients of the second-order model were used for the creation of new material in the Moldflow database. Other feedstock characteristics that are necessary for a numerical simulation are the thermal conductivity $\lambda = 1 \text{ W/mK}$ and the specific heat $c_p = 950 \text{ J/(kg K)}$. The recommended processing parameters for this feedstock are presented in **Table 2**. The dimensions of the part are $(55 \times 9 \times 5) \text{ mm}$ and the hole diameter is 5 mm.

Table 2: Recommended processing parameters for ADVAMET 316L
Preglednica 2: Priporočene vrednosti procesnih parametrov za ADVAMET 316L

Parameter	value
Material temperature	190 °C
Mold temperature	45–50 °C
Injection speed	< 8 cm ³ /s
Ejection temperature	60 °C

For the meshing we used Moldflow’s 3D meshing with tetrahedral elements, with a total number of around 24,000. The solver used for the analysis was Navier-Stokes with simulation of the inertia effect. Because the $p\nu T$ data was not determined, only the

filling phase of the injection-moulding process was preformed.

4 RESULTS

In **Figure 8** it can be seen that the injection time can be quite long, although the material is filled with metal powder. We successfully filled the cavity with an injection speed as low as 1 cm³/s, with an injection time of around 3 s. However, the parts that were filled for more than 1.5 s had explicit weld lines and so longer injection times are not recommended. From our studies we concluded that the lowest injection speed for thick parts should be around 4 cm³ /s, and for thinner parts around 8 cm³/s.

Several testing conditions were examined during the result comparison. From **Figure 9** it can be seen that the material flows easily, as the injection pressure necessary to fill the whole part is low (170 bar). A very low pressure is needed to fill the part up to the hole (80 bar). To overcome the resistance due to a thinner flow path, a higher pressure must be applied. Simulations show that when the injection time is 2 s, the necessary injection pressure to fill the whole part is 160 bar, while the pressure inside the cavity, where the sensor is, is 85 bar (**Figure 9**). The experiments showed that the necessary injection pressure at the defined injection time is 120 bar, while the cavity pressure rises to around 80 bar. Longer injection times demand higher pressures to fill the cavity. We can see that the cavity pressure during the simulation and in the experiment is almost the same. The larger difference among the hydraulic pressures is probably a result of its dependence on the type and size of the machine. Nevertheless, the results of the numerical simulations are in good agreement with the experiments.

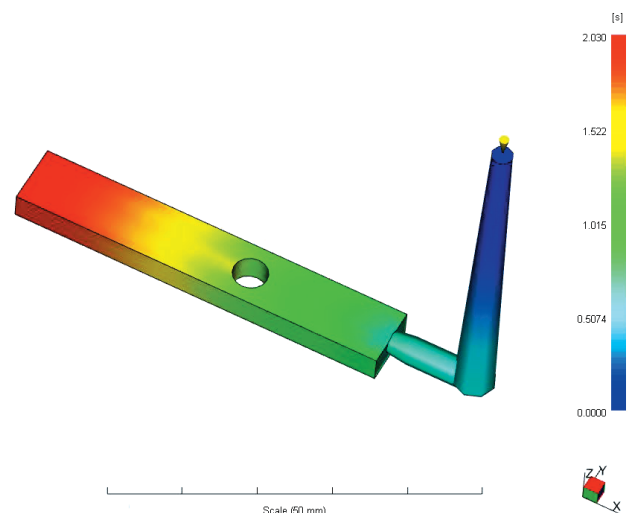


Figure 8: Simulation of the injection time of ADVAMET 316L
Slika 8: Z numerično simulacijo izračunan čas brizganja za ADVAMET316L

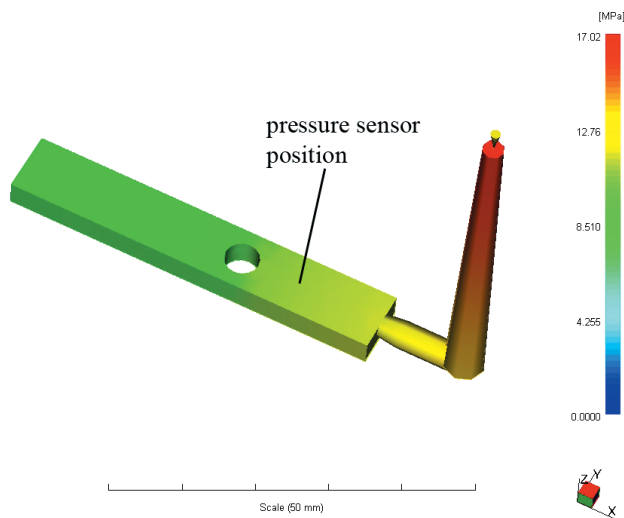


Figure 9: Simulation of injection pressure at the end of filling
Slika 9: Z numerično simulacijo izračunan tlak brizganja ob zapolnitvi orodne votline

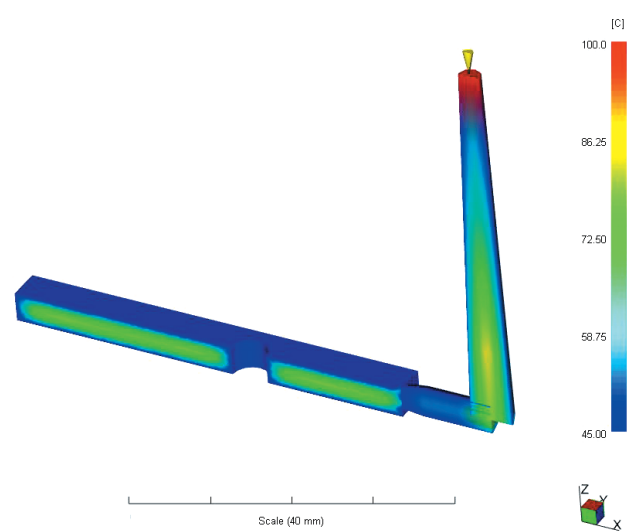


Figure 10: 3D temperature of MIM part, cooling time 15 s
Slika 10: Temperaturni profil MIM izdelka, pri času ohlajanja 15 s

During the experiment the temperature inside the cavity was also measured. Because of the material's high thermal conductivity the cooling times are rather low, even though the part is 5 mm thick. The part cooled almost to the mould temperature (48 °C) in around 30 s. The simulated cooling time and cooling time of the experiments were well correlated, because the results were practically identical. In **Figure 10** we can see that after 15 s the temperature inside the part is still 80 °C, while the mould temperature is 45 °C.

This practical experiment taught us that the part retains its shape and tolerances better if it is cooled almost to the mould temperature. If the part were to be ejected when the temperature of the core was higher than 80 °C, the part's shape retention would be reduced and this would result in bending and distortion. The optimal cooling time for this part would be between 20 s and 25 s.

5 CONCLUSIONS

In our investigations we established that Moldflow software can be used for numerical simulations of MIM materials. We successfully applied a GA to determine the coefficients of the numerical viscosity model and the simulated filling process of the injection phase using the apparent viscosity. For a confirmation of the numerical simulations the experiments of the injection-moulding process were performed.

The viscosity was measured using parallel-plate and capillary rheometers, and the latter proved to be the only one suitable for viscosity measurements of high viscosity MIM feedstocks. The next steps in our research will be

measuring the $p-v-T$ data, a determination of the true shear rate, the use of GAs for other mathematical models and comparing the numerically simulated results with experiments.

Acknowledgements

The authors wish to thank CEAST S.p.A., Italy and the Jožef Stefan Institute, Ljubljana, for the viscosity measurements and Tecos, the Slovenian tool and development centre, Celje, for lending us the Moldflow license.

6 REFERENCES

- ¹ R. M. German: Powder Injection Moulding, New Jersey, MPIF, 1990
- ² R. M. German, A. Bose: Injection Molding of Metals and Ceramics, New Jersey, MPIF, 1997
- ³ R. W. Whorlow: Rheological Techniques 2nd edition, Ellis Horwood, 1992
- ⁴ M. Rides: Rheological characterisation of filled materials: a review, NPL Report DPEC-MPR 013, Teddington, UK, 2005
- ⁵ C. W. Macosko: Rheology, principles, measurements and applications, New York, Wiley-VCH inc., 1994.
- ⁶ H. A. Barnes: *J. Non-Newtonian Fluid Mech.*, 56 (1995), 221–251
- ⁷ T. H. Kwon, S. Y. Ahn: *Powder Technol.*, 85 (1995), 45–55
- ⁸ U. Yilmazer, D. M Kalyon: ANTEC, 1989, 1682–1686
- ⁹ D. M. Kalyon: *J. Mater. Process. Manuf. Sci.*, 2 (1993), 159–187
- ¹⁰ C. Binet, D. F. Heaney, R. Spina, L. Tricarico: *J. Mater. Process. Technol.*, 164–165 (2005), 1160–1166
- ¹¹ Koza, J. R. *Genetic programming*; The MIT Press: Massachusetts, 1992
- ¹² Gen, M.; Cheng, R. *Genetic algorithms and engineering design*; John Wiley & Sons: Canada, 1997

INVESTIGATION OF THE BEHAVIOUR IN CHLORIDE SOLUTION OF ALUMINIUM ALLOYS AS MATERIALS FOR PROTECTOR PROTECTIONS

RAZISKAVA VEDENJA ALUMINIJEVE ZLITINE, MATERIALA ZA VAROVALNE ELEKTRODE, V KLORIDNI RAZTOPINI

Darko Vuksanović¹, Petar Živković¹, Dragan Radonjić¹, Branka Jordović²

¹University of Montenegro, Faculty of Metallurgy and Technology, Cetinjski put bb, 81000 Podgorica, Republic of Montenegro

²Technical Faculty of Čačak, Svetog Save 65, 32000 Čačak, Republic of Serbia
darkov@cg.ac.yu

Prejem rokopisa – received: 2007-02-02; sprejem za objavo – accepted for publication: 2008-02-05

The aim of the investigations was to check the behaviour of Al–Zn–Sn aluminium cast alloys with additions of bismuth and gallium for potential application as a material for protecting protectors. The chemical composition, the mechanical characteristics, the microstructure and the corrosion properties were investigated. Particular attention was given to microstructural investigations aimed to identify the phases that might have an active role for corrosion in chloride solution. Three corrosion tests were used: change in the corrosion potential with time, determination of the values for polarisation resistance and the corrosion current, and potention-dynamic recording of the cathode and anode polarisation curves.

Key words: aluminium alloys, chloride solution, corrosion potential, polarisation resistance, corrosion current, polarisation curves

Cilj raziskave je bil preveriti vedenje litih zlitin Al–Zn–Sn z dodatkom bizmuta in galija kot možnih materialov za varovalne elektrode. Kemijske sestava, mehanske lastnosti, mikrostruktura in korozijske značilnosti so bile opredeljene. Posebna pozornost je bila namenjena mikrostrukturnim preiskavam, da se določi, katere faze bi lahko imele aktivno vlogo pri koroziji v kloridni raztopini. Ugotovljene so bile tri korozijske značilnosti: sprememba korozijskega potenciala s časom, polarizacijska upornost in gostota toka ter potenciodinamični katodna in anodna polarizacija.

Ključne besede: aluminijeve zlitine, kloridna raztopina, korozijski potencial, polarizacijska upornost, korozijski tok, polarizacijske krivulje

1 INTRODUCTION

The corrosion damage of various constructions, such as machines, vessels pipelines, ships, oil pipelines, docks is effectively resolved with electrochemical (i.e., active) protection. One of the procedures used is the protection of protectors that are applied for infrastructural objects, e.g., warehouses, shipyards, heat exchangers, and machines operating in aggressive environments, especially in the presence of chlorides. The procedure is based on the use of more electronegative alloys as the protectors (galvanic anodes or sacrificial anodes). The results of these investigations demonstrate the importance of using the proper method for the preparation of aluminium alloys.

Several factors influence the investigated protector alloys – the chemical composition, the alloying procedure the casting and the thermal treatment – and only with proper processing a high-quality alloy will be obtained.

2 EXPERIMENTAL

The protector alloys were melted in an electro-resistive furnace using a graphite crucible. The experi-

mental work consisted of four parts: 1) the preparation of alloys; 2) chemical analysis, determination of the mechanical properties and of the microstructure; 3) determination of the corrosive and electrochemical characteristics of alloys in a solution of 0.51 M of NaCl; 4) examination of the microstructure before and after the corrosion test. The chemical analysis was performed with an X-ray quantometer; the tensile strength, the yield point ($R_{0.2}$) and the relative elongation were determined with an electronic, universal tensile-testing machine in the company Kombinat Aluminium Podgorica. The corrosion tests were performed on computerised equipment using a saturated calomel electrode as a reference, while the metallographic analysis and the electron-probe microanalysis was carried out at the Technical Faculty of Čačak. For the qualitative metallographic analysis, the method of area assessing for the intermetallic phases, and linear intercept of the width of the secondary dendrite arms of the Al solid solution (DAS) were used. The DAS parameters were determined to verify the eventual influence of added elements on the hardening process and on the behaviour of the alloy in an aggressive environment. A scanning electron microscope (SEM) was used for the energy-dispersive x-ray spectroscopy (EDS).

3 RESULTS AND DISCUSSION

The chemical composition of the alloys is shown in **Table I**, and in **Table II** the mechanical properties of the cast alloys are presented. The content of zinc was in range 3.90–4.90 %, that of tin (with the exception of

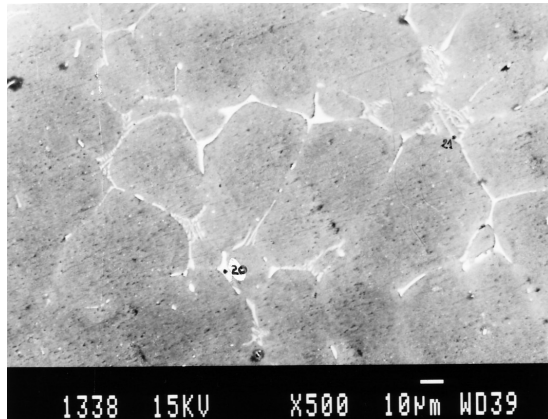


Figure 1: Microstructure of alloy 1 before the corrosion test. Magn. 500-times

Slika 1: Mikrostruktura zlitine 1 pred preizkusom korozije. Pov. 500-kratna

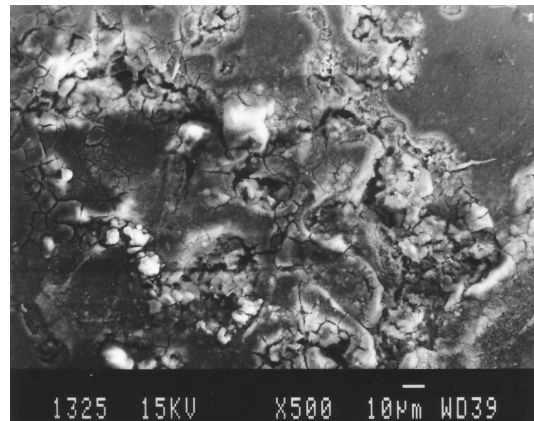


Figure 2: Microstructure of the alloy 1 after the corrosion test in 0.51-M NaCl. Magn. 500-times

Slika 2: Mikrostruktura zlitine 1 po preizkusu korozije v 0.51 M NaCl. Pov. 500-kratna

alloy 2) was 0.16–0.64 %, the content of bismuth in alloys 1 and 2 was 0.2–0.3 %, and that of gallium was 0.5 % in all alloys. The amounts of iron, silicon, titanium and copper were similar in all alloys.

The as-cast alloys have a low tensile strength and hardness, and a relatively large elongation. This combination of properties is favourable from the aspect of

Table I: Chemical composition of the alloys in mass fractions (w/%)

Tabela I: Kemična sestava zlitin v masnih deležih (w/%)

Alloy	Al	Zn	Sn	Bi	Ga	Fe	Si	Ti	Cu	V
1	94.209	3.9	0.64	0.2	0.5	0.36	0.11	0.012	0.05	0.01
2	94.794	3.95	-	0.3	0.5	0.28	0.11	0.008	0.04	0.01
3	94.035	4.9	0.16	-	0.5	0.27	0.1	0.007	0.01	0.01
4	94.613	3.95	0.47	-	0.5	0.28	0.1	0.009	0.06	0.01

Table II: Mechanical properties of the as-cast alloys

Tabela II: Mehanske lastnosti litih zlitin

Alloy	$R_{0.2}$ /(N/mm ²)	R_m /(N/mm ²)	A /%	HB /(N/mm ²)
1	44.5	69.7	6.8	30.3
2	45.6	52.2	4.0	34.6
3	47.5	97.1	14.4	30.9
4	43.5	67.5	5.6	31.9

Table III: Quantitative indicators for the microstructure of as-cast alloys

Tabela III: Kvantitativni kazalci za mikrostrukturo litih zlitin

Alloy	Surface of particle, IMF, A/µm ²	Perimeter, L_p /µm			Shape factor of perimeter			Shape factor of surface			Dendrite arm spacing DAS/µm			V_v , /%	Na·10 ³ µm*			
		min	max	sr	min	max	sr	min	max	sr	min	max	sr					
1	Al ₃ Fe	0.12	35	2.9	1.4	83	10	0.04	0.94	0.47	0.09	1	0.84	5.9	165	44	0.6	2.1
	SnBiAl	0.66	74	7.0	3.3	51.6	12	0.11	0.98	0.65	0.56	1	0.94				0.4	0.6
2	Al ₃ Fe	0.08	5.8	0.6	1.1	22.7	3.6	0.08	0.93	0.61	0.2	1	0.91	6	138	43	0.4	5.6
	BiZnAl	0.5	14.2	3.2	2.6	14.2	6.1	0.6	0.97	0.89	0.9	1	0.98				0.11	0.4
3	Al ₃ Fe	0.08	23.7	2.4	1.2	51	8.7	0.06	0.96	0.47	0.14	1	0.85	6.9	155	48	0.5	1.99
	SnAl	1	25	5.7	3.9	31	9.7	0.2	0.98	0.77	0.4	1	0.96				0.2	0.34
4	Al ₃ Fe	0.1	29	2.9	1.5	71	11	0.04	0.95	0.43	0.1	1	0.8	9.7	160	46	0.6	2.17
	SnAl	0.9	20	5.5	3.7	42	10	0.1	0.98	0.75	0.3	1	0.95				0.4	0.77

*Numerical density

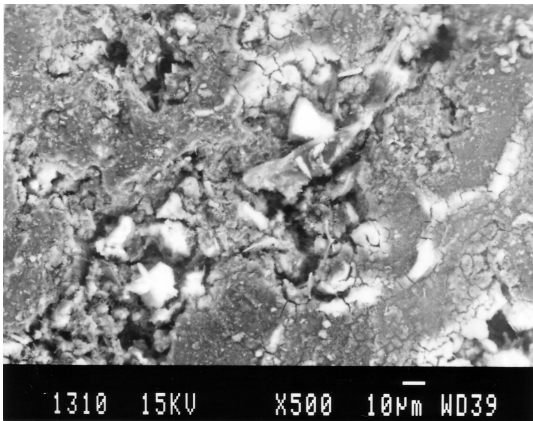


Figure 3: Microstructure of alloy 1 after the corrosion test in 0.051-M NaCl. Magn. 500-times

Slika 3: Mikrostruktura zlitine 1 po preizkusu korozije v 0.51 M NaCl. Pov. 500-kratna

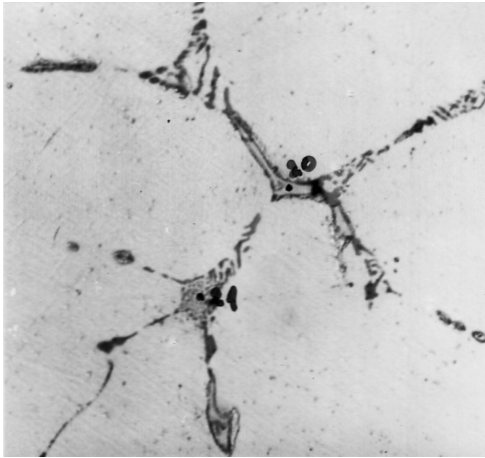


Figure 4: Microstructure of the alloy 1, phases Al_3Fe and SnBiAl . Magn. 730-times

Slika 4: Mikrostruktura zlitine 1, fazi Al_3Fe in SnBiAl . Pov. 730-kratna

the alloys' application, because their static and dynamic loading does not require a particular strength.

A detailed examination of the microstructure was carried out only for alloy 1, which contains all the elements of interest and relevant for the protection suitability. In **Table III** the quantitative indicators for the constituents of the microstructure of the cast alloys are shown, while the microstructure of alloy 1, before and after the corrosion test, is shown in **Figures 1 to 4**.

The alloys have a multiphase microstructure consisting of an Al solid solution and several phases, which differ in shape, size and distribution across the section of the sample. The phases AlBiSn and Al_3Fe were found in alloy 1. Phases based on gallium were not found, probably because of the unsuitability of the analytical equipment. From microstructural observations it was concluded that the gallium phases are located at the grain boundaries as well as inside the cells and dendrites.

In all the alloys an intermetallic phase based on aluminium and iron, with a small amount of zinc and silicon was found. According to the intensity of the

peaks on the recorded spectra and the particles morphology, the light-grey Al_3Fe phase that also contains zinc and silicon (**Figure 5**). As shown in the micrographs (**Figures 1 and 4**, mark 21), this phase is the eutectic constituent formed at the end of solidification. The particles of this phase are mainly in the shape of platelets of different size (**Table III**), when they are found in the normal degenerated eutectic. The volume share of this phase is in range 0.4–0.6 %. The total volume share of the intermetallic phases in all the investigated alloys was in the range 0.5–1.0 %. The type of second intermetallic phase depends on the chemical composition of the alloy. In alloy 1 the AlBiSn (**Figures 1 and 4**, mark 20) phase is present in the form of coarse, isolated particles with different shapes (angular, round, plate), and its composition is confirmed by the high intensity of the tin peak in **Figure 6**. Particles of this phase are found mostly at the dendrite boundaries. This phase remains bright after etching, since it is not attacked by the Keller's reagent. Its content (**Table III**) is particularly high in alloy 1, with the highest content of tin.

In alloy 2 the distribution of the phase Al_3Fe is very uniform (**Table III**). In addition to this phase the analysis showed a small amount of the AlBiZn phase (0.11 %) (**Figure 7**), mostly in the form of rounded

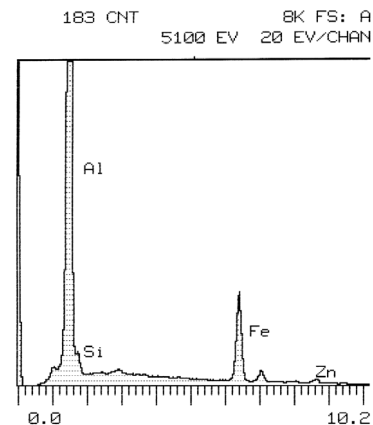


Figure 5: Maximum peak intensities, phase Al_3Fe
Slika 5: Največje intenzitete, faza Al_3Fe

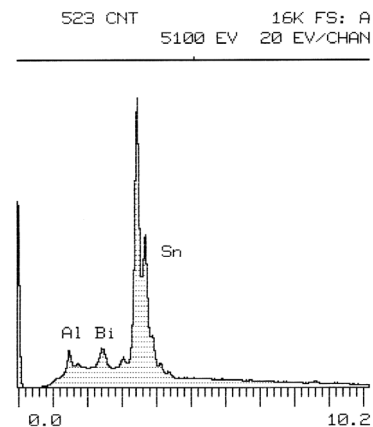


Figure 6: Maximum peak intensities, phase AlBiSn
Slika 6: Največje intenzitete, faza AlBiSn

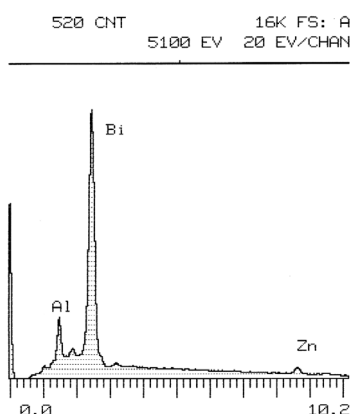


Figure 7: Maximum peak intensities, phase AlBiZn
Slika 7: Največje intenzitete, faza AlBiZn

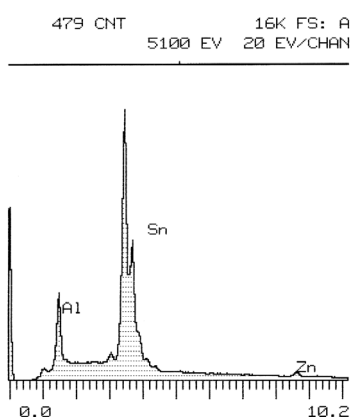


Figure 8: Maximum peak intensities, phase AlSn
Slika 8: Največje intenzitete, faza AlSn

particles at the boundaries; however, it is also inside the dendrites. A characteristic of this alloy are the small amounts of intermetallic phases (in total 0.5 %), which can probably be attributed to the absence of tin, which can form several intermetallic phases in these types of alloys. The analysis shows (Table III) that in alloys 3 and 4 a small amount of zinc is present in the phase AlSn (Figure 8).

The microstructural observations after a treatment in the chloride solution show the strongest attack taking place at the cellular-dendrite boundaries, where the intermetallic phases with a different electrochemical potential are located. During the corrosion test more of the matrix was dissolved than of the AlSn and AlBiSn phases. Also, the phases AlBiSn, AlBiZn and AlSn were dissolved during the test in the 0.51 M NaCl solution.

In Tables IV and V the values of the corrosion characteristics of the alloys in the 0.51 M NaCl solution are shown, while in Figures 9 to 12 the recordings on the tests of alloy 1 are shown. The analysis of the corrosion potential vs. time in 0.51 M NaCl indicates the temporal evolution of the potential to more positive values, up to the final value of -1327 mV. The negative value of the final potential is explained by the rapid dissolution in the test solution and by the rapid increase in the concentration of ions in the vicinity of the

electrode (Figure 11) and the slow diffusion of ions from the electrode area. At a corrosion potential of -1327 mV, in the 0.51 M NaCl solution the polarisation resistance and the corrosion current are $R_p = 0.1266 \text{ k}\Omega$ and $j_{\text{corr}} = 171.43 \mu\text{A}/\text{cm}^2$ (Figure 12).

During the test in the 0.51 M NaCl solution the dissolution of the alloy occurred virtually only at the grain boundaries where the AlBiSn particles were present. This could explain, for alloy 1, the very negative corrosion potential, the lower polarisation resistance and the higher corrosion currents. From the corrosion characteristics in Tables IV and V we can conclude that for a test in a more concentrated solution, such as the NaCl solution, a larger extent of solution of the phases provides a good characterization of the investigated alloy in terms of the application for protectors' protection.

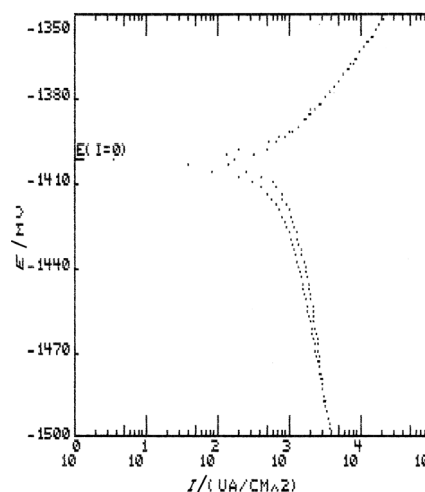


Figure 9: Potentiodynamic cathodic and anodic polarization curves for alloy 1 in 0.51 M NaCl. Scan rate 1 mV/s
Slika 9: Potenciodinamični katodna in anodna polarizacijski krivulji za zlitino 1 v 0.51 M NaCl. Hitrost skeniranja 1 mV/s

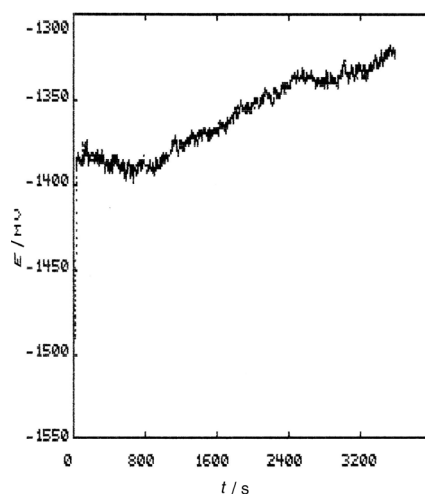


Figure 10: Corrosion potential vs. time for alloy 1 in 0.51 M NaCl
Slika 10: Časovna odvisnost korozijskega potenciala za zlitino 1 v 0.51 M NaCl

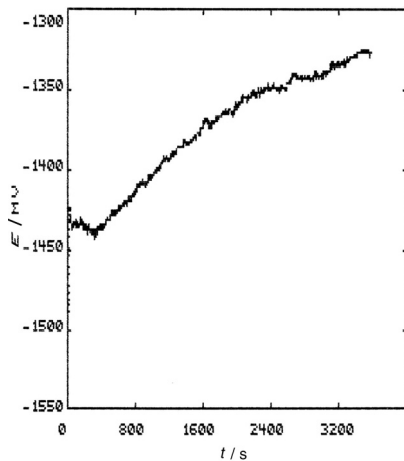


Figure 11: Corrosion potential vs. time for alloy 1 in 0.51 M NaCl
Slika 11: Časovna odvisnost korozivskega potenciala za zlitino 1 v 0.51 M NaCl

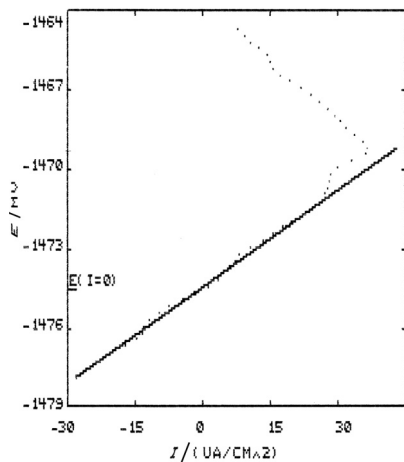


Figure 12: Polarization resistance for alloy 1 in 0.51 M NaCl. Scan rate 1 mV/s

Slika 12: Polarizacijska upornost za zlitino 1 v 0.51 M NaCl. Hitrost skaniranja 1 mV/s

Table IV: Dependence of corrosion potential vs. time in 0.51 M NaCl

Tabela IV: Odvisnost korozivski potencial – čas v 0.51 M NaCl

Alloy	E_{begin}/mV	E_{end}/mV
1	-1491	-1327
2	-1380	-1324
3	-1376	-1330
4	-1406	-1336

Table V: Polarization resistance in 0.51 M NaCl

Tabela V: Polarizacijska upornost v 0.51 M NaCl

Alloy	E_{corr}/mV	$E(j=0)/mV$	$R_p/k\Omega$	$j_{corr}/(\mu A/cm^2)$
1	-1469.25	-1474.75	0.1266	171.43
2	-1355.166	-1362.25	0.1936	112.12
3	-1334.2	-1345	0.0953	227.8
4	-1361.5	-1375	0.2065	105.14

During the corrosion test for the AlBiSn and AlBiZn phases, higher values of polarisation resistance and lower corrosion currents were obtained than for the phase AlSn in alloy 3. In the presence of the phase AlSn, alloy 4 shows a lower corrosion current and a higher polarization resistance than alloy 3, although the tin content is higher in alloy 4. The difference may be related to the difference in the content of zinc, which is lower in alloy 4.

4 CONCLUSION

The experimental findings in this investigation show that:

- the investigated alloys have poor mechanical characteristics and cannot be used in cases of significant static and dynamic stressing;
- the chemical composition strongly affects the corrosion activity of the aluminium alloys;
- the solution of the matrix is faster at the grain boundaries than the solution of the AlSn and AlSnBi phases;
- the alloys 3 and 4 show great corrosion activity in chloride solutions, while alloy 3 shows better corrosion characteristics.

It is justifiable to continue with the investigations on alloy 3 with the aim to verify the effect of the content of tin on the corrosion activity.

5 REFERENCES

- ¹ L. F. Mondolfo, Aluminum alloys-structure and properties, Butterworths, 1976
- ² S. A. Gincberg, Formation and dissolution behavior of anodic oxide films on aluminum, Japan 1979, 438–456
- ³ J. G. Ivašina, L. E. Šprengelj, Zaštita truboprovodov ot korozii, 1980, 5–7
- ⁴ D. R. Salinas, S. G. Garcia, J. B. Bessone, Influence of alloying elements and microstructure on aluminium sacrificial anode performance: case of Al–Zn, Journal of Applied Electrochemistry, 29 (1999) 9, 1063–1071
- ⁵ S. Valdez, M. A. Talavera, J. Genesca, J. A. Juarez-Islas, Activation of an Al–Zn–Mg–Li alloy by the presence of precipitates to be used as sacrificial anode, Mat. Res. Soc. Symp. Proc., 654 (2001), 351–356

IMPROVING THE PROCESS CAPABILITY OF A TURNING OPERATION BY THE APPLICATION OF STATISTICAL TECHNIQUES

IZBOLJŠANJE PROCESA SPOSOBNOSTI STRUŽENJA Z UPORABO STATISTIČNE TEHNIKE

Aysun Sagbas

Mersin University, Tarsus Technical Education Faculty, Department of Mechanical Education, 33400 Tarsus-Mersin/TURKEY
asagbas@mersin.edu.tr

Prejem rokopisa – received: 2008-08-05; sprejem za objavo – accepted for publication: 2008-10-22

Process-capability indices are effective tools for the continuous improvement of quality, productivity and managerial decisions. Statistical process-control techniques improve the quality in mass production. In this study, a process-capability analysis was carried out in the machining line of a medium-sized company that produces machine and spare parts. For this purpose, normal probability plots and histograms were prepared and the process-capability indices C_p and C_{pk} were calculated. It is shown that the process capability for the whole process was inadequate and that the mass production was unstable. In order to satisfy the process-capability measures it is necessary to improve the quality level by shifting the process mean to the target value and reducing the variations in the process.

Keywords: process capability analysis, quality improvement, turning operation

Indeksi sposobnosti so za procese učinkovita orodja za stalno izboljševanje kakovosti, produktivnosti in vodstvenih odločitev. Statistična tehnika kontrole procesa omogoči izboljšanje kakovosti pri masovni proizvodnji. V tej študiji je bila izvršena ocena procesa za obdelovalno linijo srednje velike družbe, ki izdeluje stroje in rezervne dele. Za ta namen so bili pripravljene histogrami normalne verjetnosti in izračunani indeksi sposobnosti procesa (C_p in C_{pk}). Pokazalo se je, da je bila procesna sposobnost za celoten proces neprimerna in je zato bila nestalna masovna proizvodnja. Za izboljšanje stanja je bilo treba sprejeti ukrepe za dvig nivoja kakovosti s premikom povprečja procesa na ciljno vrednost in znižati njegovo variabilnost.

Ključne besede: analiza sposobnosti procesa, izboljšanje kakovosti, struženje

1 INTRODUCTION

Process-capability analysis is a technique applied in many stages of the product cycle, including process, product design, manufacturing and manufacturing planning, since it helps to determine the ability to manufacture parts within the tolerance limits and engineering values. There are several capability indices, including C_p , C_{pu} , C_{pl} and C_{pk} , that have been widely used in manufacturing industry to provide common quantitative measures of process potential and performance. Process-capability indices are powerful means of studying the process ability for manufacturing a product that meets specifications^{1,2}.

There is considerable theoretical and experimental research work on improving product quality and process efficiency using a process-capability analysis. Kane³ described six areas of application for capability indices: the prevention of the production of nonconforming products, the continuous measure of improvement, communication, prioritization, the identification of directions for improvement, and the auditing of the quality system. Wright⁴ discussed the cumulative distribution function of process-capability indexes.

The process-capability indices, including, C_p , C_{pk} and C_{pm} , have been proposed in manufacturing industry to

provide a quick indication of how a process has conformed to its specifications, which are preset by manufacturers and customers. Pearn et al.⁵ indicated the index of capability for monitoring the accuracy of the manufacturing process. Singhal⁶ introduced the multi-process performance-analysis chart (MPPAC) based on process-capability indices for controlling and monitoring multiple processes. The MPPAC provides an easy way to process improvement by comparing the locations on the chart of the processes before and after the improvement effort. Pearn and Chen⁷ proposed a modification to the MPPAC, combining the more advanced process-capability indexes C_{pm} and C_{pmk} to identify the problems causing the process failing to centre around the target. Pearn et al.⁵ introduced the MPPAC based on the capability index, which is a simple transformation of C_{pmk} . They developed the multi-process performance-analysis chart based on process-capability indices to analyze the manufacturing performance for multiple processes. Deleryd et al.⁸ investigated experiences of implementing statistical methods in two small companies from the ceramics industry. Motorcu and Güllü⁹ used some statistical calculations to eliminate quality problems, such as undesirable tolerance limits and the out of circularity of spheroidal cast-iron parts during machining. Dolinsek and Kopac¹⁰ presented particular examples of

machining crank shafts. From the results obtained from statistical process control (SPC), they identified tool wear and machine inaccuracies. Deleryd ¹¹ performed a survey among 97 Swedish organizations that use process-capability studies. Corbett and Pan ¹² described a quantitative procedure for the monitoring and evaluating of environmental performance using statistical process-control techniques. Chang and Wu ¹³ provided explicit formulas with efficient algorithms to obtain the lower confidence bounds and sample sizes required for the specified precision of the estimation of C_{pk} for processes with asymmetric tolerances. Ramakrishnan et al. ¹ discussed process-capability indices and product reliability. Chen et al. ¹⁴ constructed a process-capability-monitoring chart (PCMC) for evaluating the process potential and performance for the silicon-filler product, which is designed for practical applications.

The purpose of this study was to focus on the process-capability analysis in a medium-sized company to eliminate quality problems during machining. A normal distribution curve and histograms were prepared, the process-capability indices were calculated, and the number of nonconforming parts was determined.

2 PROCESS-CAPABILITY STUDIES AND PROCESS-CAPABILITY INDICES

Process-capability indices have been widely used to measure product qualities and process performance that meet specifications in the manufacturing industries. The procedure for the analysis of process performance is shown in **Figure 1**.

Many engineers use process-capability indices as communication indicators to evaluate the manufacturing process. The quality characteristics of items are often

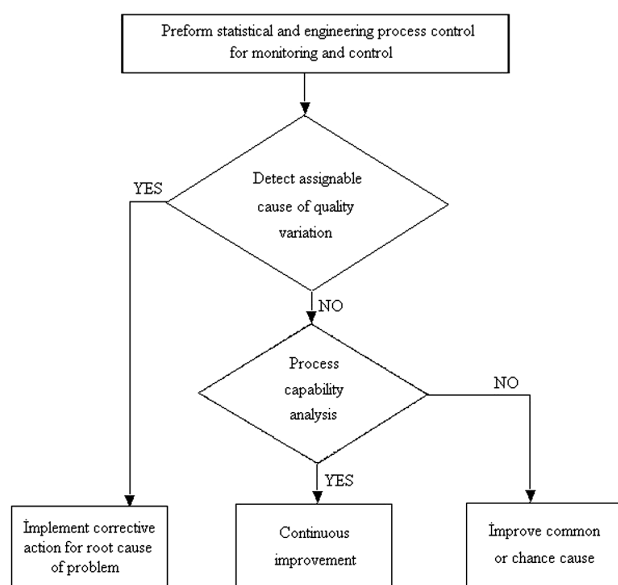


Figure 1: Analysis procedure for process performance
Slika 1: Procedura analize lastnosti procesa

measured in order to determine the capability of the production process. Usually, the customer determines a specification area or tolerance zone by setting lower and upper specification limits to require a certain quality from the supplier. Process capability is the repeatability and consistency of a manufacturing process relative to the customer's requirements ¹⁵. Since the estimated capability index is a random variable with a distribution, most engineers look at the value of the capability index calculated from the given sample and then draw a conclusion on whether the given process is capable or not and whether or not it is reliable. When a process is in a state of statistical control, and only then, the process can be evaluated with respect to its ability to produce items within specifications. Obviously, the variability of the process is a measure of the consistency of the output products. The stability of a process is an important property, since, if the process is stable in the current frame, then it is likely to stay in a stable condition in the future. Thus, the output of a stable process is in some sense predictable. There are several capability indices, including C_p , C_{pu} , C_{pl} , C_{pk} , C_{pm} and C_{pmk} . Process variation, process departure, process yield, and process loss have been considered as crucial benchmarks for measuring process performance. The index C_p considers the overall process variability relative to the specification tolerance, and therefore it only reflects the consistency of the product's quality characteristic. The index C_{pk} takes the mean of the process into consideration, but it can fail to distinguish between on-target processes and off-target processes, which is a yield-based index providing lower bounds on the process yield ². The index C_{pm} takes the proximity of the process mean from the target value into account, which is more sensitive to process departure than C_{pk} . Since the design of C_{pm} , is based on the average process loss relative to the specification tolerance, the index C_{pm} provides an upper bound of the average process loss, which is also referred to as the Taguchi index or the loss-based index. The index C_{pmk} is constructed from combining the modifications to C_p that produced C_{pk} and C_{pm} , which inherits the merits of both indices. The index C_{pmk} indeed provides more quality assurance with respect to process yield and process loss to the customers than the other two indices, C_{pk} and C_{pm} . The most widely used capability indices in industry are defined with Eq. 1 and 2. ^{1,13}.

$$C_p = \frac{USL - LSL}{6\sigma}$$

$$C_{pk} = \min \left\{ \frac{USL - \mu}{3\sigma}, \frac{\mu - LSL}{3\sigma} \right\} = \frac{d - |\mu - M|}{3\sigma} \quad (1)$$

$$C_{pk} = C_p(1 - k)$$

$$k = \frac{|\bar{T} - \mu|}{0.5(USL - LSL)} \quad (2)$$

where USL is the upper specification limit, LSL is the lower specification limit, σ denotes the process' stan-

standard deviation, μ denotes the process mean, d is the half-length and M is the midpoint of the specification interval. T is the target value, and k is the variation factor. When the process is perfectly on target, $k = 0$ and $C_{pk} = C_p$ from Eq.(2), the maximum value for C_{pk} is C_p . Examples of the estimation of the capability-process indices C_p and C_{pk} are introduced in **Table 1**.

Table 1: Examples of process estimation based on the indices C_p and C_{pk}

Tabela 1: Dva primera ocene procesa na podlagi indeksov C_p in C_{pk}

Capability index	Estimation of the process
$C_{pk} = C_p$	Process is placed exactly at the centre of the specification limits
$C_p < 1$	Process is not adequate
$1 \leq C_{pk} < 1.33$	Process is adequate
$C_p \geq 1.33$	Process is satisfactory enough
$C_p \geq 1.66$	Process is very satisfactory
$C_{pk} \neq C_p$	Process is inadequate, new process parameters must be chosen

3 PROCESS-CAPABILITY ANALYSIS IN TURNING

The following case is taken from a medium-sized casting and manufacturing factory, making various types machine and spare parts in Istanbul, Turkey. The workpiece was cast, spheroidal iron, cast GGG-40, using investment casting and machined using an industrial type

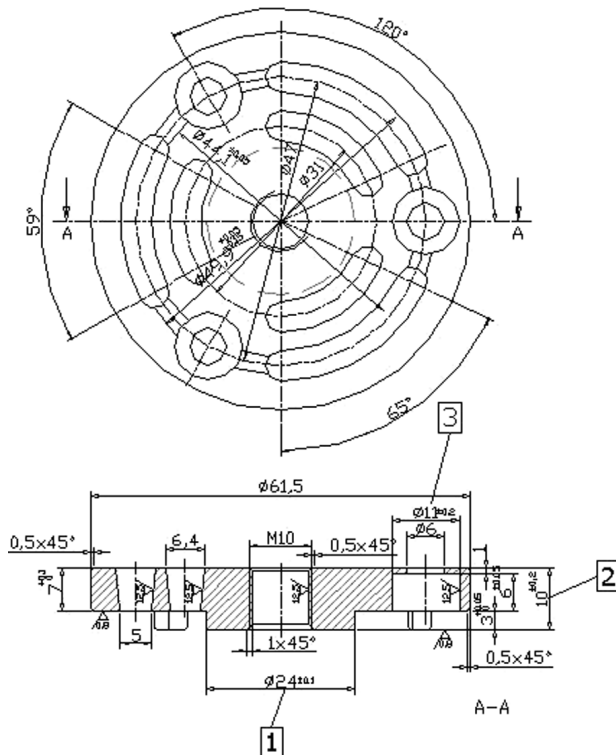


Figure 2: The dimensions and tolerance values of the workpiece and technical drawing

Slika 2: Dimenzije in tolerance za obdelovanec in tehnični načrt

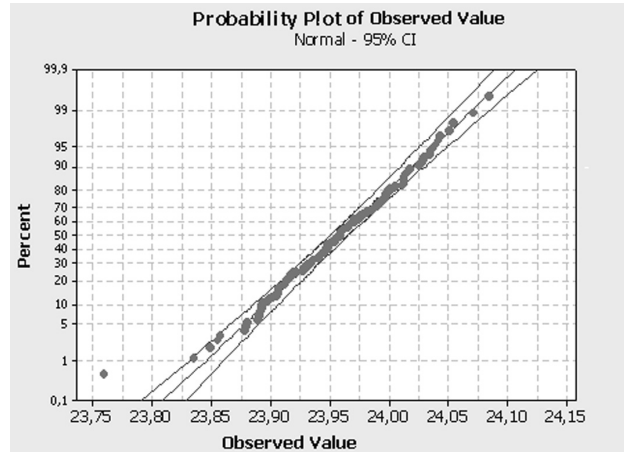


Figure 3: Normal probability plot for quality characteristic ($\text{Ø } 24 \pm 0.1$)

Slika 3: Odvisnost normalne verjetnosti za karakteristično kakovost ($\text{Ø } 24 \pm 0.1$), $N = 150$

lathe machine. The workpieces were machined under dry conditions, and ceramic-based cutting inserts were used. The quality characteristics considered are shown in 1, 2, and 3 in **Figure 2**. The dimensions and tolerance values of the workpiece and the technical drawing are shown in **Figure 2**.

In this study, in order to demonstrate the applicability of the proposed method and to make a clear decision about the capability of the machining process, the sample size was determined and a sufficient number of sample parts was inspected. A single sampling plan was implemented by using the lot-acceptance sampling plan. Samples were chosen randomly during the turning process. The data for the investigated characteristics were collected for 30 days in the company, determined for 150 samples, i.e., 30 % of a lot size of 500 parts. The same number of workpieces ($N = 150$) was measured every day. Normal probability plots and histograms were prepared and statistical parameters were calculated using the measured values taken from the workpieces that

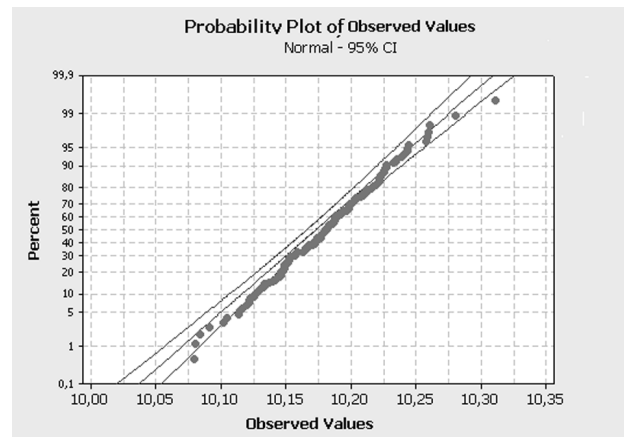


Figure 4: Normal probability plot for ($\text{Ø}10 \pm 0.2$)

Slika 4: Normalna verjetnostna odvisnost za ($\text{Ø}10 \pm 0.2$), $N = 150$

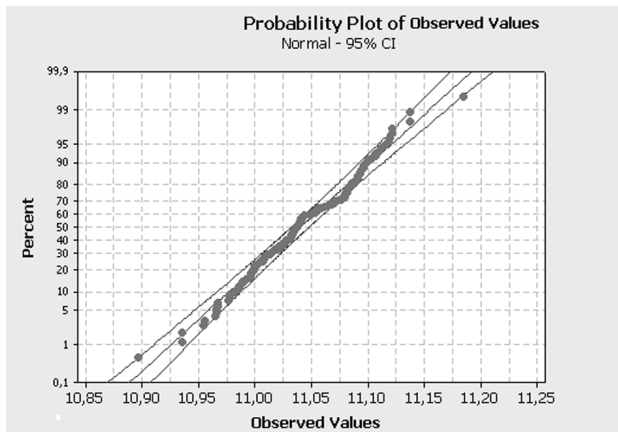


Figure 5: Normal probability plot for ($\text{Ø}11 \pm 0.2$)
Slika 5: Normalna verjetnostna odvisnost za ($\text{Ø}11 \pm 0.2$), $N = 150$

represent the whole process. To receive a numerical measure of the capability, the so-called process-capability indices were calculated. In all the stages of data analysis, Minitab software was used. The validity of the normality was verified using the Chi-square test, χ^2 . **Figures 3, 4 and 5** display the normal probability plots of the sample data and from these figures the sample data appear to be normal.

Figures 6, 7 and 8 display the histograms of the 150 observations with a density line and specification limits (LSL , T , USL) and the results of the process-capability analysis.

Figure 6 shows that the process capability deteriorated during the monitoring period to C_p and $C_{pk} < 1$, which indicates the potential risk of an increase in the number of nonconforming parts. It denotes that the process capability is inadequate. For $C_p \neq C_{pk}$ the process mean is not centred for the process width. The number of non-conforming parts out of the LSL is 120,000 and there is a none value out of the USL in the observed performance. In a short period of time, the non-conforming parts out of the LSL is 119,010 ppm and out of the USL is $1837 \cdot 10^{-6}$. In a long period of time,

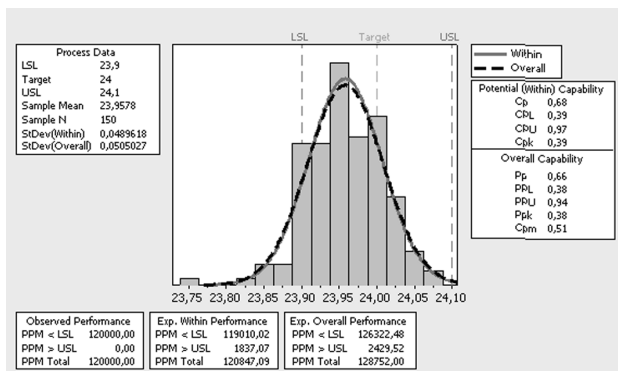


Figure 6: Histograms and process-capability analysis for quality characteristic ($\text{Ø}24 \pm 0.1$)
Slika 6: Histogram analize procesne sposobnosti za karakteristično kakovost ($\text{Ø}24 \pm 0.1$), $N = 150$

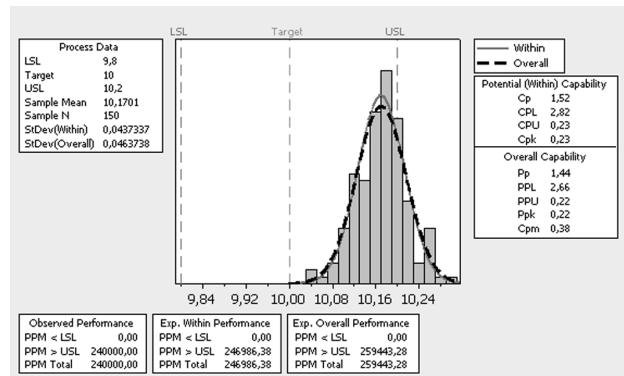


Figure 7: Histograms and process-capability analysis for quality characteristic ($\text{Ø}10 \pm 0.2$)
Slika 7: Histogram analize procesne sposobnosti za karakteristično kakovost ($\text{Ø}10 \pm 0.2$)

the number of non-conforming parts out of the LSL is $126,322 \cdot 10^{-6}$ and out of the USL is $2429 \cdot 10^{-6}$. This analysis shows that the specification limits should be rearranged and the process variability should be reduced.

Since the calculated C_p value (1.52) is bigger than 1.33 and the C_{pk} value (0.23) is lower than 1.00, the process is inadequate. Some measures must be taken immediately and new process parameters must be chosen. For $C_p \neq C_{pk}$, the process mean is not centred with the process width. If the process mean is not centred relative to the specification limits, the process-capability index will give misleading results. The process mean is near to USL . The number of non-conforming parts out of the USL is 240,000 and there is no value out of the LSL in the observed performance. The number of non-conforming parts out of the USL is $246,986 \cdot 10^{-6}$ in a short period of time and $259,443 \cdot 10^{-6}$ in a long period of time. In the short and long periods of time the data fall out of the LSL . As the process-capability indices calculated are clearly different, there will be different percentages of non-conforming products. In short and long periods of time the number of parts produced out of the USL will be

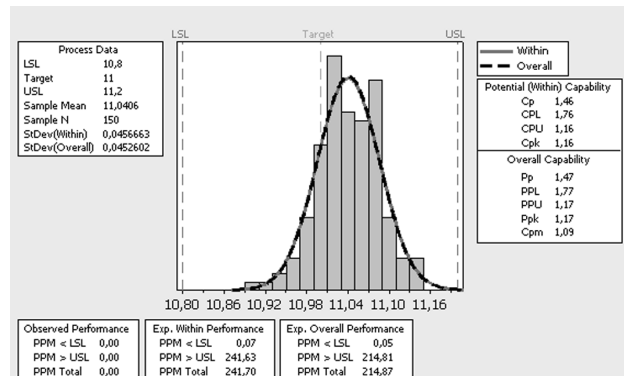


Figure 8: Histograms and process-capability analysis for quality characteristic ($\text{Ø}11 \pm 0.2$)
Slika 8: Histogram analize procesne sposobnosti za karakteristično kakovost ($\text{Ø}11 \pm 0.2$)

increased. In order to satisfy the process capability, some actions must be taken immediately and new process parameters must be chosen.

As the calculated C_p value (C_p is larger than 1.33, the process meets the capability requirement with a 95 % confidence level, or equivalently, at the significance level $\alpha = 0.05$). These product items conform to the manufacturing specifications and are considered as reliable products. For $C_p \neq C_{pk}$, the process mean is not centred on the process width. The process mean is near to the target value. It is clear that in the observed performance no data are outside the specification limits. The number of non-conforming parts out of the LSL is $0.07 \cdot 10^{-6}$ and the USL is 241 ppm in a short period of time. The number of non-conforming parts out of the LSL is $0.05 \cdot 10^{-6}$ and the USL is $214 \cdot 10^{-6}$ in a long period of time.

4 CONCLUSIONS

In recent years, process-capability analysis has become an important integrated part in the applications of statistical techniques for quality assurance. Quality assurance in mass production is achieved using statistical process-control techniques. The process-capability analysis, which is a SPC technique, helps to determine the ability for manufacturing between tolerance limits and engineering specifications. The capability analysis gives information about the changes and tendencies of the systems during production.

In this study the process-capability analysis was carried out for the elimination of the quality problems during turning operations. The number of non-conforming parts was determined in observed values, in short and long periods of time. For the elimination of the observed quality problems, some suggestions were proposed. Faults regarding manufacturing out-of-tolerance limits were eliminated, the variability in the process and the cost due to low-quality production were reduced in the particular company.

In today's competitive market, SPC is not the most frequently used technique in small and medium-sized

companies in Turkey. The most important problems in business are that there are no trained employees to apply it and there is insufficient investment. Consequently, SPC must be applied widely and continuously to achieve quality improvements.

5 REFERENCES

- ¹ Ramakrishnan B, Sandborn P, Pecht M. Process capability indices and product reliability. *Microelectronics Reliability* 41 (2001), 2067–2070
- ² Montgomery DC. *Introduction to Statistical Quality Control*. New York: John Wiley & Sons Inc.; 2005, 364–413
- ³ Kane, VE. Process capability indices. *Journal of Quality Technology* 18 (1986), 41–52
- ⁴ Wright PA. The cumulative distribution function of process capability index C_{pm} . *Statistics and Probability Letters* 47 (2000), 49–251
- ⁵ Pearn WL, Shu MH, Hsu BM. Monitoring manufacturing quality for multiple Li-BPIC processes based on capability index C_{pmk} . *Int. Journal of Production Research* 43 (2005) 12, 2493–2512
- ⁶ Singhal, SC. Multi process performance analysis chart (MPPAC) with capability zones. *Quality Engineering* 4 (1991) 1, 75–81
- ⁷ Pearn, WL, Chen, KS. New generalization of the process capability index C_{pk} . *Journal of Applied Statistics* 25 (1988) 6, 801–810
- ⁸ Deleryd M, Garvare R, Klefsjö B. Experience of implementing statistical methods in small enterprises. *Total Quality Management*, 11 (1999) 5, 341–351
- ⁹ Gullu A, Motorcu AR, Statistical process Control in machining, a case study for machine tool capability and process capability. *Materials & Design* 27 (2006), 364–372
- ¹⁰ Dolinsek S, Kopac J. Linkage between quality assurance tools and machinability criteria. *Journal of Materials Processing Technology* 118 (2001), 133–137
- ¹¹ Deleryd M. A pragmatic view on process capability studies. *International Journal of Production Economics* 58 (1999), 319–330
- ¹² Corbett JCA, Pan JNE. Evaluating environmental performance using statistical process control techniques. *Journal of Operational Research* 139 (2002), 68–83
- ¹³ Chang YC, Wu CW, Assessing process capability based on the lower confidence bound of C_{pk} for asymmetric tolerances. *European Journal of Operational Research* 190 (2008), 205–227
- ¹⁴ Chen, KS, Pearn, WL, Lin, PC., A new generalization of the capability index C_{pm} for asymmetric tolerances. *International Journal of Reliability, Quality & Safety Engineering* 6 (1999) 4, 383–398
- ¹⁵ Linn R, Tsung F, Ellis LWC. Supplier selection based on process capability and price analysis. *Quality Engineering* 18 (2006), 123–129

